

# **HIGH FREQUENCY EARTHQUAKE GROUND MOTION SCALING IN UTAH**

Young Soo Jeon, B. E., M.S.

**A Thesis Submitted to the Faculty of the Graduate School  
of Saint Louis University in Partial Fulfillment of  
the Requirements for the Degree of  
Master of Science (Research)**

2000

# Digest

Vertical component velocity seismograms from the University of Utah Seismograph Stations are used to measure and quantify high frequency ground motion scaling for the seismically hazardous Wasatch front, the northeastern Basin and Range province. This study analyzed a data set consisting of 3000 waveform from 110 stations and 238 regional earthquakes and mining related seismic events in the range of 10 - 500 kilometer hypocentral distance.

The signals were processed to examine the peak ground velocity and Fourier velocity spectra in the frequency range of 1 - 16 Hz. Random vibration theory (RVT) is used to test estimates of the peak ground motion in the time domain and duration defined by the limits of 5% - 75% seismic energy that follows the onset of the S-waves used. Comparison of the two regressions indicated that our RVT related duration term for band pass filtered spectra is quite good and both regression results display consistent shapes.

Both the Fourier velocity and peak filtered time domain regression results are characterized by rapid decreases of amplitude at short distance. Low  $Q(f)$  and rapid  $g(r)$  are required to forward modeling. Using two different geometrical spreadings at short distances,  $Q = 145f^{0.65}$  for model A and  $Q = 180f^{0.6}$  for model B are required. These  $Q$  values are lower than that obtained in previous studies of  $Q$  in the Basin and Range province.  $\kappa_0 = 0.045$  and  $\Delta\sigma = 400$  are obtained by using Boore (1983) constant stress drop model and our attenuation relationships.

Possible explanations for the excitation of mining events are first, a higher  $\kappa = 0.09$  which reduces all high frequency because of a shallow source  $\kappa$  effect is needed in addition to the receiver site  $\kappa$  effect. The second possibility is that these are low stress drop events based on the idea that the collapse of long tunnels is a very slow process. Low stress drops imply lower corner frequencies for a given  $M_W$ . There is a better fit with the low stress drop event ( $\Delta\sigma = 0.1$ ), but the seismic moments are unrealistically large.

**HIGH FREQUENCY EARTHQUAKE GROUND  
MOTION SCALING IN UTAH**

Young Soo Jeon, B.E., M.S.

**A Thesis Submitted to the Faculty of the Graduate School  
of Saint Louis University in Partial Fulfillment of  
the Requirements for the Degree of  
Master of Science (Research)**

2000

COMMITTEE IN CHARGE OF CANDIDACY:

Professor Robert B. Herrmann,  
Chairperson and Advisor

Professor Brian J. Mitchell

Associate Professor Charles J. Ammon

## Acknowledgments

I would like to thank my parents for supporting me and giving me their unconditional love through my many years of study. I thank Dr. Robert B. Herrmann, my advisor, for his support throughout this work and everything he did for me. I also thank Dr. Brian Mitchell and Dr. Charles Ammon for critically reviewing this dissertation. I also thank Dr. James Pechman and Ms. Sue Nava of the University of Utah Seismograph stations for providing the excellent data set used for this research.

Finally I appreciate the assistance of my fellow students and friends for helping me to finish this work.

# Table of Contents

<b>1</b>	<b>Introduction</b>	<b>1</b>
1.1	Importance of high frequency ground motion . . . . .	1
1.2	Geologic and geophysical features of Utah . . . . .	4
1.2.1	Earthquakes . . . . .	4
1.2.2	Tectonic provinces . . . . .	4
1.2.3	Wasatch fault . . . . .	6
1.2.4	Fault activity . . . . .	8
1.2.5	Heat flow . . . . .	9
1.2.6	Q . . . . .	11
1.3	Seismic hazard . . . . .	13
1.3.1	General hazards . . . . .	13
1.3.2	Large earthquakes . . . . .	15
1.3.3	Specific hazards for Utah . . . . .	16
1.4	Objective of this study . . . . .	17
<b>2</b>	<b>Data set</b>	<b>19</b>
2.1	The University of Utah Seismic Network . . . . .	19
2.2	Instrument response correction . . . . .	24
<b>3</b>	<b>Data preparation and regression</b>	<b>26</b>
3.1	Objective of regression analysis . . . . .	26
3.2	Initial data preparation . . . . .	28
3.3	Trace analysis . . . . .	28
3.4	Quality control steps for entire data set . . . . .	29

3.5	Regression . . . . .	29
3.6	Regression of Fourier Velocity spectra . . . . .	33
3.7	Regression of Peak Filtered velocity . . . . .	39
3.8	Duration . . . . .	46
3.9	Excitation . . . . .	52
<b>4</b>	<b>Parameterization</b>	<b>59</b>
4.1	Modeling Fourier velocity spectra . . . . .	59
4.2	Modeling peak time domain values . . . . .	60
4.3	Propagation parameters . . . . .	62
4.4	Modeling source excitation . . . . .	68
<b>5</b>	<b>CONCLUSIONS</b>	<b>82</b>
5.1	Results . . . . .	82
5.2	Comparison of heat flow and attenuation parameters . . . . .	83
5.3	Mining events . . . . .	86
5.4	Final considerations . . . . .	87
	<b>Bibliography</b>	<b>77</b>
	<b>Vita Auctoris</b>	<b>84</b>



## List of Tables

1.1	Geologic history of study area . . . . .	7
1.2	$Q_{Lg}$ and $Q_C$ relations in the Basin and Range province from previous studies (Xie and Mitchell, 1990). BRP, GB, NTS, and SGB each denote Basin and Range province, Grean Basin, Nevada Test Site, and Southern Grean Basin. . . . .	13
1.3	Large earthquakes in the study area. . . . .	16
3.1	Attenuation functional at 1.0, 2.0, 3.0, and 4.0 Hz for Fourier Velocity spectra. The columns give values of frequency (first and sixth columns), hypocentral distance (second and seventh columns), attenuation $D(r,f)$ at a reference distance of 40 km (third and eighth columns), associated error bar (fourth and ninth columns) and number of observations (fifth and tenth columns). . . . .	37
3.2	Attenuation functional at 6.0, 8.0, 10.0, and 12.0 Hz for Fourier Velocity spectra. The columns give values of frequency (first and sixth columns), hypocentral distance (second and seventh columns), attenuation $D(r,f)$ at a reference distance of 40 km (third and eighth columns), associated error bar (fourth and ninth columns) and number of observations (fifth and tenth columns). . . . .	38

3.3	Attenuation functional at 14.0 and 16.0 Hz for Fourier Velocity spectra. The columns give values of frequency (first and sixth columns), hypocentral distance (second and seventh columns), attenuation $D(r,f)$ at a reference distance of 40 km (third and eighth columns), associated error bar (fourth and ninth columns) and number of observations (fifth and tenth columns). . . . .	39
3.4	Distance functional at 1.0, 2.0, 3.0, and 4.0 Hz for Band-Passed filtered. The columns give values of frequency (first and sixth columns), hypocentral distance (second and seventh columns), attenuation $D(r,f)$ at a reference distance of 40 km (third and eighth columns), associated error bar (fourth and ninth columns) and number of observations (fifth and tenth columns). . . . .	44
3.5	Distance functional at 6.0, 8.0, 10.0, and 12.0 Hz for Band-Passed Filtered. The columns give values of frequency (first and sixth columns), hypocentral distance (second and seventh columns), attenuation $D(r,f)$ at a reference distance of 40 km (third and eighth columns), associated error bar (fourth and ninth columns) and number of observations (fifth and tenth columns). . . . .	45

3.6	Distance functional at 14.0 and 16.0 Hz for Band-Passed Filtered. The columns give values of frequency (first and sixth columns), hypocentral distance (second and seventh columns), attenuation $D(r,f)$ at a reference distance of 40 km (third and eighth columns), associated error bar (fourth and ninth columns) and number of observations (fifth and tenth columns).	46
3.7	Durations as a function of distance and frequency ranges from 01 to 16 Hz. . . . .	52
4.1	Propagation parameters of Model A and Model B . . . . .	63

## List of Figures

2.1	Map showing the epicenter and station locations for the University of Utah data set . . . . .	20
2.2	Velocity sensitivity for ARUT which has the L4-C seismometer. . . . .	21
2.3	Velocity sensitivity for BHU which has the S-13 seismometer.	21
2.4	Velocity sensitivity for FSU which has the 18300 seismometer.	22
2.5	Velocity sensitivity for YFT which has the CMT-40T seismometer. . . . .	22
2.6	Velocity sensitivity for GRD which has the SS-1 seismometer.	23
2.7	Velocity sensitivity for SLC which has the simulated Wood-anderson response seismometer. . . . .	23
3.1	Source-receiver hypocentral distance distribution of observed station for the data recorded along the seismic network . . .	30
3.2	Regression analysis for 1.0 Hz. Top, initial estimate of $D(r)$ using coda normalization technique. Middle, initial and final propagation functionals. Bottom, final residuals of the regression analysis . . . . .	34

3.3	Regression analysis for 16 Hz. Top, initial estimate of $D(r)$ using coda normalization technique. Middle, initial and final propagation functionals. Bottom, final residuals of the regression analysis . . . . .	35
3.4	Attenuation functional $D(r, f)$ obtained from the regression of the Fourier amplitudes at the frequencies of 1.0, 2.0, 3.0, 4.0, 6.0, 8.0, 10.0, 12.0, 14.0, and 16.0 Hz. The reference hypocentral distance is at 40 km. . . . .	36
3.5	Regression analysis for 1.0 Hz. Top, initial estimate of $D(r)$ using coda normalization technique. Middle, initial and final propagation functionals. Bottom, final residuals of the regression analysis . . . . .	40
3.6	Regression analysis for 16 Hz. Top, initial estimate of $D(r)$ using coda normalization technique. Middle, initial and final propagation functionals. Bottom, final residuals of the regression analysis . . . . .	41
3.7	Attenuation functional $D(r, f)$ obtained from the regression of the filtered velocities at the frequencies of 1.0, 2.0, 3.0, 4.0, 6.0, 8.0, 10.0, 12.0, 14.0, and 16.0 Hz. The reference hypocentral distance is at 40 km. . . . .	43
3.8	Duration data and regression lines as a function of distance for filter frequency of 1.0 Hz . . . . .	48

3.9	Duration data and regression lines as a function of distance for filter frequency of 16 Hz . . . . .	49
3.10	Distance dependence of duration for filtered data at the different frequencies. Thick black line is a total duration estimation for frequencies . . . . .	51
3.11	Inverted Fourier velocity excitation terms for the earthquake events recorded by vertical component velocity seismograms plotted on a linear frequency scale . . . . .	54
3.12	Inverted Fourier velocity excitation terms for the mining related events recorded by vertical component velocity seismograms plotted on a linear frequency scale . . . . .	55
3.13	Inverted Filtered ground velocity excitation terms for the earthquake events recorded by vertical component velocity seismograms plotted on a linear frequency scale . . . . .	56
3.14	Inverted Filtered ground velocity excitation terms for the mining related events recorded by vertical component velocity seismograms plotted on a linear frequency scale . . . . .	57
3.15	Map showing the earthquake-epicenters and stations for University of Utah data . . . . .	58
3.16	Map showing the explosion induced epicenters and stations for University of Utah data . . . . .	58

4.1	Residuals of the model fit to the Fourier velocity distance and geometrical spreading function of Model A . . . . .	64
4.2	Residuals of the model fit to the Fourier velocity distance and geometrical spreading function of Model B . . . . .	65
4.3	Residuals of the model fit to the band pass distance and geometrical spreading function of Model A . . . . .	66
4.4	Residuals of the model fit to the band pass distance and geometrical spreading function of Model B . . . . .	67
4.5	Fourier acceleration spectra at a distance 1 km as a function of $M_W$ for stress drop 10, 30, 100, 200 and 400 bars. Dark and lightest line indicate 10 and 400 bars. The different $M_W$ are indicated by the different low frequency asymptotics. For a given $M_W$ , the high frequency level varies as $\Delta\sigma$ . . . . .	70
4.6	Excitation of Fourier velocity spectra at 40 km (Model A). The thick dash curve is the prediction of the 400 bar constant stress drop source model. E is the $\log_{10}$ of the Fourier velocity spectra in $m/sec$ . . . . .	72
4.7	Excitation of Fourier velocity spectra at 40 km (Model A) in linear scale of frequency range. The thick dash curve is the prediction of the 400 bar constant stress drop source model. E is the $\log_{10}$ of the Fourier velocity spectra in $m/sec$ . . . . .	73

4.8	Excitation of Fourier velocity spectra at 40 km (Model B). The thick dash curve is the prediction of the 400 bar constant stress drop source model. E is the $\log_{10}$ of the Fourier velocity spectra in $m/sec$ . . . . .	74
4.9	Excitation of Fourier velocity spectra at 40 km (Model B) in linear scale of frequency range. The thick dash curve is the prediction of the 400 bar constant stress drop source model. E is the $\log_{10}$ of the Fourier velocity spectra in $m/sec$ . . . . .	75
4.10	Excitation of peak filtered velocity at 40 km (Model A). The thick dash curve is the prediction of the 400 bar constant stress drop source model. E is the $\log_{10}$ of the peak filtered velocity spectra in $m/sec$ . . . . .	76
4.11	Excitation of peak filtered velocity at 40 km (Model A) in linear scale of frequency range. The thick dash curve is the prediction of the 400 bar constant stress drop source model. E is the $\log_{10}$ of the peak filtered velocity spectra in $m/sec$ . . . . .	77
4.12	Excitation of peak filtered velocity at 40 km (Model B). The thick dash curve is the prediction of the 400 bar constant stress drop source model. E is the $\log_{10}$ of the peak filtered velocity spectra in $m/sec$ . . . . .	78



4.13	Excitation of peak filtered velocity at 40 km (Model B) in linear scale of frequency range. The thick dash curve is the prediction of the 400 bar constant stress drop source model. E is the $\log_{10}$ of the peak filtered velocity spectra in $m/sec$ . . . . .	79
4.14	Mining related excitation of Fourier velocity spectra at 40 km. The thick curve is the prediction of the 400 bar stress drop source with $\kappa_{eff} = 0.09$ for propagation model A. E is the $\log_{10}$ of the Fourier velocity spectra in $m/sec$ . . . . .	80
4.15	Mining related excitation of Fourier velocity spectra at 40 km. The thick curve is the prediction of the 0.1 bar constant stress drop for propagation model A. E is the $\log_{10}$ of the Fourier velocity spectra in $m/sec$ . . . . .	81
5.1	Regression analysis for 2.0 Hz. Top, initial estimate of $D(r)$ using coda normalization technique. Middle, initial and final propagation functionals. Bottom, Final residuals of the regression analysis . . . . .	66
5.2	Regression analysis for 4.0 Hz. Top, initial estimate of $D(r)$ using coda normalization technique. Middle, initial and final propagation functionals. Bottom, Final residuals of the regression analysis . . . . .	67

5.3	Regression analysis for 8.0 Hz. Top, initial estimate of $D(r)$ using coda normalization technique. Middle, initial and final propagation functionals. Bottom, Final residuals of the regression analysis . . . . .	68
5.4	Regression analysis for 12 Hz. Top, initial estimate of $D(r)$ using coda normalization technique. Middle, initial and final propagation functionals. Bottom, Final residuals of the regression analysis . . . . .	69
5.5	Regression analysis for 2.0 Hz. Top, initial estimate of $D(r)$ using coda normalization technique. Middle, initial and final propagation functionals. Bottom, Final residuals of the regression analysis . . . . .	70
5.6	Regression analysis for 4.0 Hz. Top, initial estimate of $D(r)$ using coda normalization technique. Middle, initial and final propagation functionals. Bottom, Final residuals of the regression analysis . . . . .	71
5.7	Regression analysis for 8.0 Hz. Top, initial estimate of $D(r)$ using coda normalization technique. Middle, initial and final propagation functionals. Bottom, Final residuals of the regression analysis . . . . .	72

5.8	Regression analysis for 12 Hz. Top, initial estimate of $D(r)$ using coda normalization technique. Middle, initial and final propagation functionals. Bottom, Final residuals of the regression analysis . . . . .	73
5.9	Duration data and regression lines as a function of distance for filtered frequency of 2.0 Hz . . . . .	74
5.10	Duration data and regression lines as a function of distance for filtered frequency of 6.0 Hz . . . . .	75
5.11	Duration data and regression lines as a function of distance for filtered frequency of 12 Hz . . . . .	76

# 1. Introduction

## 1.1 Importance of high frequency ground motion

Studies of high frequency (greater than 1 Hz) ground motions provide seismologists an understanding of seismic source properties and physical models of the Earth's structure through which the waves pass. Predictive or physical ground motion models developed by seismologists usually involve either the prediction of the motions from a fault of specified dimension and orientation, such as slip or rupture velocity over the fault surface (e.g., Bouchon, 1978; Joyner and Boore, 1980) or the random superposition of the theoretically radiated fields from many circular patches, concentrated at a point (e.g., Boatwright, 1982). The former is useful for site specific simulations, whereas the latter captures the essence of high frequency motion at an average site from an average earthquake of specified size.

Engineers are interested in the motions that structures have to endure. For engineering purposes, amplitudes, frequency content and duration of the motion are important. For structural response (Kramer, 1996), the engineering community requires empirical or model based predictions of strong motion for design, seismic hazard analysis and loss modeling.

Equations giving ground motion as a function of magnitude and distance can be empirical or model based. Empirical methods require a large data set in terms of earthquake size and observation distance for regression. Model based predictions use parametric models to provide an excitation of site spectrum and duration, which is then used with a stochastic

simulation of ground motion.

The ground motions produced by earthquakes are very complicated. The identification and evaluation of factors controlling ground motions as a function of distance and magnitude are essential for seismological and earthquake engineering applications. Ground motion at a site is affected by source, travel path, and local site conditions. Earthquake size, depth, stress drop, rupture process, and fault geometry influence the source factors. Travel path factors, which describe seismic wave propagation through the body of the earth, are geometrical attenuation, dissipation of seismic energy due to anelastic properties of the earth, and scattering of elastic waves during propagation. The shallow crustal rock and soil properties and the effect of the surface topography at a local site control site conditions.

The physical characteristic of the propagation which carries elastic energy can change. Ground motion at periods ( $\gg 1$  sec) will generally be dominated by surface waves. The fundamental-mode surface waves are affected by scattering (produced by the complexity) and intrinsic absorption of the medium as they pass through a laterally complex structure. The direct S wave carries the main shear wave energy at short distance ( $\leq 80$ km), while the postcritical reflections of S waves, namely Lg wave, are the dominant phase at distances of 150 to 1000 km. Wave propagation in the transition distance range of 80 to 150 km is more complex (Samiezade-Yard, 1993).

Any attempt to understand the attenuation of ground motion has to deal with the question of separation of the geometrical spreading contribution to amplitude decrease from intrinsic attenuation and scattering in

the different distance ranges where the nature of the motion may change. Geometrical attenuation is usually assumed as a frequency independent operator in the overall wave propagation (Ou and Herrmann, 1990; Frankel et al., 1990). Cracks, faults, and velocity heterogeneities of different scales within the crust affect the wave scattering. The scattering itself is a frequency dependent factor causing only a redistribution of the energy in space and time. A proper strategy of investigating elastic waves should account for the total energy, the degree of scattering, and total contribution of apparent attenuation.

Local site effects can amplify or deamplify ground motion as a function of frequency. Geology and the type of rocks or sediment around the site are controlling factors in evaluating the site factor (Su et al., 1992; Mayeda et al., 1992; Castro et al., 1990; Philips and Aki, 1986). Younger and less consolidated sediments may amplify seismic waves several times more than hard rocks because of different impedance and resonance effects. At the same time, wave scattering and anelastic attenuation can remove high frequencies from the signal (Boore and Joyner, 1991). Non-linear effects on seismic waves would be an increase in damping and a decrease in propagation velocity, with consequent reduction in high-frequency amplitudes and shifts to lower frequencies of the spectral resonant peaks of the soil deposit (Cultrera et al., 1999). The two competing factors can be described in terms of a site amplification,  $V(f)$ , and an attenuation parameter  $\kappa$  (Boore and Joyner, 1991). Topography and sediment thickness variation can distort wave forms and amplitudes. Topographic irregularities can produce complex patterns of amplification or deamplification, depending on the geometry of the irregularity, the frequencies, and angles of

the incoming waves (Sanchez-Sesma and Campillo, 1993). The curvature of a basin where softer alluvial soils have been deposited can trap body waves and lead incident body waves to propagate through the alluvium as surface waves (Vidale and Helmberger, 1988). These waves can produce stronger shaking and longer durations.

## **1.2 Geologic and geophysical features of Utah**

### **1.2.1 Earthquakes**

About 700 earthquakes (including aftershocks) are recorded in the Utah region each year. About 2 % of the earthquakes are felt and an average of 13 earthquakes of magnitude 3.0 or larger occur in the region every year. Earthquakes can occur anywhere in the state of Utah. Since 1850, at least 15 earthquakes of magnitude 5.5 and larger have occurred in the Utah region on the average of once every 7 years (<http://www.seis.utah.edu/HTML/UtahsEarthquakeThreat2.html>). The earthquakes are related to the tectonic processes within the region.

### **1.2.2 Tectonic provinces**

Part of Utah lies in the Basin and Range province, the largest intra-continental rift in the world which contains important clues to the deep structure of continental rifts, the nature of "transitional crust," and the relations of rifting to prior thrust faulting. This region is characterized by high heat flow, seismicity, intensive normal faulting, and an extensive distribution of Cenozoic Volcanoes (e.g. Lachenbruch and Sass 1978; Priestley and Brune; 1978). Petrological studies show that the area was a region of andesitic volcanism until late Cenozoic, when basaltic volcanism became

more predominant (Stewart and Carlson, 1976).

Models of Basin and Range extension include the classic horst and graben geometry with steeply dipping normal faults (Zoback et al., 1981; Wernicke, 1981).

The ranges in east-central Nevada and west-central Utah are underlain mostly by upper Precambrian to Triassic sequence of sandstones, shales, and carbonates. This well-known miogeoclinal succession includes about 20 distinctive and regionally extensive formations with an aggregate thickness in excess of 13 km (Stewart and Poole, 1974; Hose and Blake, 1976).

Despite major regional variations in the absolute timing of volcanism and normal faulting, local eruptive and extensional histories are strikingly similar (Gans et al; 1989). Present-day faulting is concentrated along the margins of the Basin and Range province, expanding into the thinner, gravitationally unstable crust of the Sierra Nevada and Colorado Plateau (e.g., Best and Brimhall, 1974). The seismicity of east of the Wasatch Fault may be fundamentally influenced by the Cenozoic structure, or perhaps by bending stress induced by crustal flexure (Zandt and Owens, 1980).

The northern Utah region is near the transition of the Basin and Range, the middle Rocky Mountains, the Colorado Plateau and the Columbia Plateau geologic provinces. Bucher and Smith (1971) reported that the crust is about 40 km thick in the northern Colorado Plateau province and about 32 km thick in the eastern Basin and Range province. Both have similar properties such as moderate to high heat flow, low upper-mantle seismic velocities, and a high rate of seismic attenuation. Priestley and Brune (1978) mentioned that the reason for low shear-wave velocities found in upper mantle in Great Basin is due to a zone of tension into which deep



mantle material has intruded relatively close to the surface to create a zone of partial melting.

Table 1.1 is a brief summary of significant events in Utah's geologic history as extracted from the more detailed description by Utah Geological Survey at <http://www.ugs.state.ut.us/geohist.htm>.

### **1.2.3 Wasatch fault**

The Wasatch Mountains is in the zone of transition between the northeastern margin of the active Basin and Range extensional province and the less-deformed Colorado Plateau and Wyoming Basin tectonic provinces to its east (Powell and Chapman, 1990). The Wasatch Range in the southwest of the Middle Rocky Mountains province and the Utah High Plateaus marks the transitional boundary between the thermal regimes, structural styles and stress states of the Basin and Range and Colorado Plateau (Bodell and Chapman, 1982; Eaton, 1982).

This transitional region is also the locale of a pronounced zone of intraplate seismicity, the Intermountain Seismic Belt (ISB) (Arabasz et al., 1980). About 500 earthquakes are located in the Wasatch Front region each year and about 60 % of the earthquakes of magnitude 3.0 and larger in Utah region occur in the Wasatch front region. The boundary region is cut by steeply dipping normal faults with northerly strike - an orientation characteristic of the northern Basin and Range. The slip rate of Wasatch Front is  $(1.8 \pm 0.6)$ mm/yr and most of the earthquake focal depths are located less than 20 km.

The Wasatch fault, the west front of the Wasatch mountains, is marked by a large normal fault displacement. It has cut across the Cottonwood

Period	Duration	Description of events
Quaternary	Holocene	Erosional and depositional processes dominate. Basin-Range faults continue to be active. Volcanic eruptions continue in western Utah, as recently as 660 years ago.
Quaternary	Pleistocene	Glaciers blanket the Unita Mountains, the Wasatch Range, and mountains of the Colorado Plateau.
Tertiary	Pliocene	Volcanism continues in southwestern Utah. Basin and Range faulting and regional uplift continues.
Tertiary	Oligocene	Igneous activity produces intrusive rocks in northern Utah and volcanoes in southwestern Utah.
Tertiary	Miocene	Basin and Range faulting in western Utah creates mountain-valley-mountain topography and the Wasatch fault zone. Igneous intrusions continue to form in the Henry and Abajo Mountains and Igneous activity continues until approximately 15 million years ago.
Tertiary	Eocene	In the Unita Basin thousands of feet of sediment are deposited. Granitic intrusions and volcanic flows occur in northwestern Utah during the late Eocene.
Tertiary	Paleocene	Eroding highlands prevail in western Utah. The Unita Mountains uplift smaller and the Unita basin becomes prominent features in eastern Utah.
Cretaceous	138 Ma - 66 Ma	in eastern Utah, sea invades from the east. Western Utah rises due to thrust faulting and folding generated by east-west directed compressional factors.
Jurassic	205 Ma - 138 Ma	In central Utah, the Arapien basin develops and receives over 6,000 feet of sediment including large amounts of gypsum and salt.

Table 1.1: Geologic history of study area

dome and been displaced the west part downward several thousand feet (Guidebook to the geology of Utah, Park City district Utah. No 22, 1968). It extends approximately 370 km in a north-south direction. Recent GPS survey results in this region indicate rapid crustal extension at a rate of  $2.7 \pm 1.3$  mm/yr. This horizontal displacement rate across a 55 km wide area is two or three time larger than the average Late Quaternary fault slip rate measured in conventional method (Smith et al., 1998).

#### 1.2.4 Fault activity

The presence of a fault itself does not indicate the probability of future earthquakes. The more important notion of fault activity has been a topic of considerable discussion and controversy. The terminology "active fault" describes a fault that poses a current earthquake threat. Formal definition of fault activity is important because this often trigger legal requirements for special investigations or special design provisions. Various criteria are used to define fault activity (Krammer, 1996).

Slemmons and McKinney (1977) found 31 different definitions of an active fault given in terms of the elapsed period of time since the most recent fault movement. The California Division of Mines and Geology defines an active fault as one that has produced surface displacement within Holocene time (approximately 10,000 years). For dams, the U.S. Army Corps of Engineers has used a time period of 35,000 years, and the U.S. Bureau of Reclamation has used 100,000 years (Idriss, 1985). The U.S Nuclear Regulatory Commission (*Code of Federal Regulations, 1978*) has used the term *Capable fault* (rather than active fault) for the following:

I Movement at or near the ground surface at least once within

the past 35,000 years or movement of a recurring nature within the past 500,000 years

- II Macroseismicity instrumentally determined with records of sufficient precision to demonstrate a direct relationship with the fault
- III A structural relationship to a capable fault according to characteristics of above, such as movement that one could reasonably be expected to be accompanied by movement on the other.

Utah has several fault zones in the "active" category. Any fault which has displaced recent alluvium and whose surface effects have not been modified to any appreciable extent by recent erosion (since the last few hundred or thousand years) is active. More than 90 percent of 263 earthquakes since 1847 to early 1960 had their origin in the five active fault zones identified. These are Hansel Valley fault, Wasatch fault, Sevier fault, Elsinore fault, and Hurricane fault. Most geological and historical fault scarps in Utah and the Great Basin are observed in alluvial deposits close to the foot of the adjacent mountains fronts and extend well into the adjacent valleys (Utah Geological Society Guidebook to the geology of Utah. No 18, 1964).

### **1.2.5 Heat flow**

The study area is focused mainly on the eastern Basin and Range province, Colorado Plateau, and Wyoming Basin. The Wasatch Mountains of Utah lie in the zone of transition between these provinces. The thermal state of the crust influences the rheology, orientation and concentration of stresses,

crustal magnetic processes, depth distribution of earthquakes, magmatic processes, and the physical and chemical conditions of metamorphic processes. The temperature distribution within the crust can also reflect processes that modify lithospheric structure (Powell and Chapman, 1990). Therefore, identifying thermal state of tectonic provinces and their boundaries is very important.

In the last 30 My, the region has undergone extension and apparent crustal thinning, with concomitant magmatism. Normal faulting and other structural elements associated with the extension follow the grain of the earlier compressional structure. These features are dynamically associated with the changing convergent and transcurrent conditions at the western boundary of the North American plate (Atwater, 1970; Eaton, 1982).

The typical heat flow of the eastern Basin and Range is 90-105  $\text{mW m}^{-2}$  (Lachenbruch and Sass, 1977; Blackwell, 1978; Chapman et al., 1981). This high value of heat flow can be attributed to any of a number of advective processes which effectively transport heat into and through the crust (Blackwell, 1978; Lachenbruch and Sass, 1978). Heat flow in the Basin and Range exhibits more tectonic variability than is usual in a continental tectonic province, due to active hydrothermal systems in the upper crust, regional hydrologic effects, and the localized episodic nature of the extension processes and magmatism (Powell and Chapman, 1990). But the heat flow observations alone cannot discriminate among the causative processes.

Heat flow in the interior of the Colorado Plateau is typically 55-60  $\text{mW m}^{-2}$  (Bodell and Chapman, 1982) and exhibits less variability than the Basin and Range region. The west, south and southeast margins of

the Colorado Plateau have higher heat flow than the interior, approaching that of the adjacent extensional province (Reither et al., 1979; Bodell and Chapman, 1982). Heat flow in the Wyoming basins is about  $60 \text{ mW m}^{-2}$  (Bodell and Chapman, 1982; Chapman et al., 1984). For comparison, heat flow along the San Andreas Fault in California is  $40 - 100 \text{ mW m}^{-2}$  and less than  $40 \text{ mW m}^{-2}$  in Sierra Nevada (Sass et al., 1981; ; Sass et al., 1997). The mean heat flow values of the eastern United States are  $59 \pm 22 \text{ mW m}^{-2}$  in the Central Lowlands,  $42 \pm 17 \text{ mW m}^{-2}$  in the Coastal Plain, and  $53 \pm 14 \text{ mW m}^{-2}$  in the Appalachian Highlands (Morgan and Gosnold, 1989).

### 1.2.6 Q

Q is a parameter that describes the filtering of high frequencies as propagates. The shallow part of the earth's crust contains lateral heterogeneities and short period (high frequency) waves are sensitive to those details. The longer the waves travel, the greater the variety of heterogeneities they encounter.

Studies of the rate of anelastic attenuation of seismic waves have shown the existence of lateral variations in the crust and upper mantle in the continent of the United States. It is now generally accepted that seismic anelastic attenuation of the western United States is high, while it is low in the central and eastern United States. However, detailed short-period attenuation observations over short paths within individual geological provinces of the continental United States are needed (Singh and Herrmann, 1983).

Q, which quantify the intrinsic absorption (or anelasticity) of the medium, is affected by factors such as temperature, the amount of fluid content, and

partial melt or solid-state dislocation motion in the crust or upper mantle. The attenuation of seismic shear waves in the crust is affected by anelasticity and scattering. Previous studies of  $Q$  in the Basin and Range province indicated lower  $Q$  values than in stable regions of North America. Singh and Herrmann (1983) provided a crude regionalization of Lg coda  $Q$  with lowest values in the west with values between 140 and 200 along the west coast, an average value of 200 - 300 on the Basin and Range province, and 400 in the Colorado Plateau. Coda  $Q$  increases rapidly up to 600 - 800 along the Rocky Mountain front and increases gradually up to 1300 in the Interior Highlands of the central United States. Somewhat lower values (700 - 1000) are found in the eastern United States.

Mitchell (1975) obtained a model of crustal shear wave  $Q_\mu$  for the western United States and found that differences in Rayleigh wave attenuation between the eastern and western United States could be explained by lower values of  $Q_\mu$  in the western United States. The crustal  $Q_\mu$  in the Basin and Range province shows lower  $Q_\mu$  values in the upper crust than that found in the upper crust of more stable regions. This low  $Q$  layer provides an explanation for high relative attenuation.

Historically, attenuation relations were first developed empirically for California by regression analysis of observed ground motion parameters, most typically peak horizontal acceleration ( $a_{max}$ ). These relations are quite reliable for California, where there are sufficient numbers of strong-motion data base (Boore and Atkinson, 1987). However, sufficient quantities of these data are not available for the Intermountain Seismic Belt.

Knowledge of intrinsic  $Q$  values within the crust and upper mantle may therefore contribute to our understanding of the tectonic evolution

Authors	Source Type & Region	Frequency range	Result
Singh & Herrmann (1983)	earthquake & BRP	0.6-3.5 Hz	$Q_c(f) = 250(\pm 50)f^{(0.45 \pm 0.05)}$
Chavez & Priestley (1986)	explosion & GB	0.3-10.0 Hz	$Q_{Lg}(f) = 206f^{(0.68)}$
Chavez & Priestley (1986)	earthquake & GB	0.3-5.0 Hz	$Q_{Lg}(f) = 214(\pm 15)f^{(0.54 \pm 0.09)}$
Nuttli (1986)	explosion & NTS	0.5-2.0 Hz	$Q_c(f) = 139f^{(0.6)}$
Rogers et al. (1987)	earthquake & SGB	1.0-10.0 Hz	$Q_c(f) = 143f^{(0.84)}$
Rogers et al. (1987)	earthquake & SGB	1.0-10.0 Hz	$Q_{Lg}(f) = 774f^{(0.04)}$

Table 1.2:  $Q_{Lg}$  and  $Q_C$  relations in the Basin and Range province from previous studies (Xie and Mitchell, 1990). BRP, GB, NTS, and SGB each denote Basin and Range province, Green Basin, Nevada Test Site, and Southern Green Basin.

of regions where these values have been determined (Mitchel et al., 1994). The difference between Q models could be due to the regional variations in crustal structure. Previous studies of  $Q_{Lg}$  and  $Q_C$  values in Basin and Range province are summarized in Table 1.2, where Lg Q and coda Q are denoted by  $Q_{Lg}$  and  $Q_C$ . the  $Q_{Lg}$  and  $Q_C$  values at 1 Hz vary from 140 - 774. Inconsistent Q relations may be due to imprecise inverse methods (erroneous forward models), inversion parameter trade-offs, a different seismic phases used (Xie and Mitchell, 1990).

## 1.3 Seismic hazard

### 1.3.1 General hazards

#### Ground shaking

When the seismic waves radiate away from the source and travel through the earth's crust reach the surface, they produce shaking that lasts from a few seconds to minutes. The strength and duration of shaking depends



on the size and location of the earthquake and the site's characteristics. Ground shaking may cause tremendous damage to the site near the source of a large earthquake.

Even if the waves propagate through rock from the source of an earthquake to the ground surface, the waves normally reach the top soil and the characteristics of the soil shaking can influence the ground surface. Soil deposits tend to act as "filters" to seismic waves by attenuating motion at certain frequencies and amplifying it at others. Levels of ground shaking vary within a small area due to the variance of soil conditions on the area (Kramer, 1996).

### **Liquefaction**

Liquefaction may occur when soil deposits have lost their strength and behave as a viscous liquid rather than as a solid. It reduces the strength of the soil to the point where it causes the building to collapse or to be unstable, empty buried tanks to rise to the surface, slope failures, lateral spreading, surface subsidence, ground cracking and sand blows.

### **Liquefaction in Utah**

Earthquake liquefaction has caused significant damage and is also one major earthquake hazard in Utah. The 1934 Hansel Valley and 1962 Cache Valley earthquakes caused liquefaction, and large prehistoric lateral spreads exist at many locations along the Wasatch Front. The valleys of the Wasatch Front are especially vulnerable to liquefaction because of susceptible soils, shallow ground water, and relatively high probability of moderate to large earthquakes.

The following conditions must exist for liquefaction to occur: susceptible soil, strong ground shaking and significant duration of strong motion. Investigation of local geology, subsurface soil and water conditions in the study region may identify susceptible sites. The most susceptible soils are generally along rivers, streams, lake shorelines, and some ancient river and lake deposits. Hazard-reduction techniques such as soil improvement or special foundation design may reduce the potential damage (<http://www. ugs.state.ut.us/geohist.htm>).

Soil improvement techniques are commonly used at sites where the existing soil conditions are expected to lead to large soil movements, such as horizontal or vertical movements. Reducing excessive porewater pressing during earthquake shaking or increasing the strength and stiffness of the soil are the main goals of the soil improvement techniques. The most common techniques are densification techniques, reinforcement techniques, grouting/mixing techniques, and drainage techniques (Krammer, 1996).

### **1.3.2 Large earthquakes**

Utah's largest earthquakes since settlement in 1847 was the magnitude of 6.6 1934 Hansel Valley earthquake, north of the Great Salt Lake. Not only large earthquakes but also moderate-sized earthquakes that occur near urban areas can cause major damage. Since 1850, at least 15 earthquakes of magnitude greater than 5.5 have occurred in the Utah region whose recurrence in a modern urban region could cause significant damage. The time period between moderate size earthquakes in this region is approximately 7 years. Table 1.3 presents recent magnitude 5.0 and larger earthquakes in the Utah region for the past 40 years.

Local Date	Magnitude	Location
Jan. 29, 1989	5.4	16 miles SE of Salina
Aug. 14, 1988	5.3	Central Emery County
Mar. 27, 1975	6.0	Pocatello Valley (Utah-Idaho border)
Oct. 14, 1967	5.2	Marysvale
Aug. 16, 1966	5.6	Utah-Nevada border
Sep. 05, 1962	5.2	Salt Lake Valley
Aug. 30, 1962	5.7	Cache Valley

Table 1.3: Large earthquakes in the study area.

### 1.3.3 Specific hazards for Utah

The Wasatch front is well recognized as being seismically hazardous (Smith, 1974; Cluff et al., 1975; Algermissen and Perkins, 1976), and earthquakes of magnitude 7.5 have been postulated as "credible" for this area by the U.S. Geological Survey (1976). The primary earthquake hazards of ground shaking and displacement along the surface faults in the Wasatch front area are similar to those of California.

Potential earthquake hazards in this area include;

- I Earthquake-triggered landslides and rock and snow avalanches along the mountainous Wasatch front
- II Soil liquefaction, differential ground settlement, and landslides
- III Catastrophic flooding from impounded reservoirs in the Wasatch Mountains upstream from densely populated centers
- IV Disruption of vulnerable life-support facilities that cross the Wasatch Fault (Arabasz et al., 1980).

Future large earthquakes of a magnitude 7.5 along the Wasatch fault will break segments of the fault about 32 - 64 kilometers long and 3 - 6 meters of surface displacement and strong ground shaking that could produce considerable damage up to 80 kilometers from the earthquake. The strong ground shaking also may cause soil liquefaction, landslides, rock falls, and broad permanent tilting of valley floors that may force the Great Salt Lake or Utah Lake to inundate urban areas (<http://www.ugs.state.ut.us/geohist.htm>)

#### **1.4 Objective of this study**

The objective of this study is the quantitative description of the regional attenuations of the earthquake and mining induced high frequency ground motion in Utah, especially along the Wasatch front by using University of Utah's regional seismic network. Understanding regional variations in attenuation is important for predicting the amplitude of strong ground motion expected from a future earthquake. Describing the attenuation of the ground motion as a function of frequency and hypocentral distance can be used for engineering design and seismic hazard.

The goal of earthquake-resistant design is to produce a structure or facility that can withstand a certain level of facility without excessive damage. The specification of the ground motion is one of the most difficult and most important problems in geotechnical earthquake engineering (Kramer, 1996).

A study of high frequency ground motion scaling in Utah can be compared to results of similar studies in other regions of the United States. Furthermore, we can develop the predictive relation and extrapolate to

larger events. The results of this study are important for seismic hazard studies since a large data set will be used to constrain the distance dependence of high frequency ground motion in the frequency range that is responsible for earthquake damage.

## 2. Data set

### 2.1 The University of Utah Seismic Network

The University of Utah regional seismic network extends from north of the Idaho-Utah border to south of the Utah-Arizona border, ranging from  $43^{\circ}$  to  $37^{\circ}$  in latitude and from  $-114^{\circ}$  to  $-109^{\circ}$  in longitude. Figure 2.1 shows the epicenters of events and stations of the University of Utah Seismograph Network providing the waveform data set used in this study.

The data set analyzed in this paper consists of 3000 waveforms from 110 stations and 238 regional earthquakes and other seismic events recorded primarily during the first two quarters of 1999. The observations cover a range of 500 kilometers in hypocentral distance. All events are within the upper crust.

We use the vertical component velocity seismograms from the University of Utah Seismograph Network to study ground motion scaling with distance for comparison to other locales in the US. Because of limited telemetry bandwidth and the desire to cover large geographic regions, regional seismic networks have relied on vertical component data. These are supplemented by modern three-component broadband data from selected stations. The sensors consist of Mark Products L4 or L4C's, Geotech S13 or 18300's, a simulated Wood Anderson, Kinematics SS-1 and Guralp CMG-40T and CMG3-ESP's. The velocity sensitivities for selected stations are plotted in units of (counts/m/sec) in Figures 2.2-2.7 to illustrate the response shapes. The L4, S13 and 18300 responses are approximately flat to ground velocity in the 1 - 10 Hz passband. The broadband CMG-40T

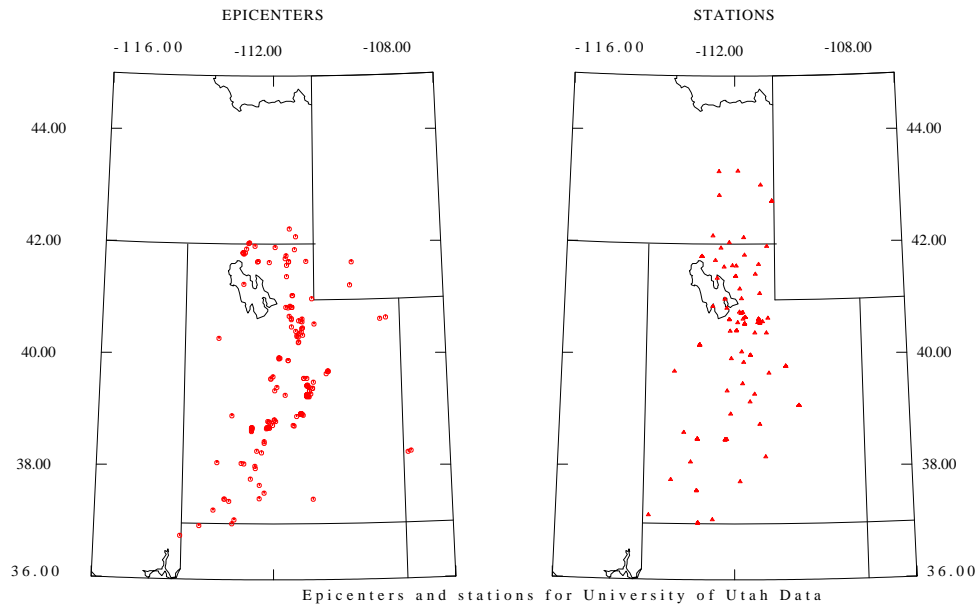


Figure 2.1: Map showing the epicenter and station locations for the University of Utah data set

sensor is very flat in the 0.1 - 10.0 Hz passband, while the SS-1 response is peaked between 1 - 2 Hz. The simulated Wood-Anderson displacement sensitivity at SLC is flat for frequencies greater than 1.25 Hz for which its corresponding velocity sensitivity falls off as  $f^{-1}$ .

The digital waveforms distributed by the University of Utah are obtained from the University of Utah Seismic Network (Utah), the U. S. Geological Survey (USGS), Snow College (SNOW), the Idaho National Engineering and Environmental Lab (INEEL), the U.S. Bureau of Reclamation (USBR), and the Lawrence Livermore National Lab (LLNL) seismic networks.

The deployed seismometer systems are described as

- 1) USSS single-component, analog-telemetry, short-period
- 2) USSS multi-component, analog-telemetry, short-period

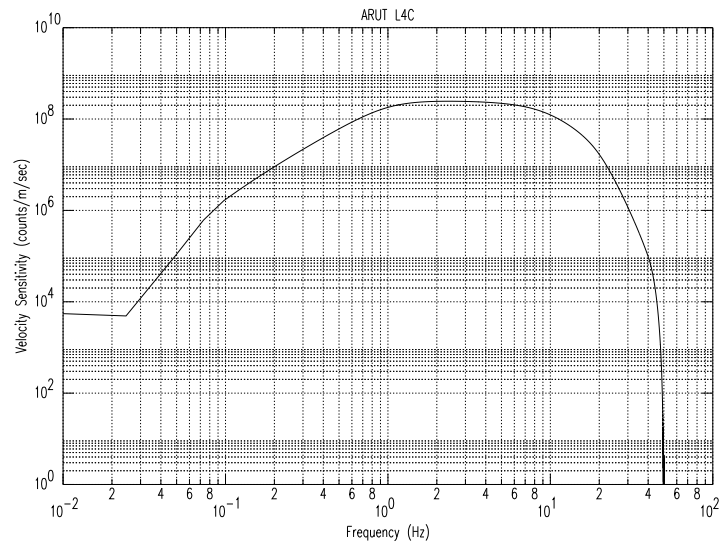


Figure 2.2: Velocity sensitivity for ARUT which has the L4-C seismometer.

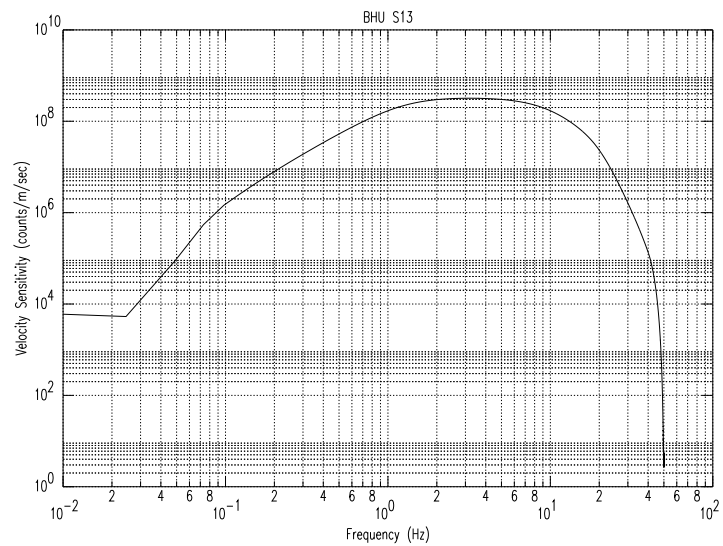


Figure 2.3: Velocity sensitivity for BHU which has the S-13 seismometer.



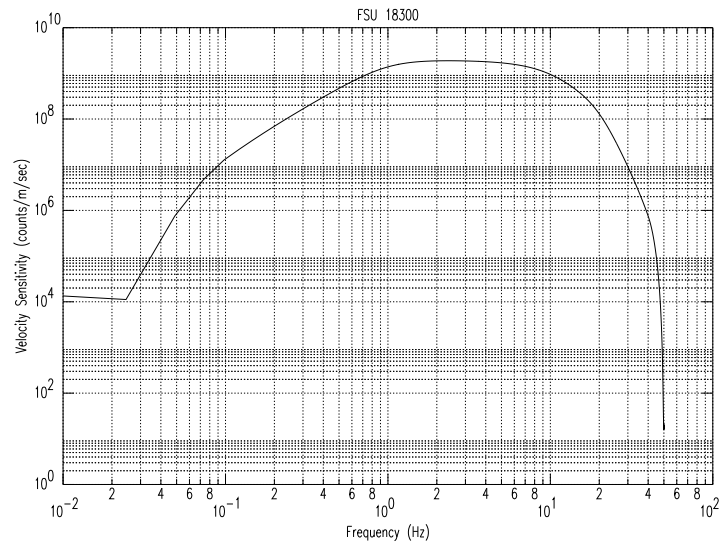


Figure 2.4: Velocity sensitivity for FSU which has the 18300 seismometer.

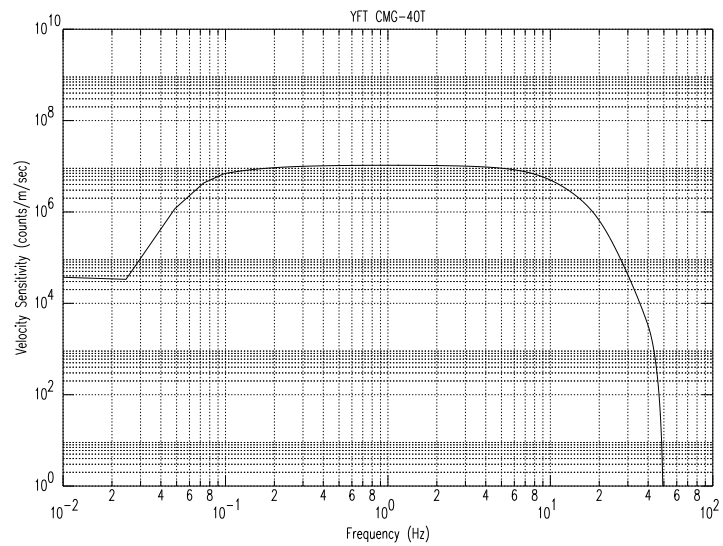


Figure 2.5: Velocity sensitivity for YFT which has the CMG-40T seismometer.

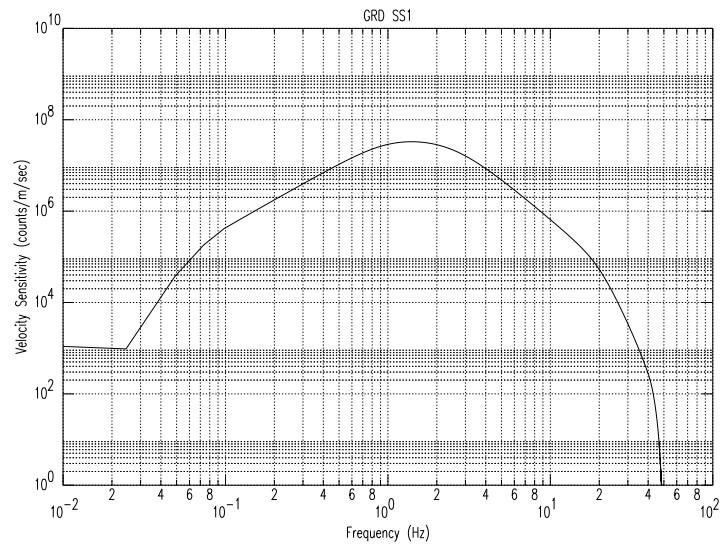


Figure 2.6: Velocity sensitivity for GRD which has the SS-1 seismometer.

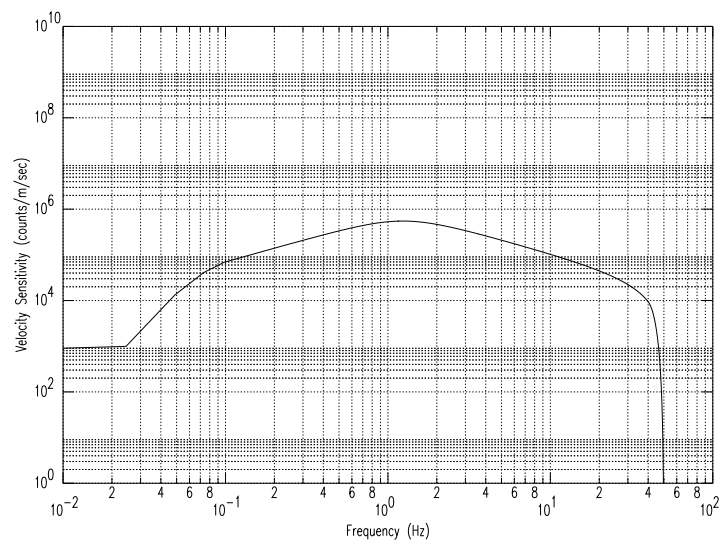


Figure 2.7: Velocity sensitivity for SLC which has the simulated Wood-Anderson response seismometer.

- 3) UUSS multi-component, digital-telemetry, broadband and
- 4) USNSN multi-component, digital-telemetry, broadband sensors.

## 2.2 Instrument response correction

The digital data series were corrected for instrument response to form ground velocity in units of m/sec. This is done by a filtering operation within SAC (Seismic Analysis Code, ..... 19XX, <http://www-ep.es.lnl.gov/tvp/sac.html>). The instrument response was given in the form of SAC pole-zero files for displacement sensitivity in units of counts/micron. To perform the instrument correction to form the desired ground velocity waveforms, we applied the following SAC commands to each trace:

```
rtr
taper
transfer from polezero subtype tresp to none freq 0.25 0.3 20 21
dif
div 1000000
mul GAIN
```

Here we remove the linear trend in the data set, taper the beginning and end of the time series, remove the instrument response given by the file emph(tresp) after bandpass filtering the data between 0.3 - 20 Hz. The result is the displacement time series in units of microns. This is converted to velocity by differentiation, emph(dif), and to units of meters/sec by dividing by the factor 1000000. Corrections for low gain channels used

the same pole-zero file `tresp`, but applied the `emph(GAIN)` multiplication factor. The bandpass filter used within the `emph(transfer)` command is required to ensure stability of the deconvolution process. The band limits are chosen so that they do not interfere with the the bandpass filtering to be performed in the next step of precessing.

Careful correction for instrument response is critical to this study since we will attempt to study the absolute scaling of ground motion generated by the source. The difficulty of maintaining this for regional seismic networks is acknowledged given the large number of field stations and the many instrument settings controlling system gain and frequency response that must be carefully documented. The University of Utah Seismic Networks is quite confident in the transfer functions for the data set provided.

### 3. Data preparation and regression

#### 3.1 Objective of regression analysis

We will perform a regression using a large data set of recordings to obtain the dependence of the ground motion parameters on distance to derive a regional predictive relationship that can be compared to those obtained for other regions.

A general form of the observed ground motion is the multiplicative effect of source, path, and site, which is additive in a logarithmic sense:

$$\log A = SRC(f) + SITE(f) + D(r, f)$$

Using this relationship to describe our observations, we invert the linear system to obtain estimates of source, path (attenuation), and site terms. The propagation term,  $D(r, f)$ , is a function of distance  $r$  and frequency  $f$ . It can be modeled in terms of geometrical spreading  $g(r)$  and frequency dependent anelastic attenuation through a  $Q(f)$  term. Propagation factors such as the existence of geological structures that affect efficient transmission of the seismic energy on a regional scale are included in these two components. The source term,  $SRC(f)$ , reflects the generation of the ground motion by the source and the site term,  $SITE(f)$ , reflects the local modification of the ground motion at the recording site.

Researchers often pre-define the functional dependence of  $g(r)$  for the region of interest. This fundamental assumption often requires  $r^{-1}$  at short distances for body waves and  $r^{-1/2}$  at larger distances for surface waves. Atkinson (1993) used a trilinear geometrical spreading since her data were fit better with an  $r^0$  intermediate trend between the  $r^{-1}$  and  $r^{-1/2}$  trends

at intermediate distances. The choice of distances where the form of the geometrical spreading changes is intimately connected to the final choice of the  $Q(f)$  function. In our work, we defer the choice of  $g(r)$  and  $Q(f)$  to a second stage of processing, and initially require that  $D(r, f)$  be a piecewise linear continuous function which the data are permitted to define.

Because of concerns about instrument response and unknown source and site effects, we also apply the coda normalization technique (Aki, 1980; Frankel et al., 1990) to provide an estimate of the  $D(r, f)$  that should be independent of these unknowns. The coda normalization technique divides the the amplitude of the S or Lg wave amplitude by that of coda wave envelope level. For a linear system, this removes the frequency dependent instrument gain, source excitation, and site amplification effects. The peak S-wave arrival amplitude,  $A_s(r, f)$ , and the RMS coda wave level,  $A_c(f, t_s)$ , at a reference time  $t_s$  is used to compute the ratio:

$$A_{reduced}(r, f) = \frac{A_s(r, f)}{A_c(f, t_s)}$$

which can be modeled as

$$\log[A_{reduced}(r, f)] = D(r, f) - C(f, t_s)$$

where  $A_s(r, f)$  is the peak amplitude of the shear wave, and  $C(f, t_s)$  is coda envelope. Usually  $t_s$  is chosen greater than about twice the direct S wave travel time at which the coda level is independent of the source-receiver distance. Through this procedure, the normalized amplitudes yield an initial  $D(r, f)$ . Therefore, amplitudes of different events and paths can be combined on the same plot for each frequency.

Because the site term may include the effect of unknown instrument response, we hope that the obtained  $D(r, f)$  by coda normalization is an

independent, unbiased estimate of the true  $D(r, f)$ . The path term is forced to be zero at the reference distance at 40 km in this study. The reference distance is usually chosen at a point within the distance distribution of observations. This initial  $D(r, f)$  is used to start a damped least-squares regression to give results of source, site, and distance functions.

### 3.2 Initial data preparation

We only used unclipped and high signal/noise ratio data. The selected waveforms must have both P and S waves. We set origin time, computed distances, and removed the instrument response, as described in Chapter 2.

### 3.3 Trace analysis

For each waveform, the arrival times of P and S waves were picked for two reasons. First to provide a quick check on the event location by using the difference in P- and S-wave arrival times to estimate the epicentral distance. The other reason is that an analysis of peak S-wave motion requires knowledge of where the S wave actually begins.

To study the frequency dependence of ground motion, each waveform was filtered about a center frequency,  $f_c$ , by an 8-pole highpass causal Butterworth filter with corner frequency at  $(\frac{f_c}{\sqrt{2}})$  Hz, followed by an 8-pole lowpass Butterworth filter with corner frequency at  $\sqrt{2}f_c$  Hz. The center frequencies used were 1, 2, 3, 4, 6, 8, 10, 12, 14 and 16 Hz. The peak filtered ground velocity was saved. In addition a duration window was defined in terms of the 5% and 75% bounds of the normalized integral signal-squared

following the S arrival. The signal within this window was Fourier transformed, and a smoothed estimate of the Fourier velocity spectra was made between the two filter corners for each center frequency. For each filter frequency, the peak filtered motion, Fourier velocity spectra, duration and signal envelope were tabulated for use in later processing. The reason for saving this information is to be able to use Random Vibration Theory (Boore, 1983) later which relates spectral amplitudes and duration to peak motion.

### 3.4 Quality control steps for entire data set

The source-receiver distance distribution for the whole dataset is shown in Figure 3.1. The y-axis of the plot displays the station names, and the x-axis shows the source-receiver hypocentral distance. The chosen data set has good overlapping distance sampling by stations which is required for a stable inversion.

### 3.5 Regression

Although the observed ground motion is the multiplicative effect of source, path and site, it is a linear expression in terms of logarithms:

$$A(r, f) = Src(r, f) + Site(r, f) + D(r, f)$$

This equation is now modified to emphasize observations. The logarithm of the observed ground motion parameter is a combined effect of site, excitation, and propagation:

$$PEAK = S(r, f) + E(r, f) + D(r, f)$$





where  $r$  and  $f$  are the hypocentral distance and the observed frequency.  $E(r, f)$  is the excitation term. The term excitation is used since the regression only defines the scaling of observed ground motions and says nothing directly about the seismic source.  $S(r, f)$  represents the site term. The true separation of those terms is hard due to the trade-offs. We use a piecewise linear function (Anderson and Lei, 1994; Harmsen, 1997) to represent the distance dependence of observed motion,  $D(r, f)$ , at a fixed frequency,  $f_c$ :

$$D(r, f_c) = \sum_{i=1}^n L_i(r) D_i$$

where  $L_i(r)$  is a linear interpretation function and  $D_i \equiv D(r_i, f)$  are node values. We prefer to use a large number of nodes,  $n$ , so that the regression can fit any curvature in the actual distance dependence. The ground motion regression model is now written as

$$PEAK = \log A(r, f) = S(r, f) + E(r, f) + \sum_{i=1}^n L_i(r) D_i$$

This linear system can be solved by a least squares inversion using singular value decomposition (SVD). The following constraints are used in this study to reduce the number of degrees of freedom of the system to permit a stable inversion:

- $D(r_{ref}) = 0$ , where  $r_{ref} = 40$  km. The chosen reference distance should be large enough to avoid the effect of source depth error on the hypocentral distance. Since these results will be compared to similar studies in other regions, the reference distance should also be less than distances where regional variations in geometrical spreading predominate.

- $\sum Site(f) = 0$ . There is a direct trade-off between a DC offset in all site terms and the excitation. This is just one of many constraints that could be applied. Often if the geologic site characteristics are known, the constraint  $Site_{rock}(f) = 0$  is used.
- A smoothing constraint is applied to the  $D(r)$ . We use  $D_{l-1} - 2D_l + D_{l+1} = 0$ , which is only a linearity constraint if the  $r_l$  are evenly spaced in which case it approximates a zero second derivative. For unequally spaced nodes, it ensures a uniform variation in slope between adjacent nodes (Herrmann, 2000).

With these constraints, the regression model can be described in words. Given the level of motion at  $r_{ref} = 40km$ , the  $D(r, f)$  propagates that motion to the desired distance,  $r$ , and the site term adjusts that motion to a particular physical location. Other aspects of this model that must be understood are tradeoffs between the excitation, site, and distance terms. Two cases illustrate the problems. First, if one event dominates a distance range, then there will be a tradeoff between the excitation for that event and the adjacent distance terms. This occurs if an event is separated by a distance of the network dimensions from a neighboring event and if the distribution of distance nodes is too dense. A second case occurs if only one station appears in a narrow range of distance it has an anomalous response. In this case the  $D(r)$  will be distorted by this station and a bias introduced in all other site terms by the site term constraint (Herrmann, 2000).

### 3.6 Regression of Fourier Velocity spectra

Figures 3.2, and 3.3 give typical examples of the regression analysis at filter frequencies of 1.0 and 16.0 Hz on the Fourier velocity spectra data set. It also shows the initial propagation term estimated by the coda normalization technique. The initial and final propagation functionals show good agreement for the Fourier velocity spectra data set at all distances at 1.0 Hz and at most distances for 16 Hz. The regression residual plot shows that the distance nodes were appropriate to determine  $D(r)$ .

Figure 3.4 shows the vertical component distance scaling of the  $D(r)$  term at the ten different frequencies for regression on the Fourier velocity spectra. The piecewise linear segments in the  $D(r)$  are now apparent, For clarity the regression error bars on  $D(r)$  are not plotted. This figure is corrected for an  $r^{-1}$  trend to emphasize departure (scattering, deviation) of high frequency spectra with distance from  $r^{-1}$  spreading. As expected the 16 Hz signal decreases more rapidly with distance than lower frequencies. The anomalous spike at 135 km is not accounted for by the error bars and may be the effect of just one anomalous station.

Table 3.1, Table 3.2, and Table 3.3 give the numerical results of our regression on the regional attenuation functional of Fourier Velocity spectra for Utah. They give the corresponding value  $D(r)$  for each frequency and distance as well as the number of observations available at the specific distance (within each distance bin).

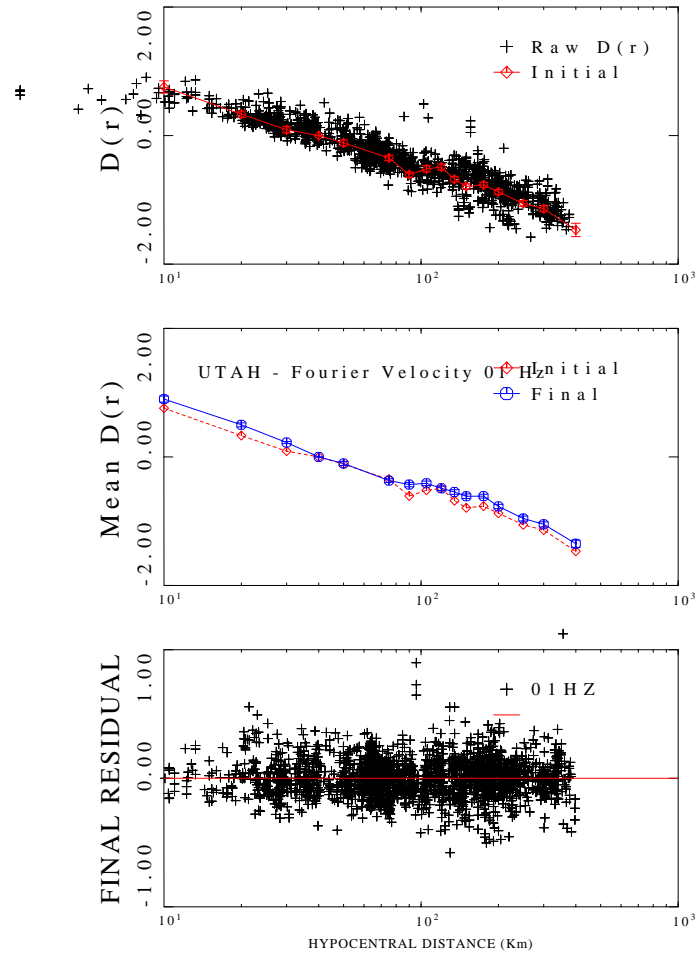


Figure 3.2: Regression analysis for 1.0 Hz. Top, initial estimate of  $D(r)$  using coda normalization technique. Middle, initial and final propagation functionals. Bottom, final residuals of the regression analysis

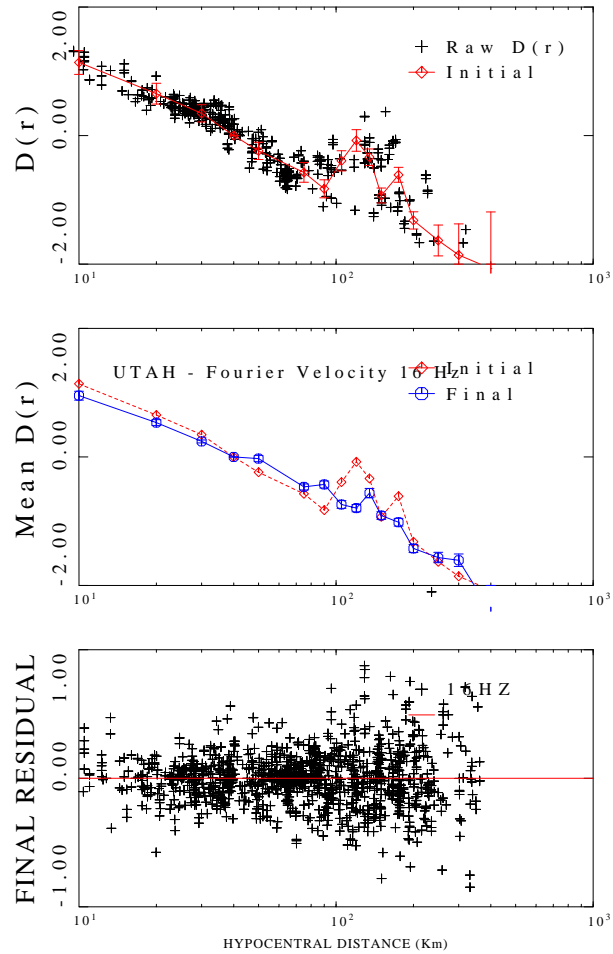


Figure 3.3: Regression analysis for 16 Hz. Top, initial estimate of  $D(r)$  using coda normalization technique. Middle, initial and final propagation functionals. Bottom, final residuals of the regression analysis

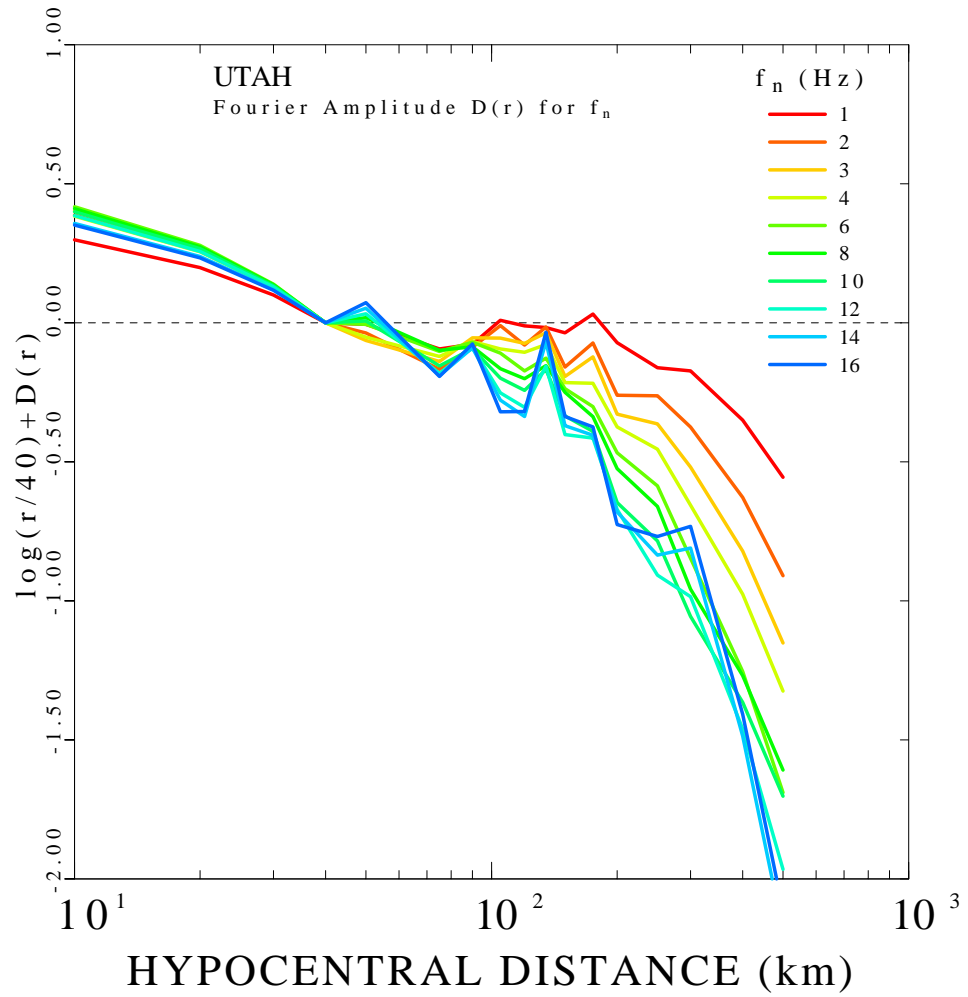


Figure 3.4: Attenuation functional  $D(r, f)$  obtained from the regression of the Fourier amplitudes at the frequencies of 1.0, 2.0, 3.0, 4.0, 6.0, 8.0, 10.0, 12.0, 14.0, and 16.0 Hz. The reference hypocentral distance is at 40 km.

Utah Fourier Velocity Spectra $D(r)$									
f (Hz)	r (km)	$D(r, f)$	$\sigma$	Nobs	f (Hz)	r (km)	$D(r, f)$	$\sigma$	Nobs
1.0	10	0.901	0.047	26.5	2.0	10	0.990	0.040	30.9
1.0	20	0.500	0.032	99.1	2.0	20	0.560	0.027	121.2
1.0	30	0.225	0.016	160.8	2.0	30	0.254	0.013	181.4
1.0	40	0.000	0.000	110.5	2.0	40	0.000	0.000	133.3
1.0	50	-0.102	0.031	308.5	2.0	50	-0.133	0.026	338.9
1.0	75	-0.367	0.028	484.5	2.0	75	-0.440	0.024	530.3
1.0	90	-0.429	0.035	114.5	2.0	90	-0.440	0.028	154.0
1.0	105	-0.410	0.035	98.7	2.0	105	-0.429	0.030	129.4
1.0	120	-0.488	0.035	105.9	2.0	120	-0.557	0.028	144.9
1.0	135	-0.545	0.036	95.5	2.0	135	-0.543	0.030	120.7
1.0	150	-0.610	0.035	124.9	2.0	150	-0.733	0.030	142.6
1.0	175	-0.609	0.031	211.7	2.0	175	-0.713	0.027	236.4
1.0	200	-0.770	0.033	210.3	2.0	200	-0.959	0.029	234.1
1.0	250	-0.957	0.037	114.6	2.0	250	-1.058	0.033	132.3
1.0	300	-1.048	0.039	114.6	2.0	300	-1.250	0.035	117.3
1.0	400	-1.350	0.058	43.5	2.0	400	-1.628	0.053	44.3
3.0	10	1.005	0.039	31.7	4.0	10	0.986	0.037	32.1
3.0	20	0.569	0.026	128.8	4.0	20	0.557	0.025	131.0
3.0	30	0.259	0.013	186.2	4.0	30	0.253	0.013	190.6
3.0	40	0.000	0.000	140.2	4.0	40	0.000	0.000	143.0
3.0	50	-0.160	0.026	347.0	4.0	50	-0.148	0.025	354.8
3.0	75	-0.412	0.023	545.2	4.0	75	-0.394	0.022	547.9
3.0	90	-0.406	0.027	163.9	4.0	90	-0.419	0.026	165.8
3.0	105	-0.474	0.029	133.1	4.0	105	-0.513	0.028	134.8
3.0	120	-0.551	0.028	155.7	4.0	120	-0.583	0.027	157.1
3.0	135	-0.564	0.030	123.7	4.0	135	-0.606	0.029	124.8
3.0	150	-0.767	0.030	145.0	4.0	150	-0.789	0.029	146.6
3.0	175	-0.763	0.026	237.5	4.0	175	-0.858	0.025	237.6
3.0	200	-1.027	0.028	232.9	4.0	200	-1.073	0.027	231.7
3.0	250	-1.159	0.032	131.8	4.0	250	-1.250	0.031	131.6
3.0	300	-1.394	0.034	117.3	4.0	300	-1.531	0.033	117.2
3.0	400	-1.821	0.053	44.3	4.0	400	-1.976	0.051	44.3

Table 3.1: Attenuation functional at 1.0, 2.0, 3.0, and 4.0 Hz for Fourier Velocity spectra. The columns give values of frequency (first and sixth columns), hypocentral distance (second and seventh columns), attenuation  $D(r, f)$  at a reference distance of 40 km (third and eighth columns), associated error bar (fourth and ninth columns) and number of observations (fifth and tenth columns).



Utah Fourier Velocity Spectra $D(r)$									
f (Hz)	r (km)	$D(r, f)$	$\sigma$	Nobs	f (Hz)	r (km)	$D(r, f)$	$\sigma$	Nobs
6.0	10	1.020	0.038	32.3	8.0	10	1.013	0.043	31.3
6.0	20	0.580	0.025	132.5	8.0	20	0.575	0.028	130.5
6.0	30	0.264	0.013	193.4	8.0	30	0.262	0.014	186.5
6.0	40	0.000	0.000	146.2	8.0	40	0.000	0.000	141.6
6.0	50	-0.102	0.025	351.1	8.0	50	-0.078	0.029	312.8
6.0	75	-0.376	0.023	540.7	8.0	75	-0.372	0.026	472.5
6.0	90	-0.422	0.027	167.1	8.0	90	-0.438	0.030	164.9
6.0	105	-0.528	0.029	127.3	8.0	105	-0.584	0.034	116.9
6.0	120	-0.650	0.027	156.5	8.0	120	-0.678	0.030	154.7
6.0	135	-0.655	0.029	125.7	8.0	135	-0.682	0.033	121.2
6.0	150	-0.811	0.029	146.3	8.0	150	-0.824	0.033	142.6
6.0	175	-0.942	0.026	232.6	8.0	175	-0.978	0.029	220.7
6.0	200	-1.166	0.028	226.7	8.0	200	-1.223	0.032	211.9
6.0	250	-1.382	0.032	127.3	8.0	250	-1.456	0.038	112.0
6.0	300	-1.722	0.035	111.8	8.0	300	-1.833	0.040	98.6
6.0	400	-2.254	0.053	42.5	8.0	400	-2.269	0.070	31.3
10.0	10	1.002	0.043	30.3	12.0	10	0.988	0.050	28.9
10.0	20	0.568	0.028	123.2	12.0	20	0.558	0.033	104.1
10.0	30	0.258	0.014	173.2	12.0	30	0.254	0.017	149.7
10.0	40	0.000	0.000	129.6	12.0	40	0.000	0.000	111.7
10.0	50	-0.090	0.030	279.9	12.0	50	-0.064	0.035	244.5
10.0	75	-0.428	0.027	430.9	12.0	75	-0.455	0.032	370.2
10.0	90	-0.445	0.030	154.7	12.0	90	-0.441	0.036	128.0
10.0	105	-0.618	0.034	107.3	12.0	105	-0.671	0.041	83.7
10.0	120	-0.720	0.031	140.1	12.0	120	-0.781	0.038	90.9
10.0	135	-0.696	0.035	101.7	12.0	135	-0.684	0.044	77.8
10.0	150	-0.909	0.034	123.2	12.0	150	-0.976	0.040	100.4
10.0	175	-1.031	0.031	183.4	12.0	175	-1.055	0.038	133.8
10.0	200	-1.345	0.034	182.1	12.0	200	-1.370	0.040	138.1
10.0	250	-1.580	0.040	92.7	12.0	250	-1.703	0.051	65.2
10.0	300	-1.931	0.046	66.5	12.0	300	-1.860	0.059	45.0
10.0	400	-2.365	0.079	22.2	12.0	400	-2.461	0.103	16.1

Table 3.2: Attenuation functional at 6.0, 8.0, 10.0, and 12.0 Hz for Fourier Velocity spectra. The columns give values of frequency (first and sixth columns), hypocentral distance (second and seventh columns), attenuation  $D(r, f)$  at a reference distance of 40 km (third and eighth columns), associated error bar (fourth and ninth columns) and number of observations (fifth and tenth columns).

Utah Fourier Velocity Spectra $D(r)$									
f (Hz)	r (km)	$D(r, f)$	$\sigma$	Nobs	f (Hz)	r (km)	$D(r, f)$	$\sigma$	Nobs
14.0	10	0.960	0.058	28.2	16.0	10	0.954	0.070	27.0
14.0	20	0.540	0.038	90.0	16.0	20	0.535	0.046	86.5
14.0	30	0.244	0.019	133.3	16.0	30	0.242	0.023	122.0
14.0	40	0.000	0.000	97.9	16.0	40	0.000	0.000	87.0
14.0	50	-0.044	0.041	205.5	16.0	50	-0.024	0.049	183.9
14.0	75	-0.463	0.040	304.9	16.0	75	-0.466	0.048	272.2
14.0	90	-0.442	0.044	108.7	16.0	90	-0.428	0.055	89.4
14.0	105	-0.697	0.050	67.6	16.0	105	-0.739	0.061	55.4
14.0	120	-0.814	0.046	71.6	16.0	120	-0.796	0.057	60.2
14.0	135	-0.596	0.060	55.7	16.0	135	-0.562	0.074	48.0
14.0	150	-0.944	0.048	81.6	16.0	150	-0.911	0.060	67.4
14.0	175	-1.045	0.048	98.0	16.0	175	-1.015	0.060	80.3
14.0	200	-1.379	0.050	92.8	16.0	200	-1.424	0.063	68.5
14.0	250	-1.631	0.065	43.6	16.0	250	-1.564	0.081	33.9
14.0	300	-1.685	0.075	32.5	16.0	300	-1.607	0.097	24.5
14.0	400	-2.486	0.134	12.2	16.0	400	-2.408	0.189	8.1

Table 3.3: Attenuation functional at 14.0 and 16.0 Hz for Fourier Velocity spectra. The columns give values of frequency (first and sixth columns), hypocentral distance (second and seventh columns), attenuation  $D(r, f)$  at a reference distance of 40 km (third and eighth columns), associated error bar (fourth and ninth columns) and number of observations (fifth and tenth columns).

### 3.7 Regression of Peak Filtered velocity

Figures 3.5, and 3.6 give typical examples of the regression analysis for the band pass filtered spectra data set at 1.0 and 16.0 Hz. It also shows the initial propagation term estimated from the coda normalization technique. The initial and final propagation functional shows good agreement for the band pass filtered spectra data set. The regression residual plot is used to see if the distance nodes was appropriate to determine  $D(r)$ . Fourier velocity spectra residuals show slightly less scatter than band-pass filtered residuals and residuals of two data sets increase at higher frequencies. Residual values are high at a distance of 135 km for both data sets.

Figure 3.7 shows the vertical component distance scaling of the peak filtered velocity  $D(r)$  term at ten different frequencies for the Utah region.

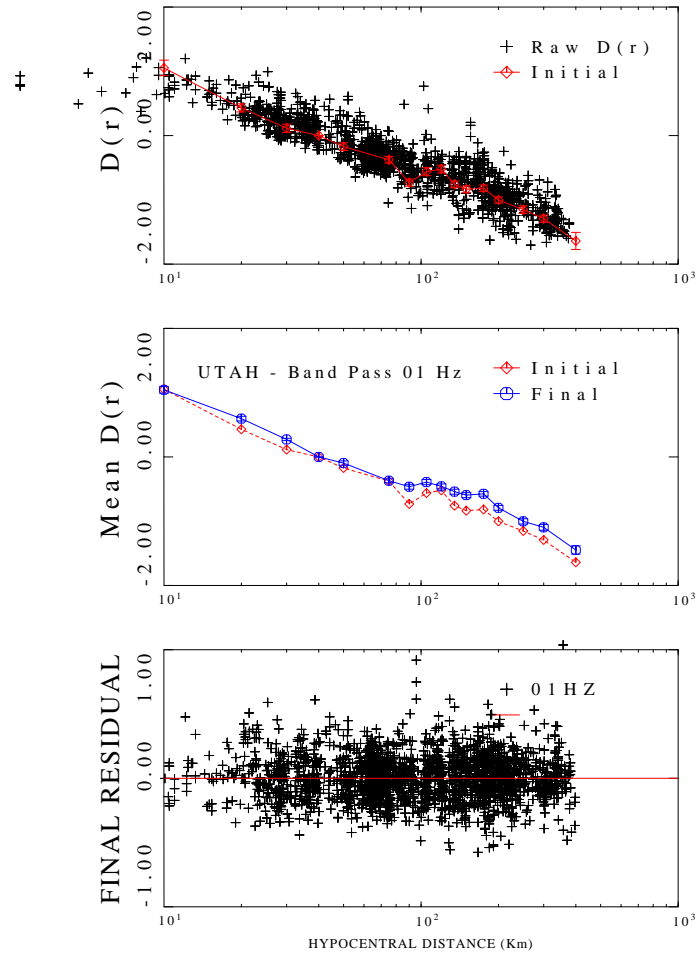


Figure 3.5: Regression analysis for 1.0 Hz. Top, initial estimate of  $D(r)$  using coda normalization technique. Middle, initial and final propagation functionals. Bottom, final residuals of the regression analysis

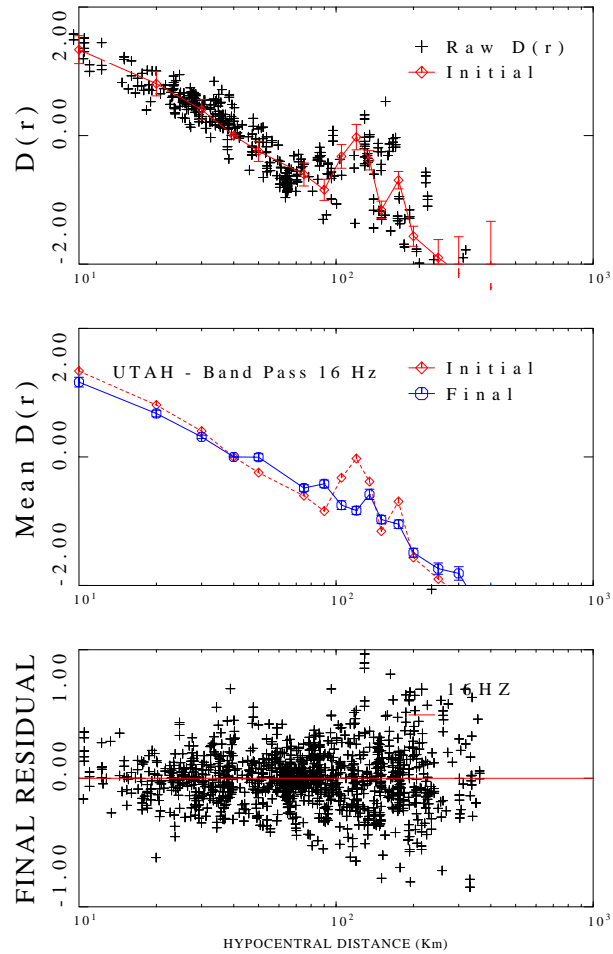


Figure 3.6: Regression analysis for 16 Hz. Top, initial estimate of  $D(r)$  using coda normalization technique. Middle, initial and final propagation functionals. Bottom, final residuals of the regression analysis

This  $D(r)$  values are corrected for an  $r^{-1}$  trend to emphasize departure from simple  $r^{-1}$  spreading.

Table 3.4, Table 3.5, and Table 3.6 give the numerical results of our regression on the regional attenuation functional for the Utah. They give the corresponding value of  $D(r)$  for each frequency and distance as well as the number of observations contributing to each node.

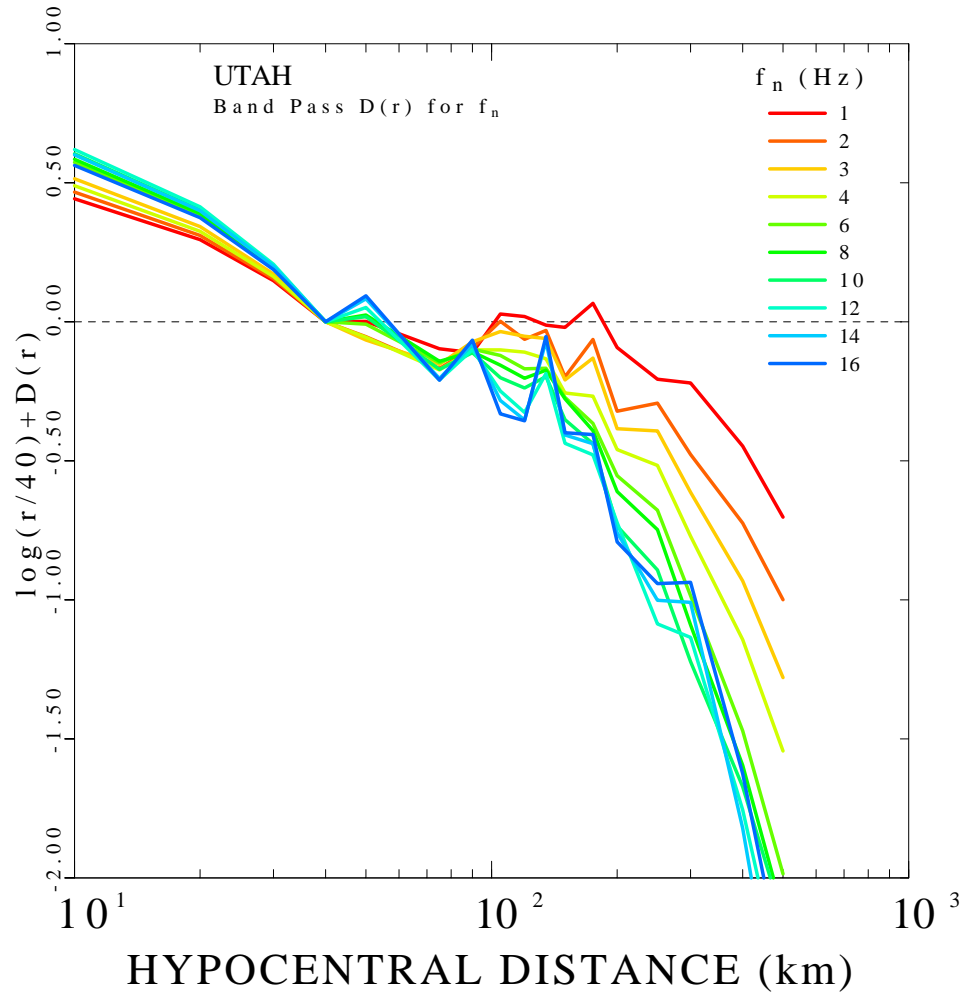


Figure 3.7: Attenuation functional  $D(r, f)$  obtained from the regression of the filtered velocities at the frequencies of 1.0, 2.0, 3.0, 4.0, 6.0, 8.0, 10.0, 12.0, 14.0, and 16.0 Hz. The reference hypocentral distance is at 40 km.

Utah Filtered Velocity D(r)									
f (Hz)	r (km)	$D(r, f)$	$\sigma$	Nobs	f (Hz)	r (km)	$D(r, f)$	$\sigma$	Nobs
1.0	0	0.000	0.000	0.0	0	0	0	0	0
1.0	10	1.045	0.053	26.5	2.0	10	1.069	0.048	30.9
1.0	20	0.597	0.035	99.1	2.0	20	0.612	0.032	121.2
1.0	30	0.273	0.018	160.8	2.0	30	0.280	0.016	181.4
1.0	40	0.000	0.000	110.5	2.0	40	0.000	0.000	133.3
1.0	50	-0.095	0.034	308.5	2.0	50	-0.150	0.032	338.9
1.0	75	-0.370	0.031	484.5	2.0	75	-0.441	0.029	530.0
1.0	90	-0.463	0.038	114.5	2.0	90	-0.446	0.034	154.0
1.0	105	-0.391	0.039	98.7	2.0	105	-0.417	0.036	129.4
1.0	120	-0.458	0.038	105.9	2.0	120	-0.540	0.034	144.9
1.0	135	-0.540	0.040	95.5	2.0	135	-0.559	0.036	120.7
1.0	150	-0.594	0.039	124.9	2.0	150	-0.772	0.036	142.6
1.0	175	-0.574	0.034	211.7	2.0	175	-0.704	0.032	236.4
1.0	200	-0.791	0.037	210.3	2.0	200	-1.020	0.034	234.1
1.0	250	-1.002	0.042	114.6	2.0	250	-1.088	0.039	132.3
1.0	300	-1.095	0.043	114.6	2.0	300	-1.352	0.042	117.3
1.0	400	-1.447	0.064	43.5	2.0	400	-1.724	0.064	44.3
3.0	10	1.117	0.047	31.7	4.0	10	1.092	0.046	32.1
3.0	20	0.644	0.031	128.8	4.0	20	0.627	0.030	131.0
3.0	30	0.297	0.016	186.2	4.0	30	0.288	0.015	190.6
3.0	40	0.000	0.000	140.2	4.0	40	0.000	0.000	143.0
3.0	50	-0.162	0.031	347.0	4.0	50	-0.152	0.030	354.8
3.0	75	-0.426	0.028	545.2	4.0	75	-0.446	0.027	547.9
3.0	90	-0.424	0.033	163.9	4.0	90	-0.453	0.032	165.8
3.0	105	-0.454	0.035	133.1	4.0	105	-0.520	0.034	134.8
3.0	120	-0.529	0.033	155.7	4.0	120	-0.586	0.033	157.1
3.0	135	-0.588	0.036	123.7	4.0	135	-0.661	0.035	124.8
3.0	150	-0.783	0.036	145.0	4.0	150	-0.830	0.035	146.6
3.0	175	-0.771	0.032	237.5	4.0	175	-0.908	0.031	237.6
3.0	200	-1.083	0.034	232.9	4.0	200	-1.158	0.033	231.7
3.0	250	-1.188	0.039	131.8	4.0	250	-1.312	0.038	131.6
3.0	300	-1.488	0.042	117.3	4.0	300	-1.646	0.041	117.2
3.0	400	-1.932	0.064	44.3	4.0	400	-2.143	0.062	44.3

Table 3.4: Distance functional at 1.0, 2.0, 3.0, and 4.0 Hz for Band-Passed filtered. The columns give values of frequency (first and sixth columns), hypocentral distance (second and seventh columns), attenuation  $D(r, f)$  at a reference distance of 40 km (third and eighth columns), associated error bar (fourth and ninth columns) and number of observations (fifth and tenth columns).

Utah Filtered Velocity D(r)									
f (Hz)	r (km)	D(r, f)	$\sigma$	Nobs	f (Hz)	r (km)	D(r, f)	$\sigma$	Nobs
6.0	10	1.176	0.045	32.3	8.0	10	1.187	0.050	31.3
6.0	20	0.684	0.030	132.5	8.0	20	0.691	0.033	130.5
6.0	30	0.316	0.015	193.4	8.0	30	0.320	0.017	186.5
6.0	40	0.000	0.000	146.2	8.0	40	0.000	0.000	141.6
6.0	50	-0.105	0.030	351.1	8.0	50	-0.072	0.034	312.8
6.0	75	-0.420	0.027	540.7	8.0	75	-0.415	0.031	472.5
6.0	90	-0.450	0.032	167.1	8.0	90	-0.460	0.035	164.9
6.0	105	-0.540	0.035	127.3	8.0	105	-0.575	0.040	116.9
6.0	120	-0.646	0.033	156.5	8.0	120	-0.680	0.035	154.7
6.0	135	-0.695	0.035	125.7	8.0	135	-0.702	0.039	121.2
6.0	150	-0.846	0.035	146.3	8.0	150	-0.851	0.038	142.6
6.0	175	-1.006	0.031	232.6	8.0	175	-1.032	0.035	220.7
6.0	200	-1.252	0.034	226.7	8.0	200	-1.309	0.038	211.9
6.0	250	-1.473	0.039	127.3	8.0	250	-1.543	0.044	112.0
6.0	300	-1.860	0.042	111.8	8.0	300	-1.965	0.047	98.6
6.0	400	-2.471	0.064	42.5	8.0	400	-2.595	0.083	31.3
10.0	10	1.207	0.051	30.3	12.0	10	1.222	0.058	28.9
10.0	20	0.704	0.034	123.2	12.0	20	0.715	0.038	104.1
10.0	30	0.327	0.017	173.2	12.0	30	0.332	0.019	149.7
10.0	40	0.000	0.000	129.6	12.0	40	0.000	0.000	111.7
10.0	50	-0.078	0.035	279.9	12.0	50	-0.045	0.040	244.5
10.0	75	-0.444	0.032	430.9	12.0	75	-0.482	0.037	370.2
10.0	90	-0.463	0.036	154.7	12.0	90	-0.452	0.042	128.0
10.0	105	-0.620	0.041	107.3	12.0	105	-0.668	0.048	83.7
10.0	120	-0.715	0.037	140.1	12.0	120	-0.803	0.044	90.9
10.0	135	-0.725	0.042	101.7	12.0	135	-0.714	0.051	77.8
10.0	150	-0.926	0.041	123.2	12.0	150	-1.011	0.046	100.4
10.0	175	-1.079	0.037	183.4	12.0	175	-1.119	0.043	133.8
10.0	200	-1.433	0.040	182.1	12.0	200	-1.421	0.046	138.1
10.0	250	-1.688	0.048	92.7	12.0	250	-1.882	0.059	65.2
10.0	300	-2.097	0.055	66.5	12.0	300	-2.010	0.069	45.0
10.0	400	-2.672	0.095	22.2	12.0	400	-2.755	0.120	16.1

Table 3.5: Distance functional at 6.0, 8.0, 10.0, and 12.0 Hz for Band-Passed Filtered. The columns give values of frequency (first and sixth columns), hypocentral distance (second and seventh columns), attenuation  $D(r,f)$  at a reference distance of 40 km (third and eighth columns), associated error bar (fourth and ninth columns) and number of observations (fifth and tenth columns).



Utah Filtered Velocity D(r)									
f (Hz)	r (km)	$D(r, f)$	$\sigma$	Nobs	f (Hz)	r (km)	$D(r, f)$	$\sigma$	Nobs
14.0	10	1.203	0.065	28.2	16.0	10	1.165	0.075	27.0
14.0	20	0.701	0.043	90.0	16.0	20	0.676	0.050	86.5
14.0	30	0.325	0.022	133.3	16.0	30	0.313	0.025	122.0
14.0	40	0.000	0.000	97.9	16.0	40	0.000	0.000	87.0
14.0	50	-0.014	0.047	205.5	16.0	50	-0.003	0.053	183.9
14.0	75	-0.477	0.045	304.9	16.0	75	-0.483	0.052	272.2
14.0	90	-0.433	0.049	108.7	16.0	90	-0.418	0.060	89.4
14.0	105	-0.702	0.056	67.6	16.0	105	-0.750	0.066	55.4
14.0	120	-0.830	0.051	71.6	16.0	120	-0.833	0.062	60.2
14.0	135	-0.597	0.067	55.7	16.0	135	-0.581	0.080	48.0
14.0	150	-0.981	0.055	81.6	16.0	150	-0.973	0.065	67.4
14.0	175	-1.079	0.054	98.0	16.0	175	-1.046	0.065	80.3
14.0	200	-1.457	0.057	92.8	16.0	200	-1.490	0.069	68.5
14.0	250	-1.797	0.073	43.6	16.0	250	-1.737	0.088	33.9
14.0	300	-1.884	0.085	32.5	16.0	300	-1.812	0.105	24.5
14.0	400	-2.821	0.151	12.2	16.0	400	-2.625	0.205	8.1

Table 3.6: Distance functional at 14.0 and 16.0 Hz for Band-Passed Filtered. The columns give values of frequency (first and sixth columns), hypocentral distance (second and seventh columns), attenuation  $D(r, f)$  at a reference distance of 40 km (third and eighth columns), associated error bar (fourth and ninth columns) and number of observations (fifth and tenth columns).

### 3.8 Duration

The duration of strong ground motion can have a strong influence on earthquake damage. A ground motion with moderate amplitude but long duration can produce enough load reversals to cause substantial damage (Kramer, 1996). Properly studied observed ground motions enable us to characterize the distance and frequency band influence on duration.

Duration is a function of the rupture and of the dispersion that elastic waves experience along source and receivers paths (Herrmann, 1985). Scattering also contributes to the increase in duration at increasing distances from the source. Dispersion redistributes the frequency content of the radiated spectrum (Malagnini, 1999) in time. As a result, the duration increases with increasing earthquake magnitude and distance. Trifunac

and Brady (1975) define duration on the time interval between the points at which 5 % and 95 % of the total energy has been recorded. Various other estimates duration (T) are fully described in Kramer (1996). Only the strong-motion portion of the accelerogram is important for engineering purposes.

We used integrated square filtered velocity to estimate signal duration. Integration starts at the S arrival time and continues into the coda. The signal within 5 % - 75 % limits is Fourier transformed and RMS averaged between the filter corners to yield the Fourier velocity spectra in *meters*. Thus the Fourier velocity spectra observation is intimately related to the duration determination (Raouf et al, 1999).

We used the 5 % - 75 % duration of the seismic ground motion throughout this study for all the available recording. Raouf et al., (1999) used 5 % - 75 % duration window and test results indicated that it provided better agreement between observed and RVT predicted peak values instead of using 5 % - 95 % duration. The advantage using a duration based on the 5 - 75 % integral rather than 5 - 95 % of Atkinson and Boore (1995) is discussed by Raouf et al. (1999).

Figures 3.8 and 3.9 show the observed durations at 1.0 and 16.0 Hz. We noted significant scatter at 1.0 Hz which decreased at higher frequencies. At higher frequencies though, small signals due to attenuation did not permit a reliable estimation of duration at large distance.

To estimate the distance dependence of duration, we modeled it as a piecewise linear function of distance.

$$T(r) = \int_{l=1}^L T_l N_l(r)$$

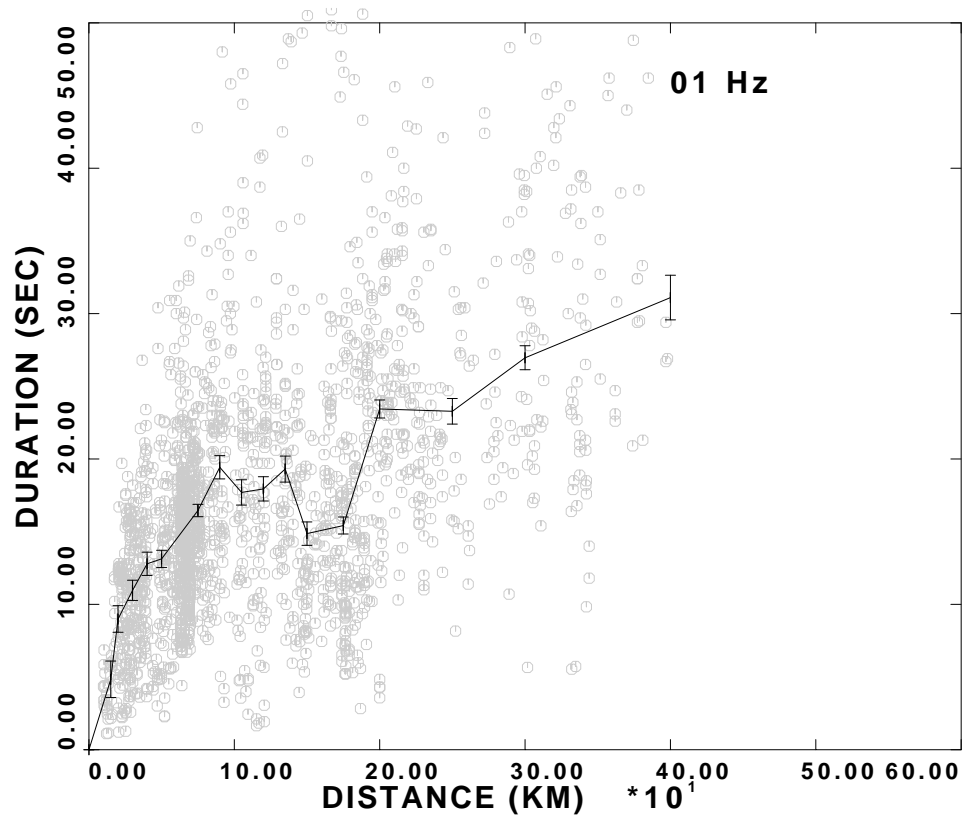


Figure 3.8: Duration data and regression lines as a function of distance for filter frequency of 1.0 Hz

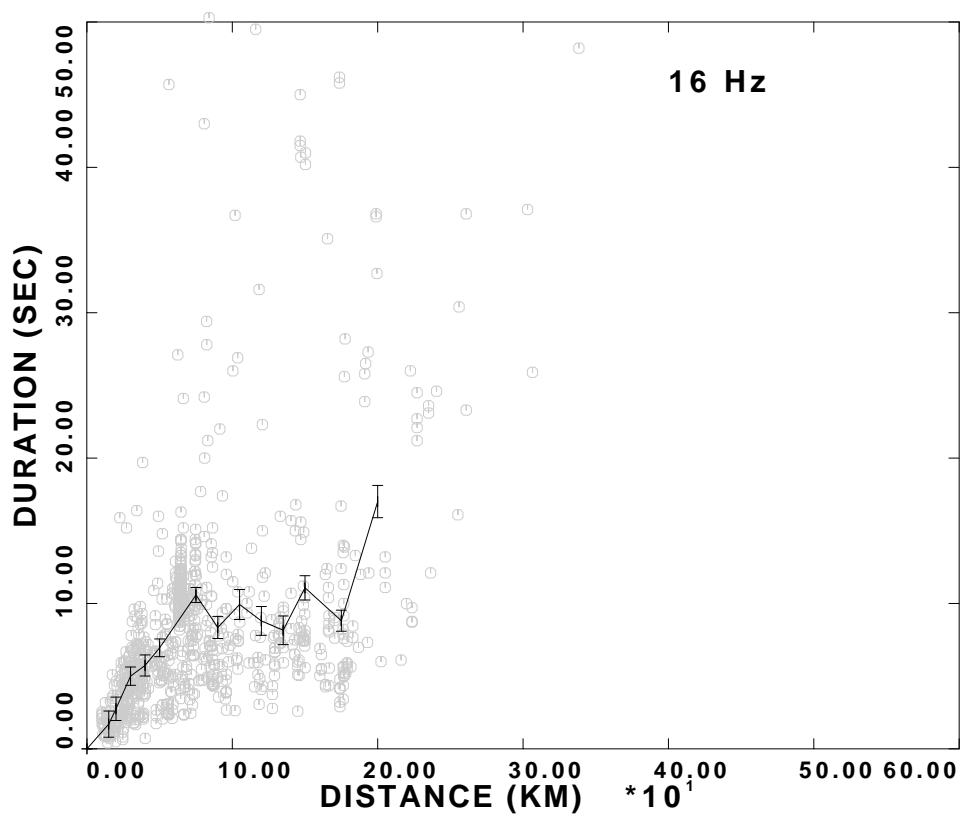


Figure 3.9: Duration data and regression lines as a function of distance for filter frequency of 16 Hz

The only constraint is that  $T(r = 0km) = 0$  which we feel appropriate for small earthquakes. We solved this by least-squares even though Malagnini (1999) proposed the use of an L1 norm because of the scatter. To determine the  $T(r)$  duration function, we assumed the measured duration is relatively insensitive to event size for small earthquakes. RVT predictions depend on the assumed signal duration:

$$T_s + T(r)$$

where  $T_s$  is the source contribution and  $T(r)$  is the distance dependent wave propagation contribution to total duration. Predictions for larger earthquakes will use a sufficiently large  $T_s$  that overwhelms the  $T(r = 0km) = 0$  constraint at short distance (Herrmann, 1985). The least squares fits are plotted in Figures 3.8 and 3.9. The  $T(r)$  functional are compared in Figure 3.10 for all the filter frequencies and tabulated in Table 3.7. There is much scatter in the automatic determination of scattering because of the rapid decrease of high frequency signals with distance. We can only determine the 16 Hz duration reliably out to 250 km. The 1 Hz values are observed at large distances, but show a lot of scatter. This is similar to the observations of Raoof et al. (1999). The dark line is adequate for describing all frequencies greater than 1.0 Hz except near 75 km, which may be affected by mining related events at that distance.

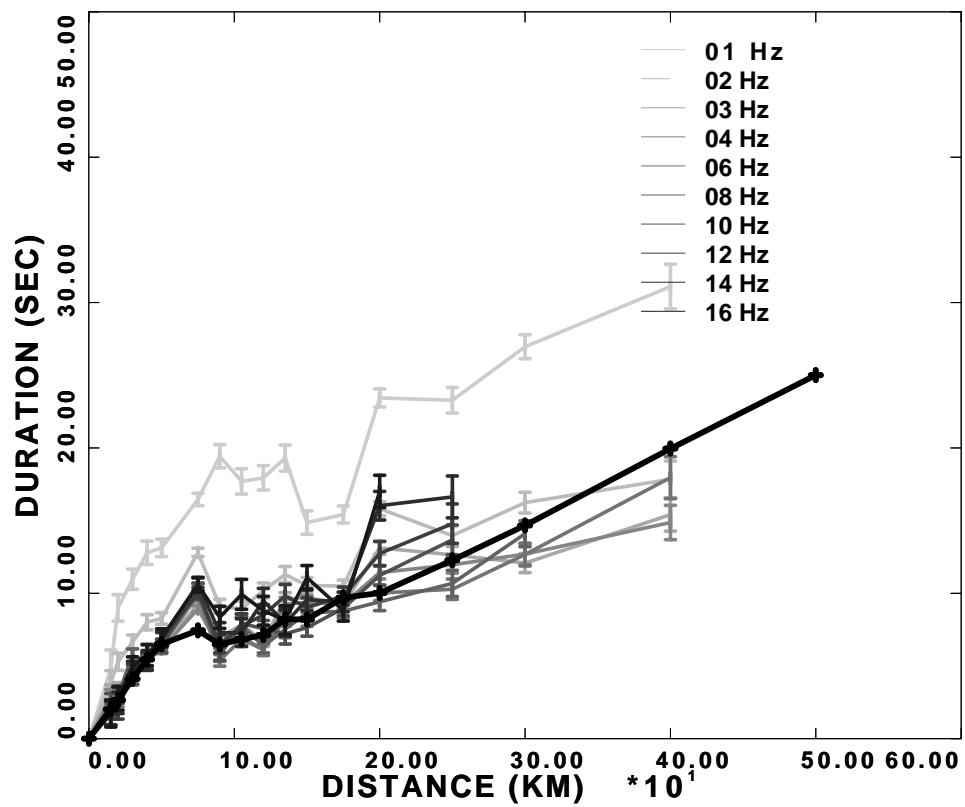


Figure 3.10: Distance dependence of duration for filtered data at the different frequencies. Thick black line is a total duration estimation for frequencies

Durations for different frequencies (Hz)											
Distance(km)	01	02	03	04	06	08	10	12	14	16	FINAL
0	0	0	0	0	0	0	0	0	0	0	0
15	4.8	3.9	3.0	2.7	2.0	1.7	2.3	1.8	1.8	1.7	2.0
20	9.0	5.3	3.3	3.0	2.6	3.0	3.0	2.0	2.5	2.7	2.6
30	10.9	6.6	4.6	4.1	4.1	5.7	4.2	4.6	4.7	5.0	4.1
40	12.8	8.0	6.1	5.4	5.4	5.3	5.4	5.3	5.4	5.7	5.4
50	13.1	8.3	6.5	6.2	6.5	6.3	6.4	6.8	6.8	7.0	6.5
75	16.5	12.8	9.2	8.9	9.8	10.3	10.4	10.0	10.6	10.6	7.5
90	19.4	9.1	7.0	6.3	5.4	5.7	5.9	6.5	7.3	8.3	6.5
105	17.7	8.9	7.8	7.0	6.8	7.8	7.9	7.7	7.3	9.9	6.8
120	17.9	10.2	6.7	6.1	6.1	6.3	7.6	8.5	9.5	8.8	7.1
135	19.3	11.3	9.6	9.3	8.2	7.5	7.2	9.8	8.0	8.2	8.2
150	14.9	10.5	9.7	9.4	8.2	8.6	7.6	9.0	9.5	11.1	8.2
175	15.4	10.5	9.2	9.3	9.7	8.8	9.0	9.8	9.4	8.8	9.7
200	23.4	15.8	13.1	11.4	10.0	9.4	11.2	12.7	16.0	17.0	10.0
250	23.3	14.0	12.7	12.0	10.3	10.7	13.7	14.8	16.6	-	12.3
300	27.0	16.2	12.1	12.7	12.7	14.1	-	-	-	-	20.0
400	31.1	17.8	15.4	14.9	17.9	-	-	-	-	-	25.0

Table 3.7: Durations as a function of distance and frequency ranges from 01 to 16 Hz.

### 3.9 Excitation

After careful observation, I noticed that the initial plots of excitation,  $E(f)$ , showed two different populations and decided to separate the excitation in two groups. We applied a simple sieve to the excitation terms by asking whether the 10 Hz level was significantly beneath the 3.0 Hz level. This sieve gives the important clue for separating mining related events from earthquakes.

Figures 3.11 and 3.13 show the excitations at 40 km of earthquakes obtained from the regressions on the Fourier velocity and band passed peak amplitudes. Figures 3.12 and 3.14 represent the explosion induced excitations at 40 km for the Fourier velocity and band passed peak amplitudes. This automatic process seems to have left a few mining related events in the earthquake population at Figures 3.11 and 3.13.

For either source, the shapes of the Fourier velocity and filtered veloc-

ity excitation are different. This is due to the fact that the filtered bandwidth used with frequency. Forward modeling will account for this. The differences in frequency dependent excitation between the sources is obvious. The mining related events have significantly reduced excitation as a function of increasing frequency. This may be due to differences between the earthquake source and the deep mine collapses mechanisms and/or source term function.

Figures 3.15 and 3.16 shows the earthquake and mining induced epicenter maps in the study area. The epicenters of Figure 3.16 are those have mining induced spectra in Figures 3.12 and 3.14, while Figure 3.15 shows locations of presumed earthquakes. Note that there is a narrow grouping of mining related events. After personal communication with Walter Arabasz at the SSA 2000 meeting in San Diego, I realized that mines of the Colorado Plateau use room-and-pillar methods instead of blasting for underground mining (Arabasz and McCarter, 2000). The subsequent mine collapse may be triggered by small, nearby tectonic earthquakes collapse or self-initiated collapse. Therefore, mining related events differ from conventional earthquakes by a rapid drop of high frequency excitation spectra and lack of Love wave excitation (Pechmann et al., 1995).

Because of concern about the effect of mining sources on our regression, we separated them from the data set and redid the regression for  $D(r, f)$ . We did not see significant differences in the results. In the next chapter we will model the  $D(r, f)$  from the entire data set.



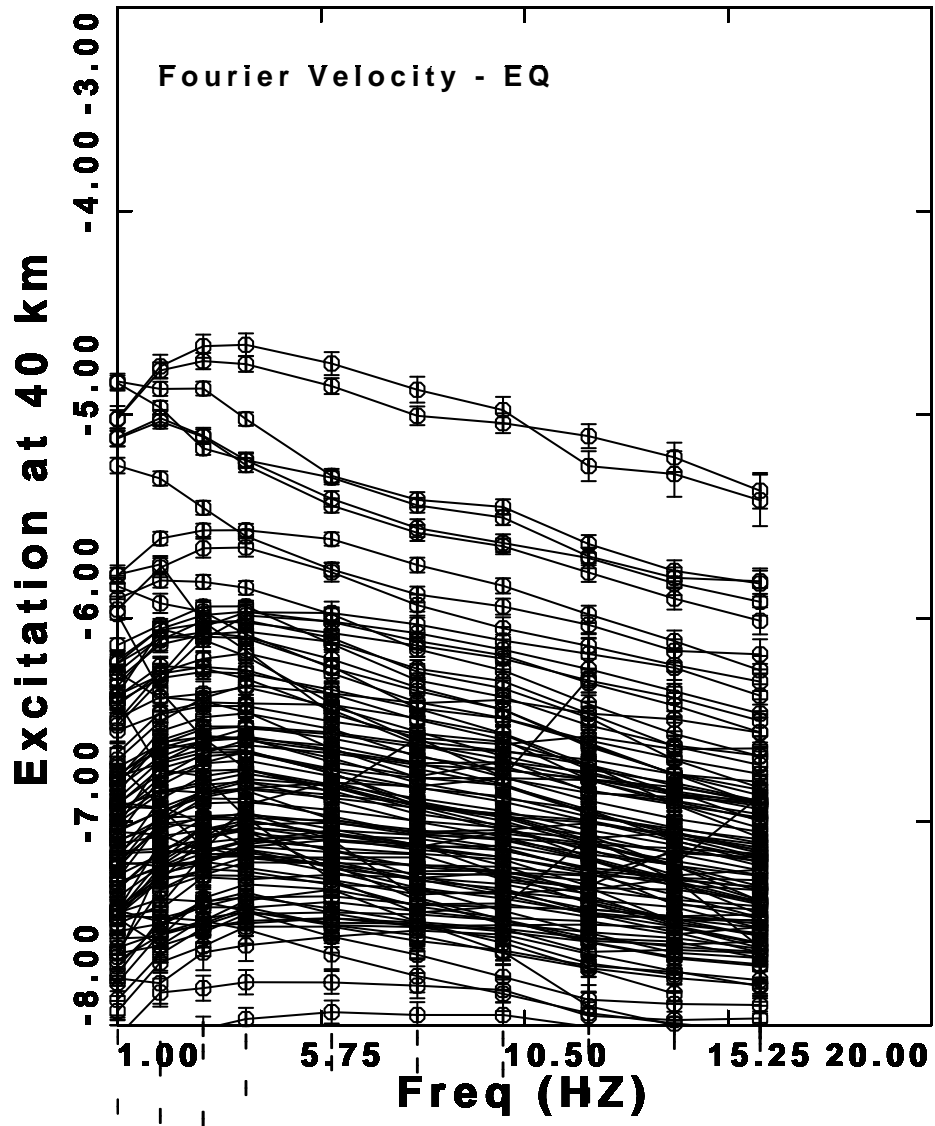


Figure 3.11: Inverted Fourier velocity excitation terms for the earthquake events recorded by vertical component velocity seismograms plotted on a linear frequency scale

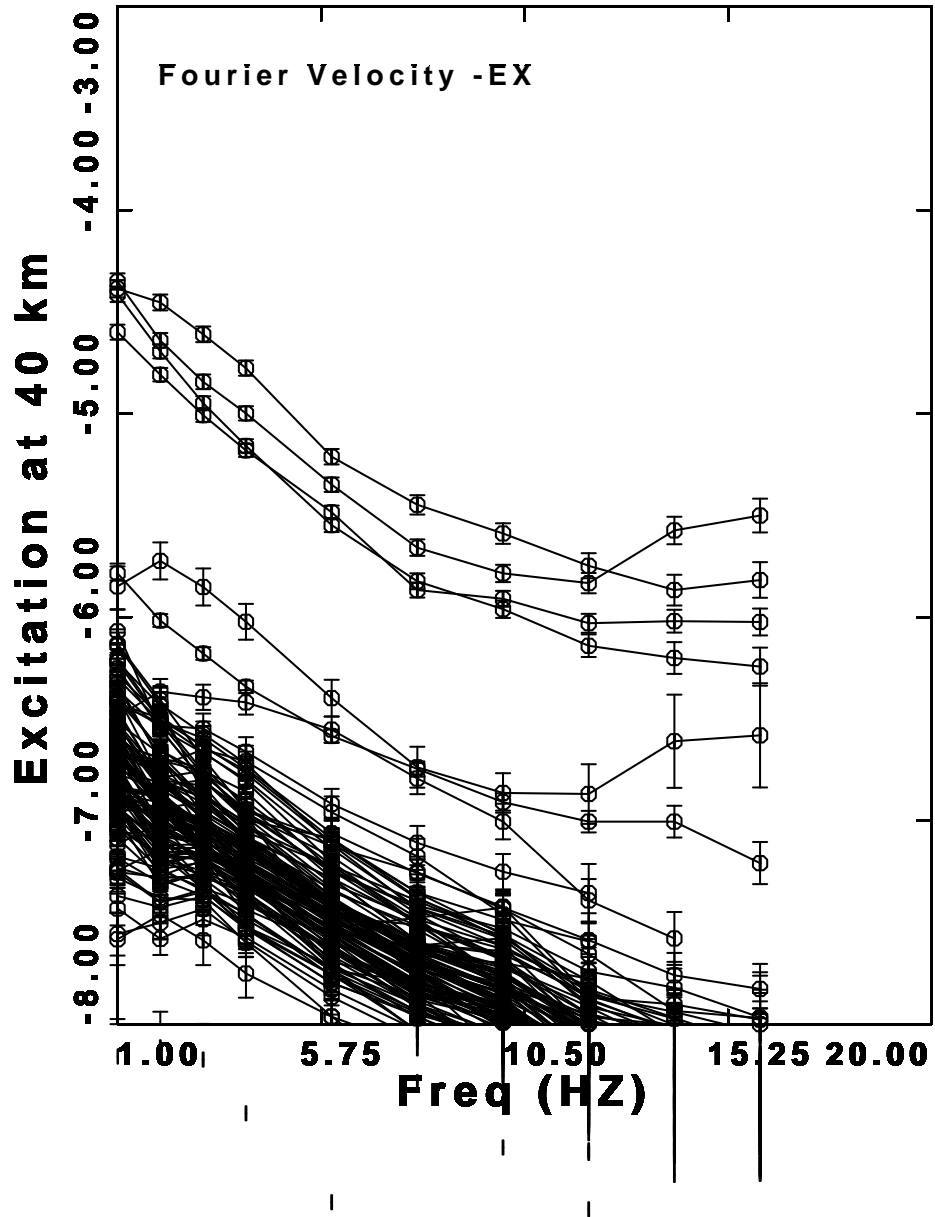


Figure 3.12: Inverted Fourier velocity excitation terms for the mining related events recorded by vertical component velocity seismograms plotted on a linear frequency scale

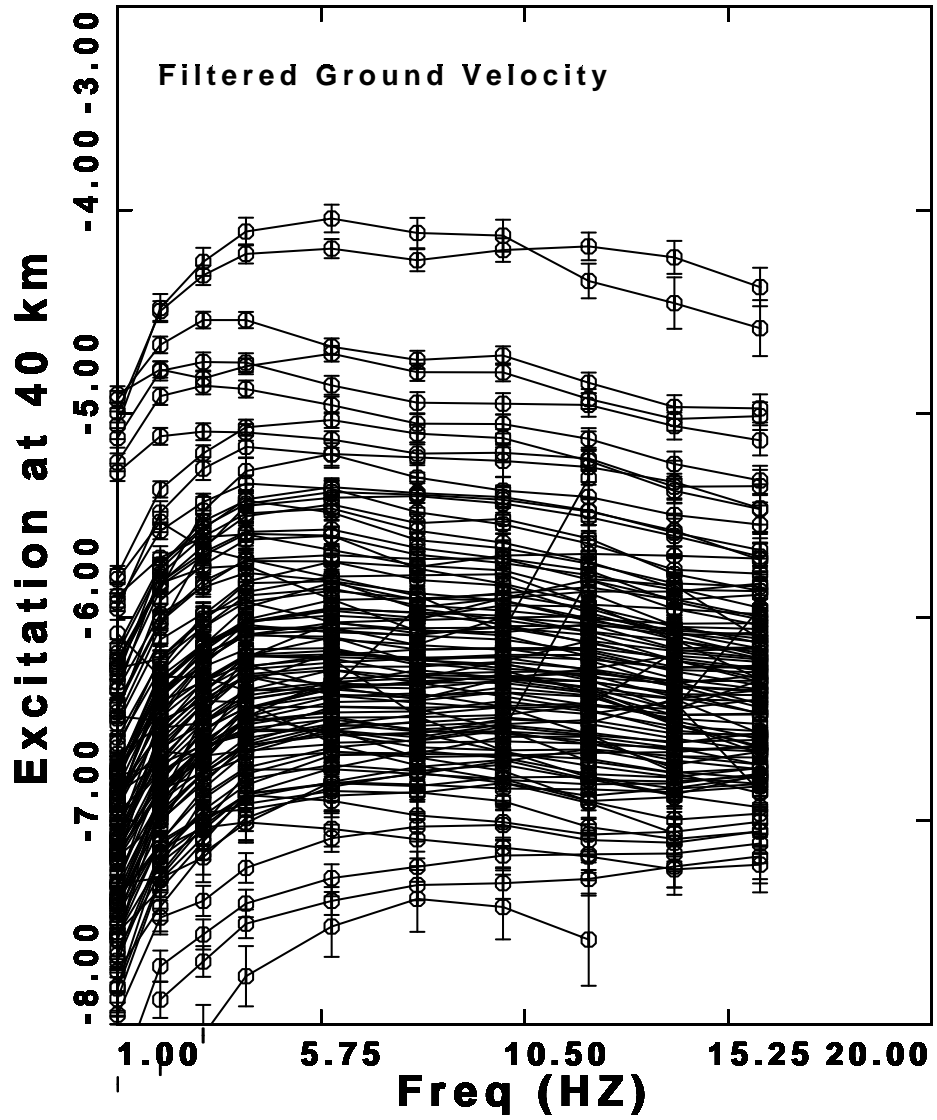


Figure 3.13: Inverted Filtered ground velocity excitation terms for the earthquake events recorded by vertical component velocity seismograms plotted on a linear frequency scale

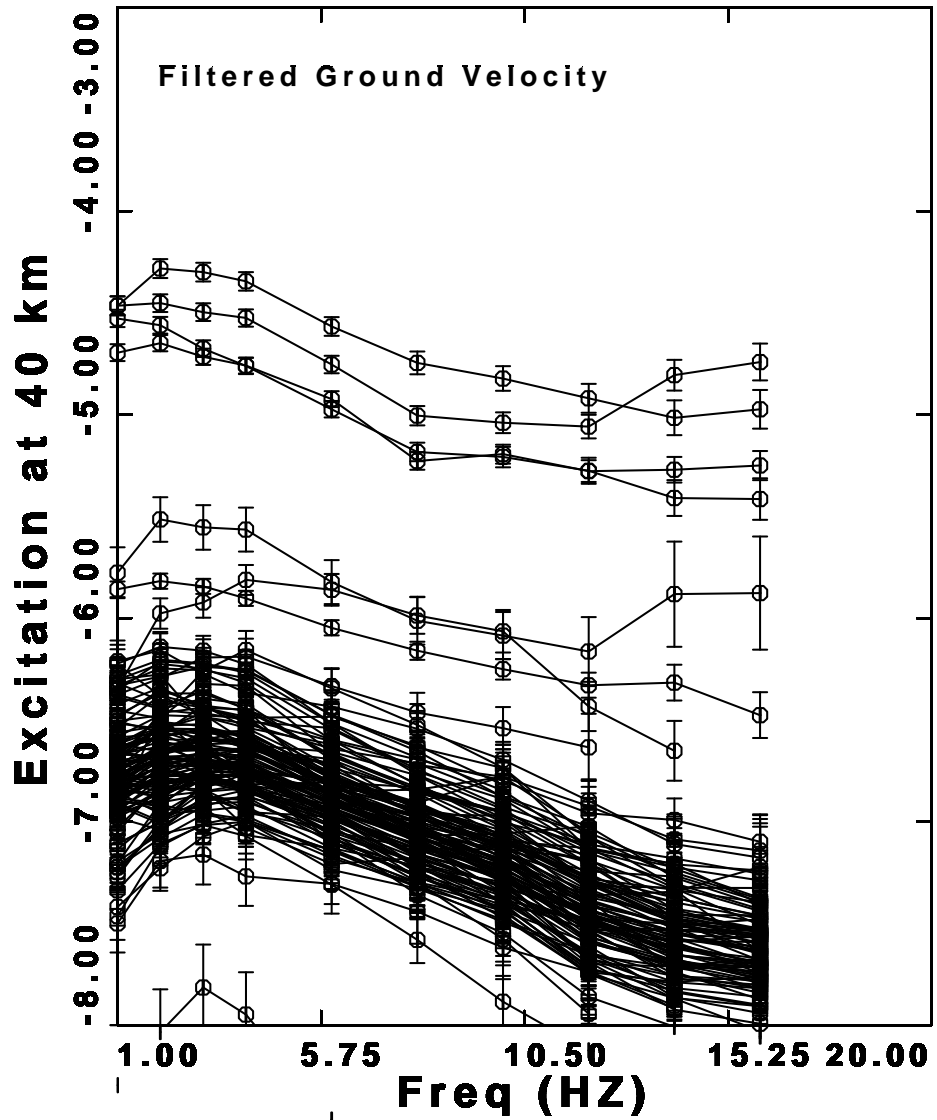


Figure 3.14: Inverted Filtered ground velocity excitation terms for the mining related events recorded by vertical component velocity seismograms plotted on a linear frequency scale

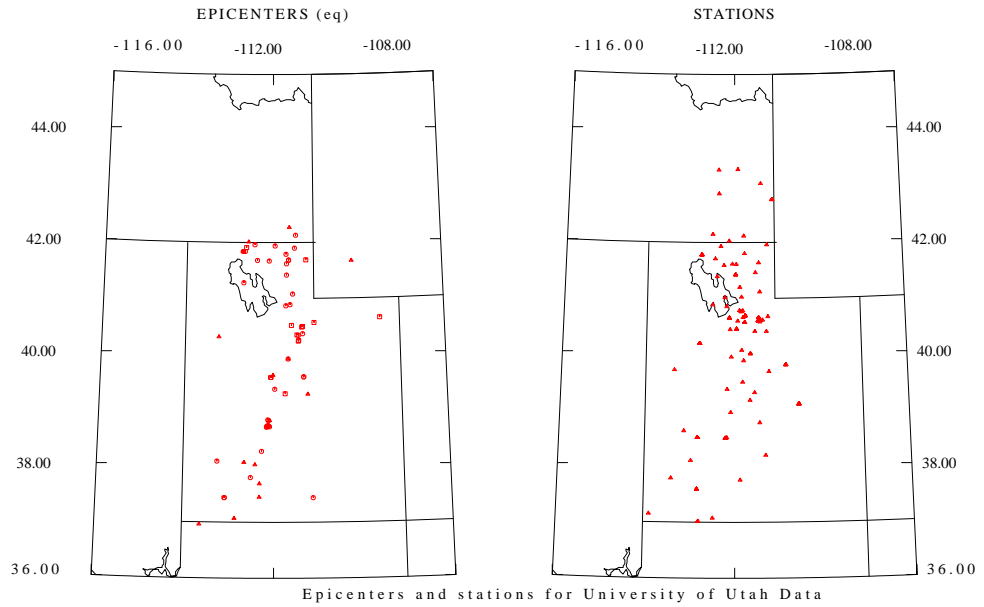


Figure 3.15: Map showing the earthquake-epicenters and stations for University of Utah data

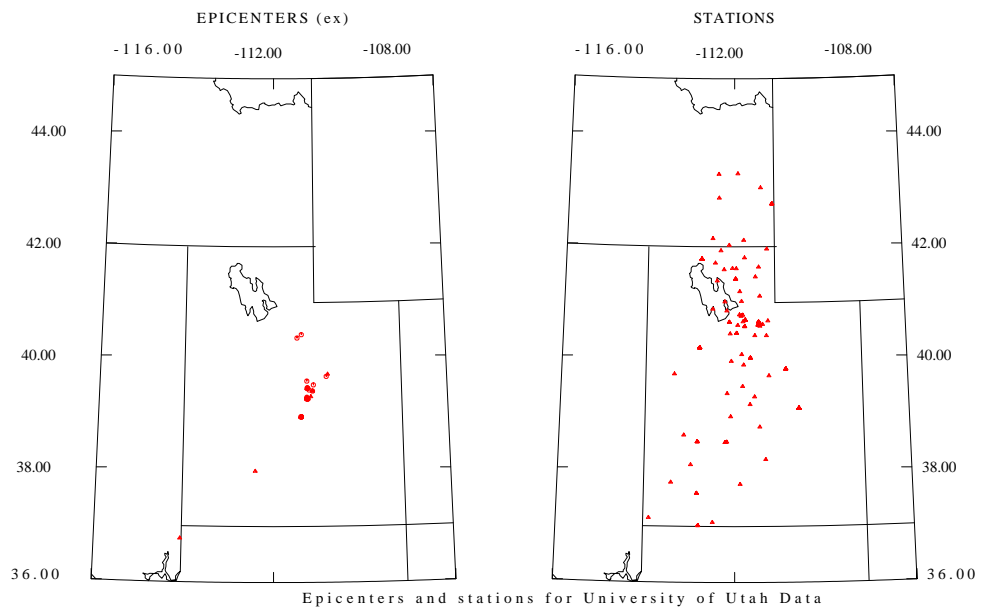


Figure 3.16: Map showing the explosion induced epicenters and stations for University of Utah data

## 4. Parameterization

The previous chapter presented the regression results. The purpose of this chapter is to model those results in terms of a simple physically based model which reduces the observations to a few parameters. This parameterization is an essential step toward creating a forward ground motion prediction model.

### 4.1 Modeling Fourier velocity spectra

An equation for the predicted Fourier velocity spectra for a frequency  $f$  at a distance  $r$  is

$$a(r, f) = S(f, M_w)F(f)g(r)e^{-\pi fr/Q(f)\beta}V(f)e^{-\pi f\kappa}$$

where  $a(r, f)$  is the Fourier velocity spectra,  $S(f, M_w)$  is the source excitation as a function of moment-magnitude,  $F(f)$  is a filter that converts ground motion to the desired motion,  $g(r)$  is the geometrical spreading function, and  $Q(f)$  is the frequency dependent quality factor which is taken to be  $Q_0(f/1.0)^\eta$  and  $Q_0$  is the quality factor at 1.0 Hz.  $V(f)$  is a frequency dependent site amplification that accounts for the site velocity structure while  $\kappa$  controls site attenuation of high frequency. The filter function  $F(f)$  can represent the lightly damped single degree-of-freedom oscillator used for computing response spectra, a simple operator to give ground velocity, displacement or acceleration or an instrument response. A comparison of this simple prediction model to the regression terms shows the following correspondence:

$$10^E \quad S(f, M_w)F(f)g(r_{ref})e^{-\pi fr_{ref}/Q(f)\beta}\overline{V(f)}e^{-\pi\kappa f}$$

for  $r = r_{ref}$

$$10^D \quad \frac{g(r)e^{-\pi fr/Q(f)\beta}}{g(r_{ref})e^{-\pi fr_{ref}/Q(f)\beta}}$$

$$10^{S_i} \quad \frac{V(f)e^{-\pi\kappa f}}{\overline{V(f)e^{-\pi\kappa f}}}$$

where  $\overline{V(f)e^{-\pi\kappa f}}$  is the network average site effect (Herrmann, 2000). By construction these expressions incorporate the regression constraints used in the previous chapter. The parameters used are phenomenological in that they describe an aspect of ground motion scaling but may not be the true physical values. For example, the  $Q(f)$  will tradeoff with the  $g(r)$  if the data set consists of only finite distance and frequency ranges.

From the second of these equations, we see that the  $D(r, f)$  term is a function of the geometrical spreading  $g(r)$  and frequency dependent  $Q(f)$ . Thus simple forward modeling can provide possible candidates for these functions. The excitation term  $E(f)$  depends on these, the source spectrum, and the network averaged site effect. If the source spectrum and site effects are known, then it would be possible to choose among the various candidates to describe the distance effect.

## 4.2 Modeling peak time domain values

Random Vibration Theory (RVT) is a tool to estimate peak motion in a time series given the spectral amplitudes and signal duration (Cartwright and Longuet-Higgins, 1956). Boore (1983) applied this to the seismological problem of estimating response spectra and peak velocity and acceleration from earthquakes.

The mathematical development of Cartwright and Longuet-Higgins (1956) is complicated, but Boore (1996) provides software to perform the computations. A local adaption of random vibration theory for application to this study is called *rptcal*. Following Boore (1993), the site spectrum, which is a function of distance and frequency is use to compute the 0'th, 2'nd and 4'th spectral moments. Using the signal duration, which is a function of source size to reflect the rupture duration and distance to reflect the effect of propagation, the the RMS (root mean square) motion is computed by using Parseval's theorem. The RMS value is related to the peak value of motion by the  $\eta_{max}$  value computed using the Cartwright and Longuet-Higgins (1956) definition as

$$a_{max} = \eta_{max} a_{rms}.$$

The signal duration enters into the peak motion estimation in two ways: the estimate of the RMS value and in the definition of  $\eta_{max}$ .

Because the peak value of the time domain motion requires spectral moments, the time domain results are not truly single frequency results. They are approximately if the filter function  $F(f)$  is very sharp, as were the pair of Butterworth filters used in our processing. Comparison of RVT model based predictions to observations requires that the source spectrum be appropriate for the earthquakes used. Fortunately, the shape of the source spectrum is easy to define in our frequency range for the small earthquakes that we use. Thus the modeling of peak time domain motions builds upon the  $g(r)$  and  $Q(f)$  estimated from the Fourier velocity spectra modeling and relies heavily on the duration function  $T(r)$ .



### 4.3 Propagation parameters

Both the Fourier velocity and peak filtered time domain  $D(r, f)$  regression results shown in Figures 3.4 and 3.7, respectively, are characterized by very rapid decreases of amplitude at distances less than 40 km. Such a rapid decrease can be accounted for by a geometrical spreading faster than  $r^{-1}$  at short distances. On the other hand, many authors use an  $r^{-1}$  geometrical spreading at short distances. If we did this, then a very low  $Q(f)$  would be required to fit the regression  $D(r, f)$ .

To understand the implication of the use of a very rapid geometrical spreading at short distances, we will consider two  $g(r)$  and  $Q(f)$  models. These models are first defined by fitting the Fourier velocity  $D(r)$  of Figure 3.4 and then tested again by using the *FINAL T(r)* of Table 3.7 and RVT to match the time domain  $D(r, f)$  of Figure 3.7. Table 4.1 gives the parameters of both models. Model A use conventional geometrical spreading of  $r^{-1}$  at short distances, while Model B use  $r^{-1.35}$  to fit short distances. The  $Q(f)$  values in Table 4.1 are from the peak filtered velocity data set. The Fourier velocity  $Q(f)$  results indicate  $115f^{0.75}$  for model A and  $160f^{0.65}$  for model B. We use the time domain results because we wish to model time domain data.

The effect of anelastic attenuation is reduction of amplitude with distance by a factor of  $\exp(\frac{-\pi fr}{Q(f)\beta})$ , where  $\beta = 3.5$  km/sec. The anelastic attenuation  $Q(f)$  trades off with the geometrical spreading and the cross over distance. Thus it is not unique by determined  $Q(f)$ . In addition it is closely associated with the signal bursts within the duration window and may be unrelated to  $Q(f)$  values estimated from other parts of the seismic

	Model A	Model B
$Q(f)$	$145f^{0.65}$	$180f^{0.60}$
$g(r)$	$r^{-1.0}$ $0 < r \leq 20$ $r^{-1.2}$ $20 \leq r \leq 50$ $r^{-0.6}$ $50 \leq r \leq 80$ $r^{-0.0}$ $80 \leq r \leq 250$ $r^{-0.5}$ $250 \leq r$	$r^{-1.35}$ $0 < r \leq 40$ $r^{-0.55}$ $40 \leq r \leq 80$ $r^{-0.50}$ $80 \leq r$
$\kappa_{eff}$	0.045	0.045
$\Delta\sigma$	400	400

Table 4.1: Propagation parameters of Model A and Model B

waveform.

A comparison of the difference between observed Fourier velocity  $D(r)$  and predicted Fourier velocity  $D(r)$  is given in Figure 4.1 for model A. The data set has small numbers of observation beyond 300 kilometers which is indicated by the larger standard error bars on the  $D(r)$ . Model B (Figure 4.2) has better agreement with Model A (Figure 4.1) at short distance. Band pass filtered  $D(r)$  residuals of Figure 4.3 and Figure 4.4 are similar to the Fourier velocity results. The deviations between observed and predicted  $D(r, f)$  of the distance range are within the error bars for most distances except at 135 km where an improper station instrument response may bias the regression. Since the  $D(r, f)$  is a logarithmic quantity, model B agrees with observations to within a factor of 1.4 (0.15 log units) for most distances.

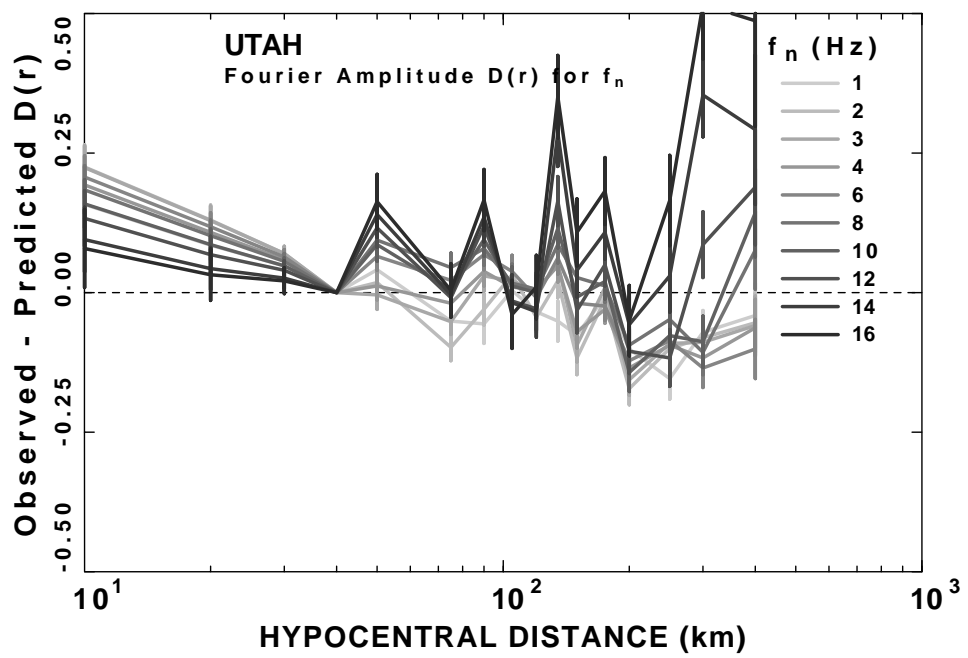


Figure 4.1: Residuals of the model fit to the Fourier velocity distance and geometrical spreading function of Model A

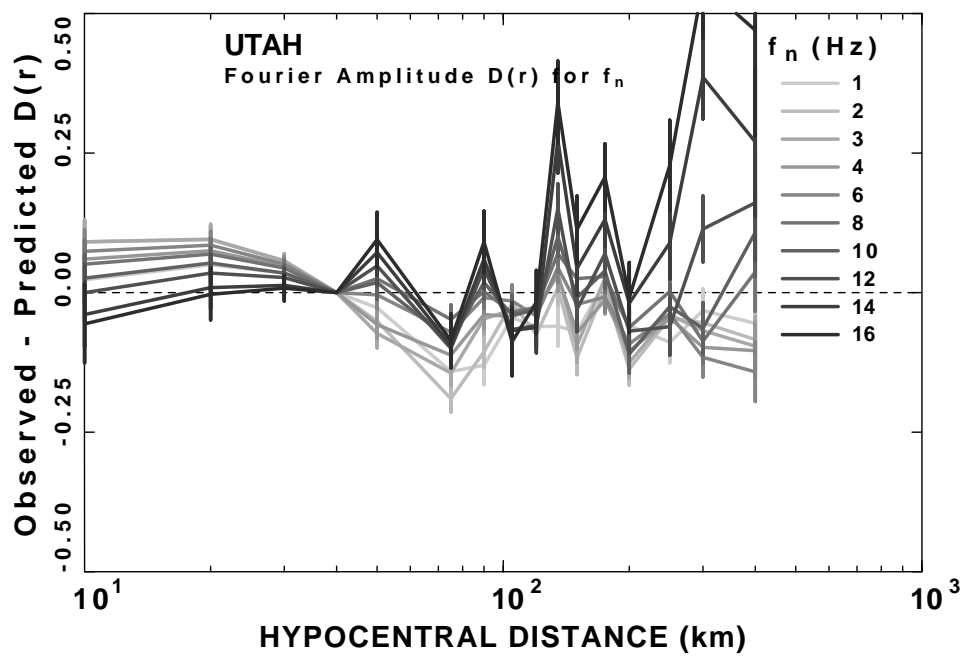


Figure 4.2: Residuals of the model fit to the Fourier velocity distance and geometrical spreading function of Model B

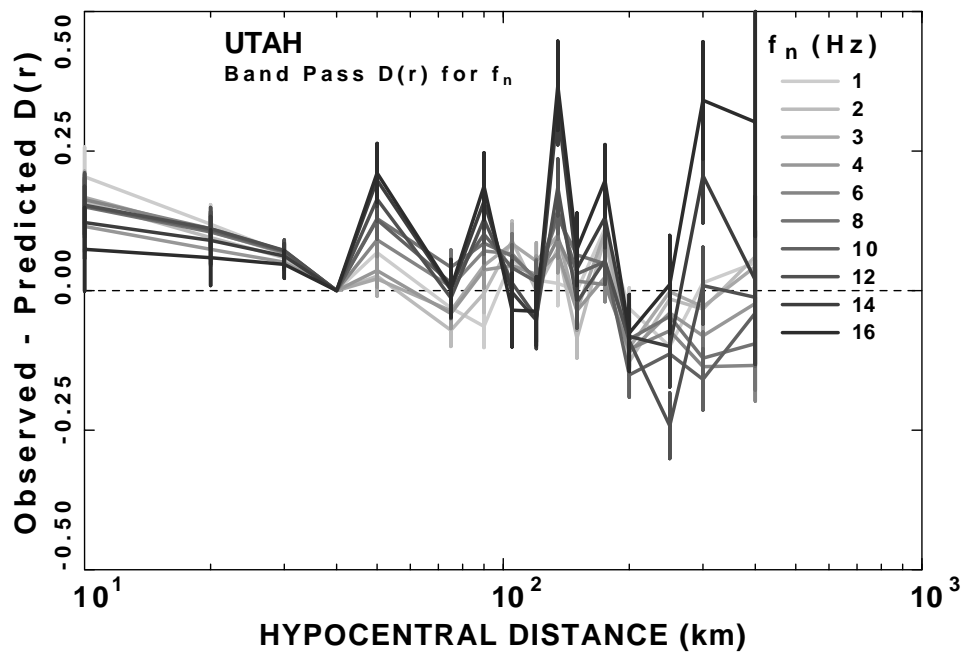


Figure 4.3: Residuals of the model fit to the band pass distance and geometrical spreading function of Model A

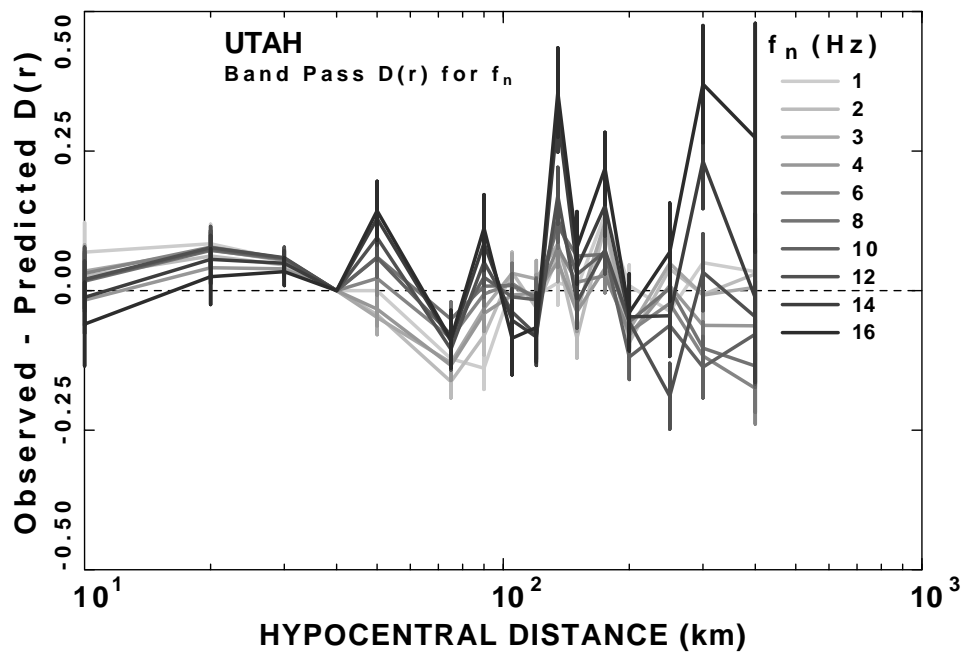


Figure 4.4: Residuals of the model fit to the band pass distance and geometrical spreading function of Model B

#### 4.4 Modeling source excitation

Although we do not have calibrated events to study source scaling, we can predict the excitation at  $r = 40$  km for a simple spectral model. The prediction of Fourier velocity spectra at a distance of  $r = 40$  km is already mentioned in section 4.1. The source excitation model for Fourier velocity spectra at  $r = 1$  km as a function of moment-magnitude,  $M_W$ ,

$$S(f, M_w) = \frac{C M_0 2\pi f}{10^{20} 1km (1 + (\frac{f}{f_c})^2)}.$$

where  $C$  is a constant given by

$$C = \frac{0.55 \cdot 2.0 \cdot 0.707}{4 \pi \rho \beta^3}.$$

Here the 0.55 represents the S-wave average radiation pattern, 2.0 is the amplification at the free surface, 0.707 is the reduction factor that accounts for the partitioning of energy into two horizontal components (Boore, 1983) and  $\rho = 2.8 \text{ g/cm}^3$  and  $\beta = 3.5 \text{ km/s}$  are the density and shear velocity we use. The corner frequency  $f_c$ , seismic moment  $M_0$  and  $1.0 = V/H$  are  $4.9 \times 10^6 \beta (\Delta\sigma/M_0)^{1/3}$ ,  $10^{1.5M_w+16.05}$ , and the ratio between vertical and horizontal components respectively. The  $10^{20}$  converts kilometers to centimeters.

Figure 1.5 shows the Fourier acceleration spectra at a distance 1 kilometer for 6 different moment magnitudes and five stress drops-10, 30, 100, 200 and 400 bars. We see that for  $M_W = 2$  and  $M_W = 3$ , there is little dependence of shape of spectrum between 1 and 16 Hz as a function of stress drop for 100, 200 and 300 bars. Since we do not know anything about the sites, we use the effective  $\kappa$ ,  $\kappa_{eff}$ , for the composite effect of network average site amplification,  $V(f)$ , and  $\kappa$  which we define as

$$e^{-\pi\kappa_{eff}f} = \overline{V(f)e^{-\pi\kappa f}}.$$

Because the excitation for small events recorded at 40 km depends only on  $Q(f)$  and the  $\kappa_{eff}$  and not on the stress drop, studying small earthquakes enables us to estimate the site effect without worrying about the unknown source spectrum scaling.

From our spectral model (Section 4.1), we conclude that the parameters controlling the shape of the excitation at 40 kilometer for small earthquakes are the  $Q(f)$ ,  $V(f)$  and  $\kappa$ . We kept  $V(f) = 1$  and varied  $\kappa_{eff}$  to fit small earthquake spectra. A  $\kappa_{eff} = 0.045$  sec, shown in the propagation parameter table (Table 4.1) was selected for use with a 400 bar stress drop. Linear frequency plots demonstrate the good fit for small earthquakes from Figure 4.7 to 4.13.

Figure 1.6 shows the excitation of Fourier velocity spectra for Model A. We found that the  $\Delta\sigma = 400$  was required to match the excitation of both small and large earthquake shapes since the shape of the excitation does not change much with source size, a factor of 1000 in low frequency excitation. The fundamental difference between propagation Models A and B is that the predicted spectral levels for the A model are higher by about  $0.6 \pm 0.1$  log units than for the B model. This is because Model B has a very rapid geometrical spreading at short distances. At this point we cannot distinguish between the models since we do not know the absolute seismic moments of any event. An indirect comparison comes from the observation that the UUSS  $M_L$ 's for  $M_L > 3$  are close to the  $M_W$ 's obtained from waveform modeling by Nabelek (<http://quakes.oce.orst.edu/moment-tensor/>),



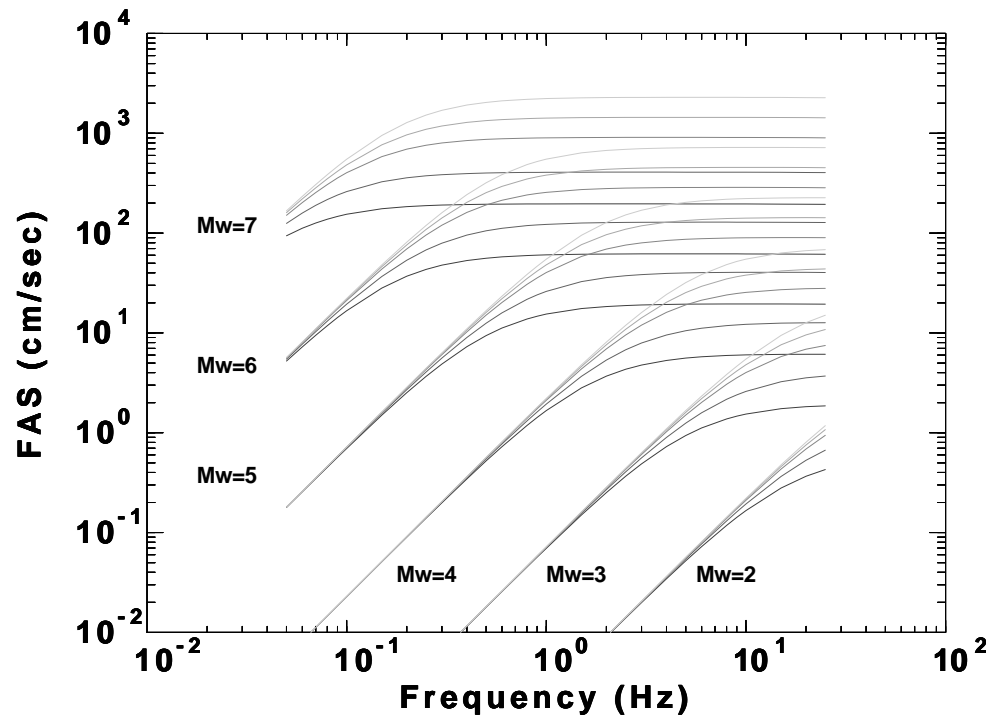


Figure 4.5: Fourier acceleration spectra at a distance 1 km as a function of  $M_W$  for stress drop 10, 30, 100, 200 and 400 bars. Dark and lightest line indicate 10 and 400 bars. The different  $M_W$  are indicated by the different low frequency asymptotics. For a given  $M_W$ , the high frequency level varies as  $\Delta\sigma$ .

and thus model B may be preferred even though its geometrical spreading at short distance is not the typical  $r^{-1}$  usually assumed by other investigators (Atkinson and Boore, 1995).

We also investigated the excitation of the mining related events. Possible explanations for the excitation of mining events are first, a higher  $\kappa = 0.09$  which reduces all high frequency because of a shallow source  $\kappa$  effect in addition to the receiver site  $\kappa$  effect. So doubling the earthquake  $\kappa$  is one way to test this. The  $\kappa$  effect is shown in Figure 4.14. The second possibility is that these are low stress drop events based on the idea that the collapse of long tunnels is a very slow process. Low stress drops imply lower corner frequencies for a given  $M_W$ . Figure 4.15 shows the predictions of the  $\Delta\sigma = 0.1$  bar source model. There is a better fit with the low stress drop event, but the seismic moments are unrealistically large.

The exact nature of the mining collapse source time functions is interesting and requires studying both the  $f > 1.0$  Hz excitation as done in this study and the  $f < 1.0$  excitation, which can be done by low frequency waveform modeling. Waveform modeling is also required for events  $> M_W 3.0$  to resolve both the absolute scaling of earthquake spectra and mining spectra.

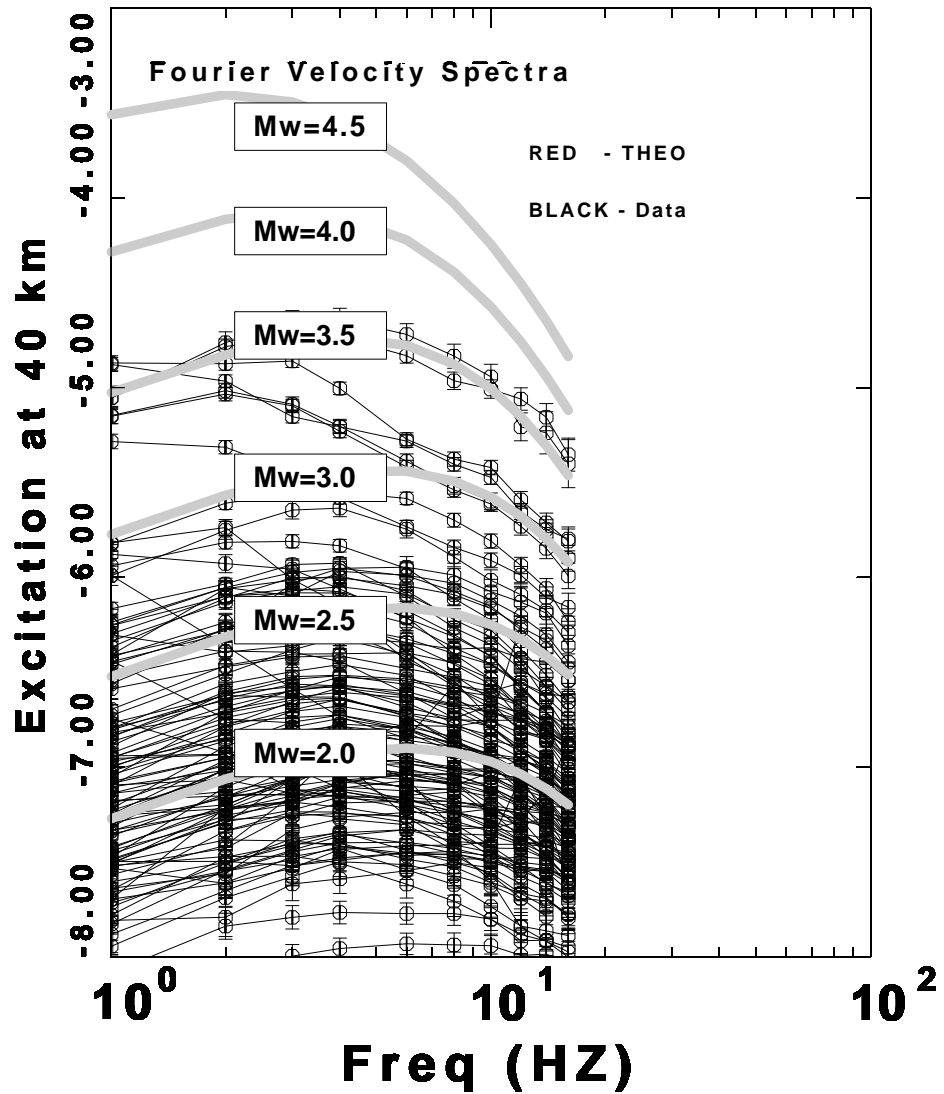


Figure 4.6: Excitation of Fourier velocity spectra at 40 km (Model A). The thick dash curve is the prediction of the 400 bar constant stress drop source model. E is the  $\log_{10}$  of the Fourier velocity spectra in  $m/sec$ .

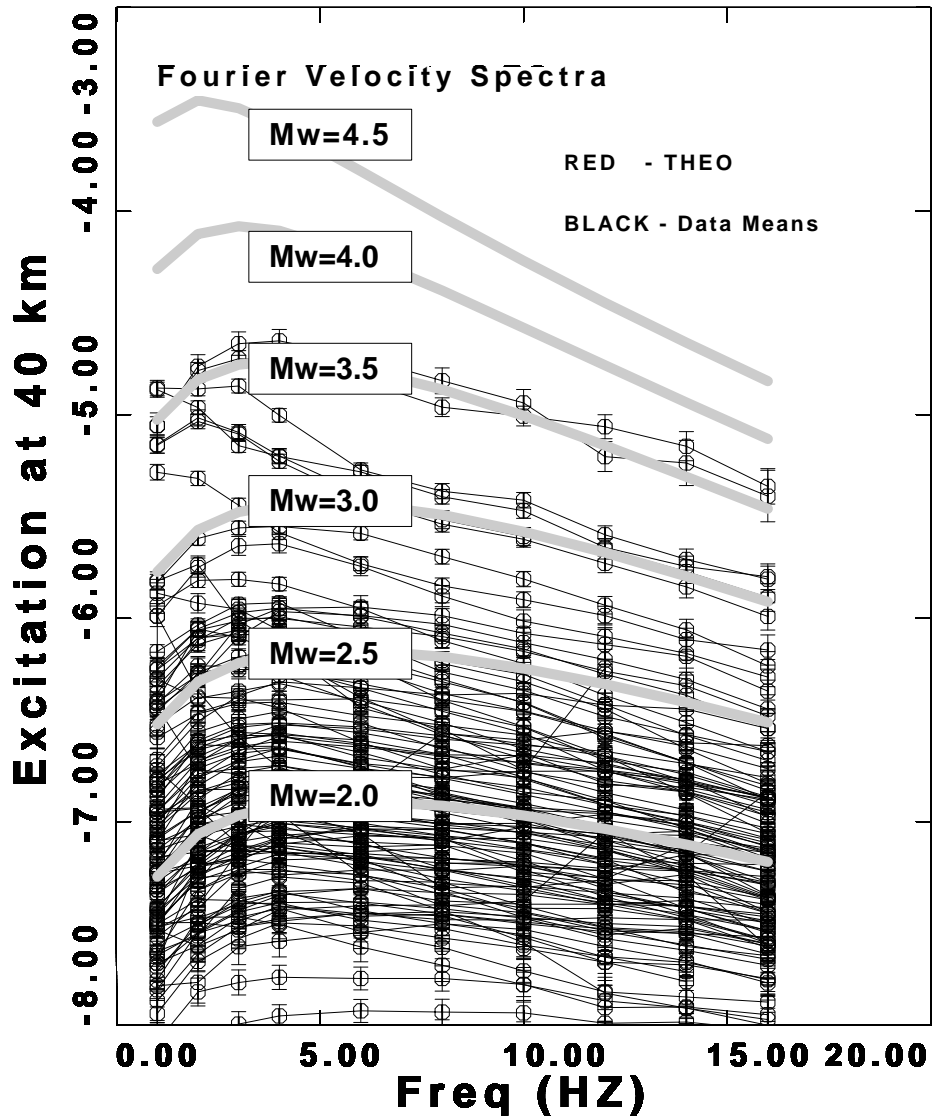


Figure 4.7: Excitation of Fourier velocity spectra at 40 km (Model A) in linear scale of frequency range. The thick dash curve is the prediction of the 400 bar constant stress drop source model. E is the  $\log_{10}$  of the Fourier velocity spectra in  $m/sec$ .

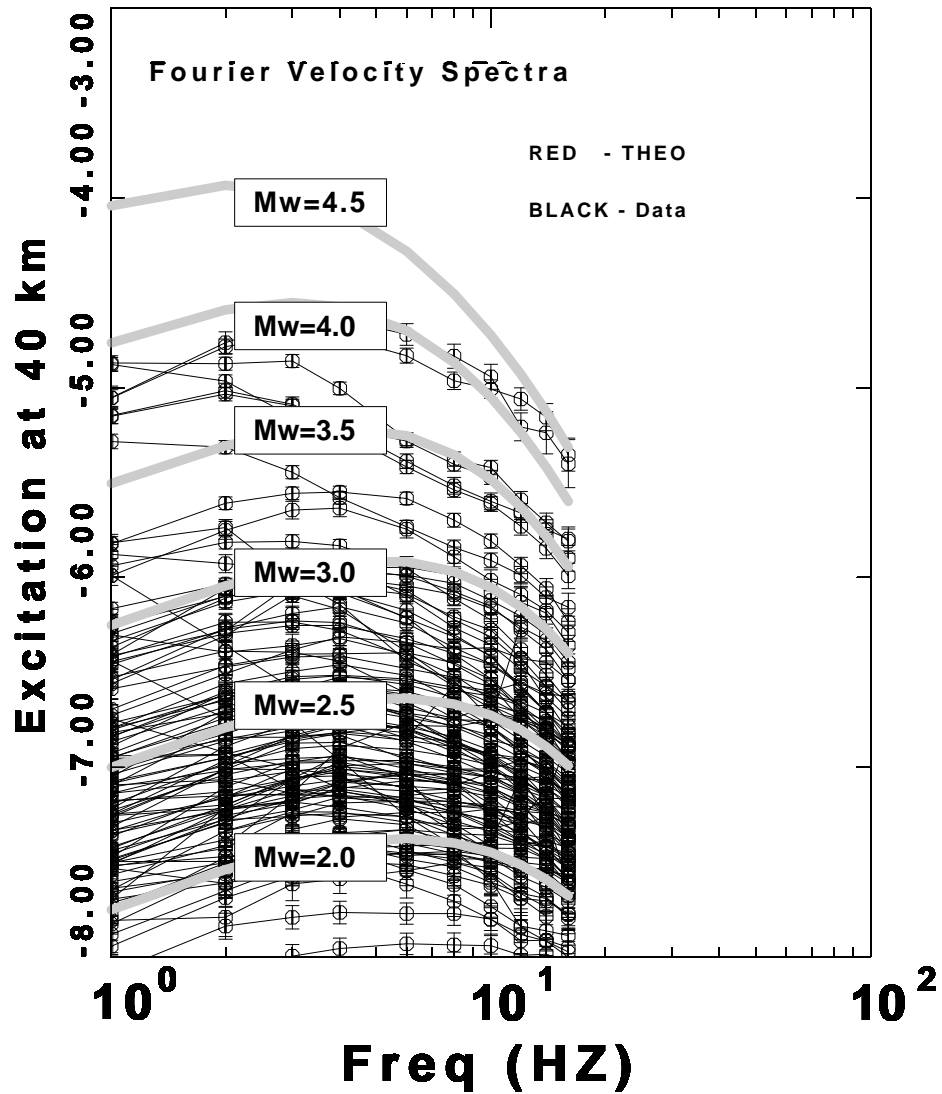


Figure 4.8: Excitation of Fourier velocity spectra at 40 km (Model B). The thick dash curve is the prediction of the 400 bar constant stress drop source model. E is the  $\log_{10}$  of the Fourier velocity spectra in  $m/sec$ .

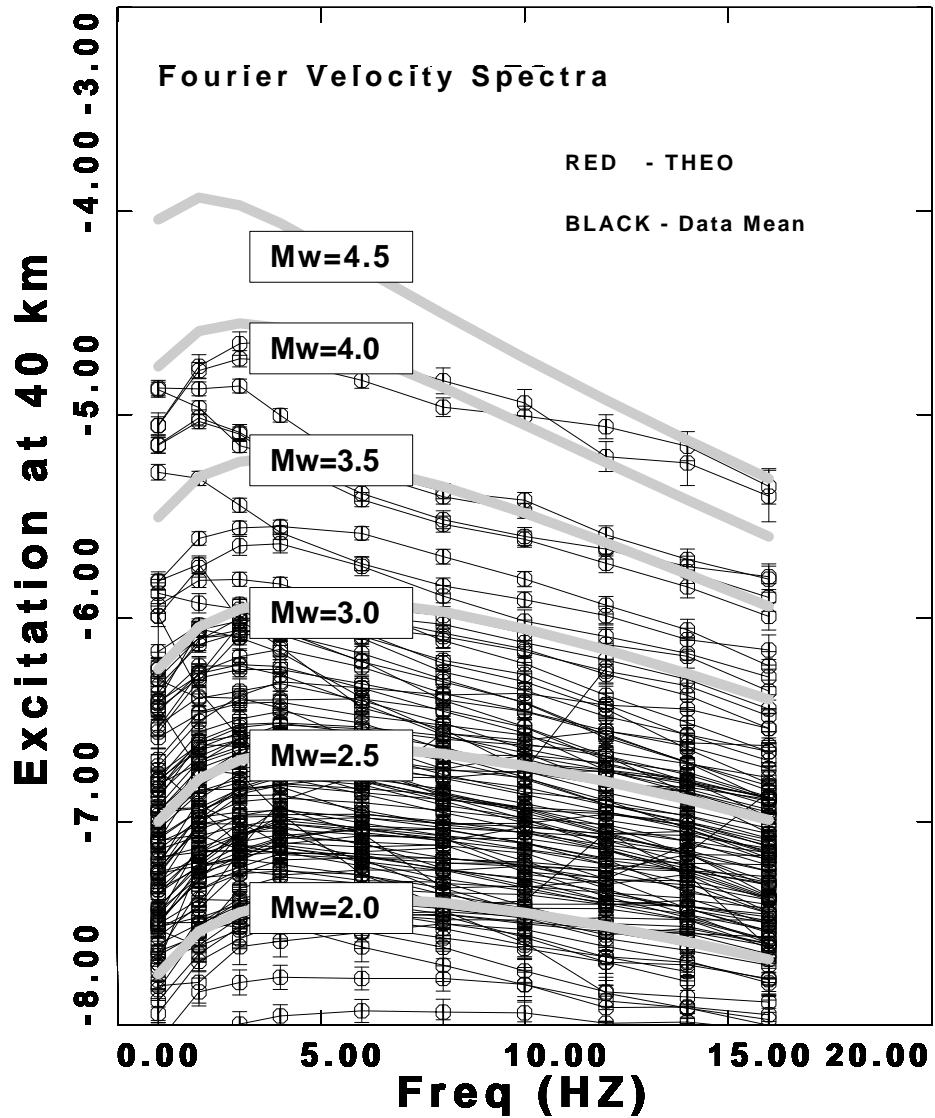


Figure 4.9: Excitation of Fourier velocity spectra at 40 km (Model B) in linear scale of frequency range. The thick dash curve is the prediction of the 400 bar constant stress drop source model. E is the  $\log_{10}$  of the Fourier velocity spectra in  $m/sec$ .

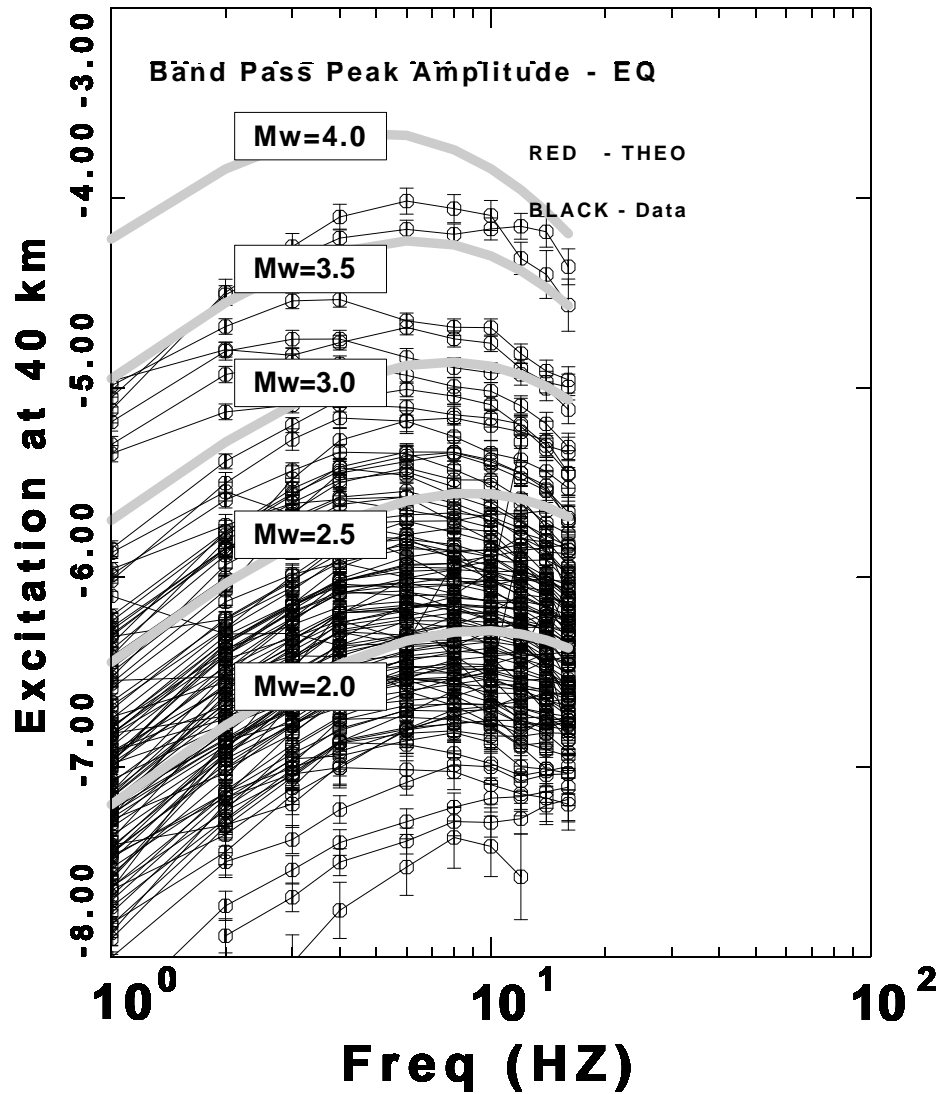


Figure 4.10: Excitation of peak filtered velocity at 40 km (Model A). The thick dash curve is the prediction of the 400 bar constant stress drop source model. E is the  $\log_{10}$  of the peak filtered velocity spectra in  $m/sec$ .

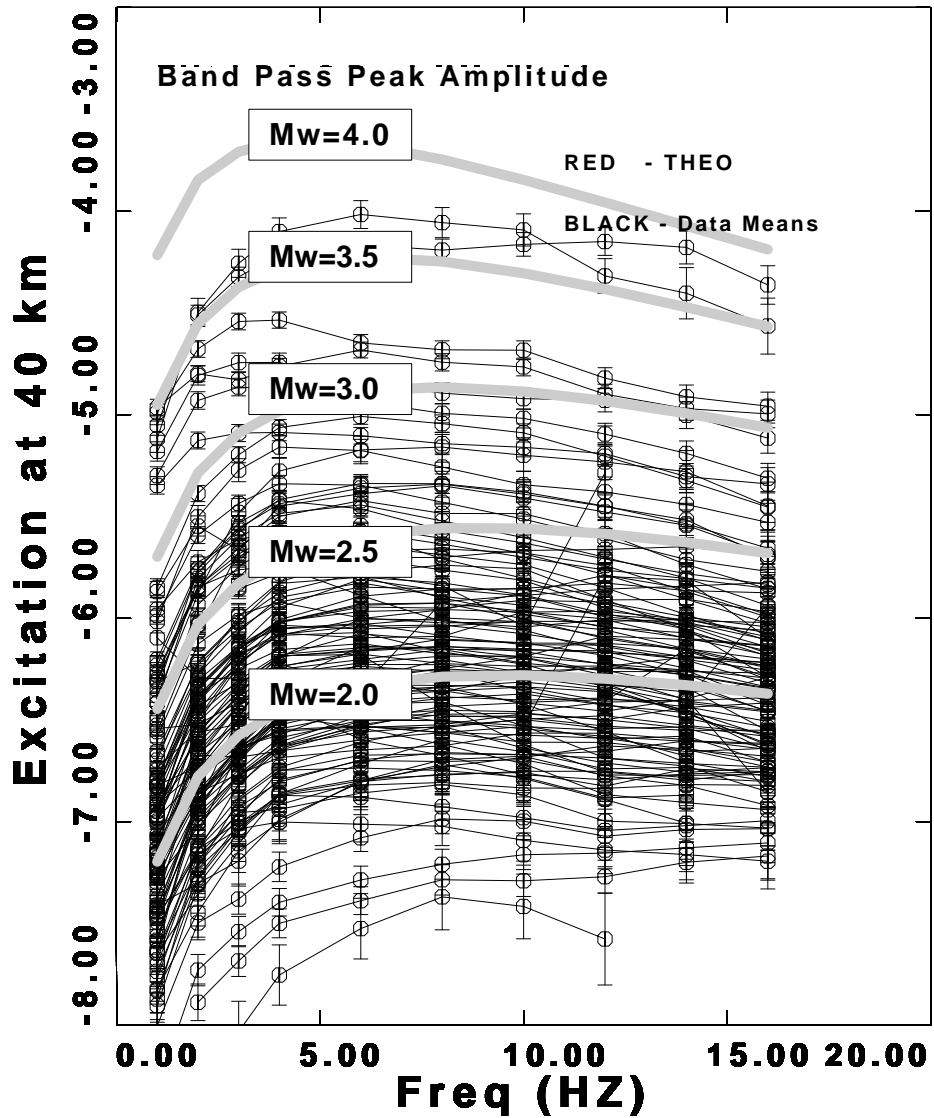


Figure 4.11: Excitation of peak filtered velocity at 40 km (Model A) in linear scale of frequency range. The thick dash curve is the prediction of the 400 bar constant stress drop source model. E is the  $\log_{10}$  of the peak filtered velocity spectra in  $m/sec$ .



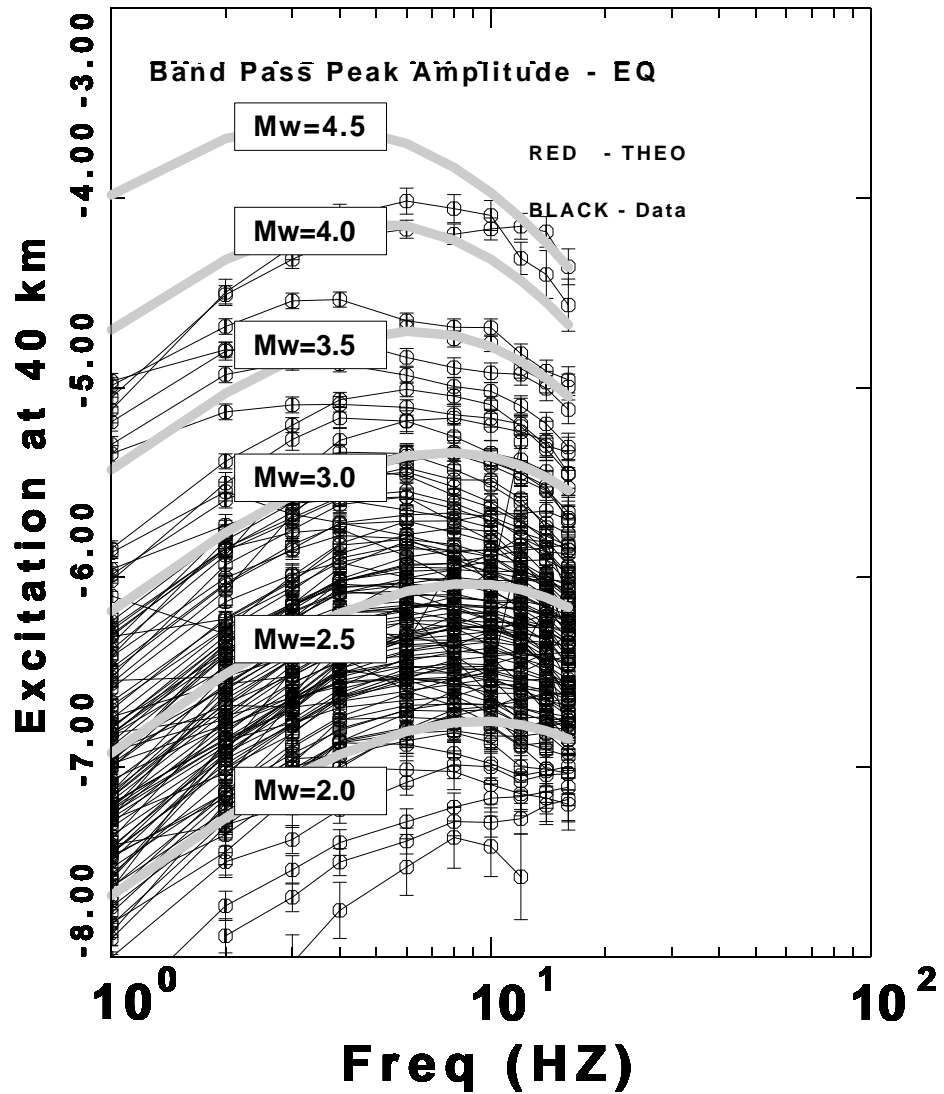


Figure 4.12: Excitation of peak filtered velocity at 40 km (Model B). The thick dash curve is the prediction of the 400 bar constant stress drop source model. E is the  $\log_{10}$  of the peak filtered velocity spectra in  $m/sec$ .

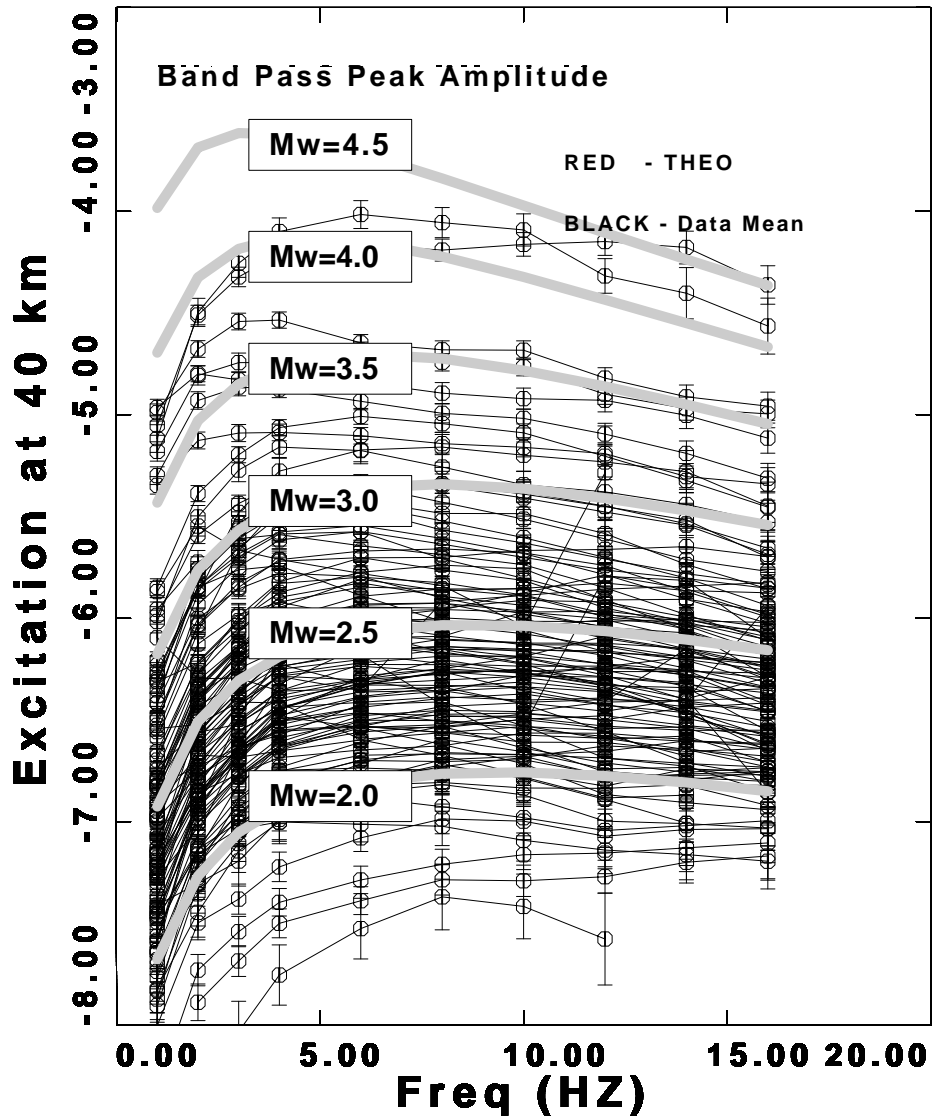


Figure 4.13: Excitation of peak filtered velocity at 40 km (Model B) in linear scale of frequency range. The thick dash curve is the prediction of the 400 bar constant stress drop source model. E is the  $\log_{10}$  of the peak filtered velocity spectra in  $m/sec$ .

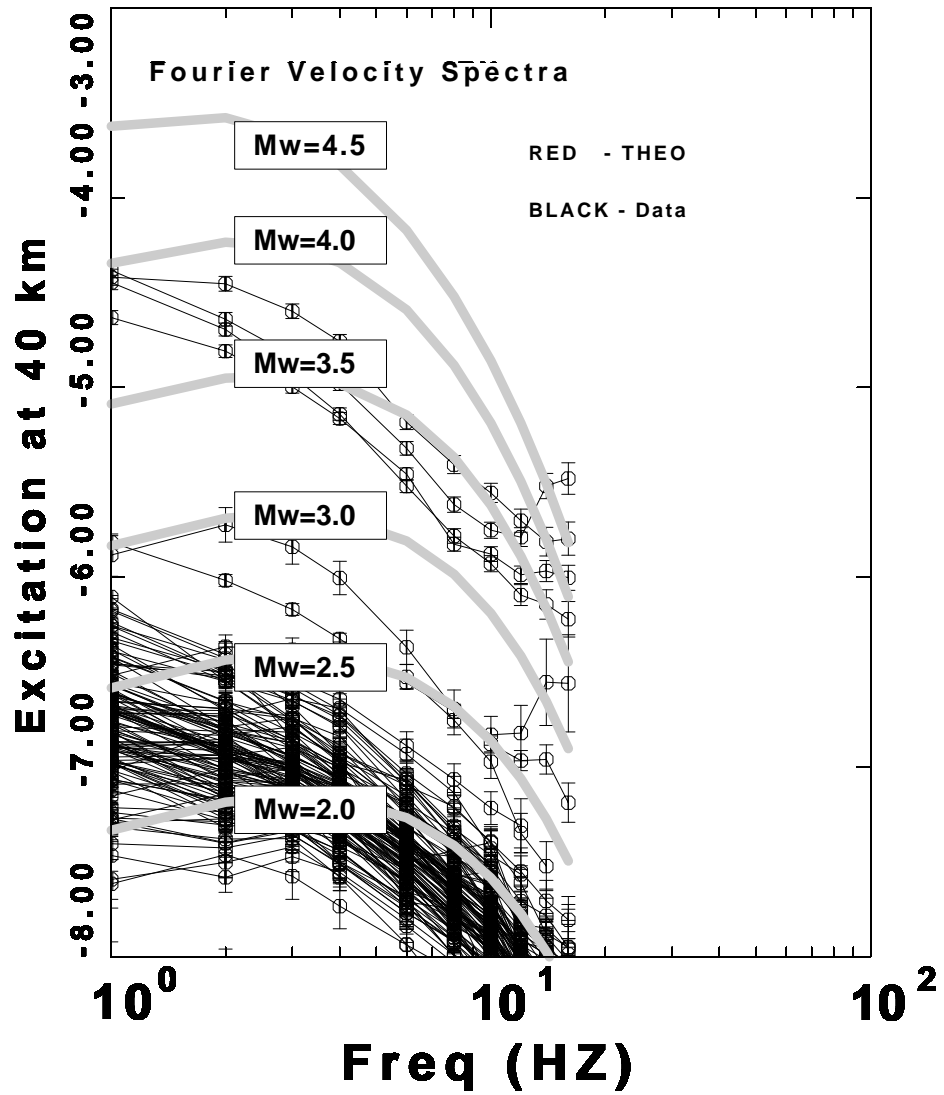


Figure 4.14: Mining related excitation of Fourier velocity spectra at 40 km. The thick curve is the prediction of the 400 bar stress drop source with  $k_{eff} = 0.09$  for propagation model A. E is the  $\log_{10}$  of the Fourier velocity spectra in  $m/sec$ .

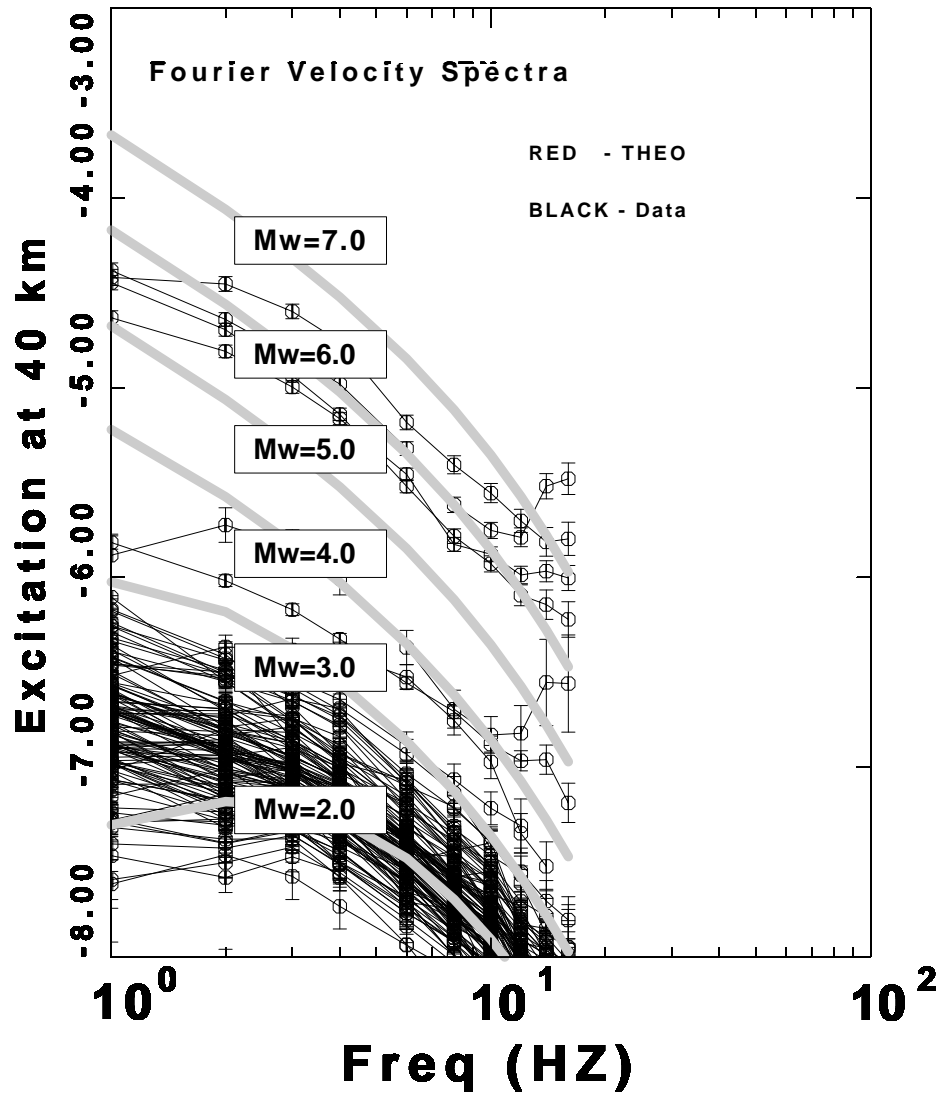


Figure 4.15: Mining related excitation of Fourier velocity spectra at 40 km. The thick curve is the prediction of the 0.1 bar constant stress drop for propagation model A. E is the  $\log_{10}$  of the Fourier velocity spectra in  $m/sec$ .

## 5. CONCLUSIONS

### 5.1 Results

We studied the regional ground motion scaling for the seismically hazardous Wasatch front, the northeastern Basin and Range province. This study analyzed a data set consisting of 3000 waveform from 110 stations and 238 regional earthquakes and mining related seismic events in the range of 10 - 500 kilometer hypocentral distance. Vertical component velocity seismograms from the University of Utah seismogram seismic network are used to measure and quantify the regional attenuation ground motion.

The vertical component distance scaling of the  $D(r)$  term of Fourier velocity spectra and band-pass filtered time domain peak motion enables us to check the appropriateness of duration length by predicting the peak filtered velocity. Comparison of the two regressions indicated that our random vibration theory (RVT) related duration term of Fourier amplitude spectra is quite good and both of regression results display consistent shape. RVT is used to obtain estimates of the peak ground motion in the time domain and duration of 5% - 75% seismic energy that follows the onset of the S-waves used throughout this study.

Our results show a geometrical spreading of

$$g(r) = \begin{cases} r^{-1.0} & r < 20 \text{ km} \\ r^{-1.2} & 20 < r < 50 \text{ km} \\ r^{-0.6} & 50 < r < 80 \text{ km} \\ r^{-0.0} & 80 < r < 250 \text{ km} \\ r^{-0.50} & r > 250 \text{ km} \end{cases}$$

and the anelastic attenuation  $Q = 145f^{0.65}$  for model A. Another set of

geometrical spreading and anelastic attenuation value is

$$g(r) = \begin{cases} r^{-1.35} & r < 40 \text{ km} \\ r^{-0.55} & 40 < r < 80 \text{ km} \\ r^{-0.50} & r > 80 \text{ km} \end{cases}$$

and  $Q = 180f^{0.6}$  for model B.

The anelastic attenuation  $Q(f)$  trades off with the geometrical spreading. A more rapid decay of amplitude with distance than expected at short distance, the low  $Q$ , and evidence of many mining related collapse events in the data set are important regression results. Our estimating of  $\kappa_0 = 0.045$  and  $\Delta\sigma = 400$  are obtained by using Boore (1983) constant stress drop model and our attenuation relationships.

The network average spectral shape for small events recorded at 40 km depends only on  $Q(f)$  and the  $\kappa_{eff}$  and not on the stress drop. If stress drop is greater than 100 bars, the limited data for larger events ( $M_L > 3$ ) indicates the need for at least a 400 stress drop. The rapid decrease of amplitude vs distance and low  $Q$  will mean that the probabilistic hazard analysis estimates for Utah will be controlled by nearby events.

Both the  $Q = 145f^{0.65}$  and  $Q = 180f^{0.6}$  are lower than that obtained in previous studies of  $Q$  in the Basin and Range province (Singh and Herrmann, 1983; Baqer and Mitchell, 1998). One reason is that coda techniques sample a larger geographic region compared to this study of S-wave amplitude.

## 5.2 Comparison of heat flow and attenuation parameters

The apparent  $Q$  at high frequencies is affected by thermal and scattering processes. Since the temperature distribution within the crust also

reflects processes that modify lithospheric structure (Powell, W. G. and Chapman, D. S., 1990), identifying thermal state of tectonic provinces and their boundaries is very important. Normally regions with recent tectonic activity commonly have higher heat flow than stable regions.

Heat is a measure of energy and the source of the energy is derived from the conduction of lithosphere and mantle convection. Another source of heat flow is frictional heat generation along a fault plane in a homogeneous medium. The rate and redistribution of frictional heat generation is not necessarily related to the heat flow anomaly.

Extension may have been an important factor in producing or maintaining the high heat flow in Basin and Range province. But elsewhere in western United States - and perhaps in the Basin and Range province - convection of heat into the crust by mantle derived melts not related to extension appears to be the primary heat source. These melts are probably related to subduction, even if the exact mechanism of their origin is unclear (Morgan and Gosnold, 1989). Low heat flow in the Sierra Nevada and northwest Pacific Coastal provinces is related to subduction. Relatively normal heat flow in the Colorado Plateau is inconsistent with the elevation of the plateau. Different tectonic environments must reflect significant differences on the propagation characterization.

The typical heat flow of the eastern Basin and Range is 90-105  $\text{mW m}^{-2}$  (Lachenbruch and Sass, 1977; Blackwell, 1978; Chapman et al., 1981). Typical value of Colorado Plateau is typically 55-60  $\text{mW m}^{-2}$  (Bodell and Chapman, 1982) and exhibits less variability than the Basin and Range region. Heat flow in the Wyoming basins is about 60  $\text{mW m}^{-2}$  (Bodell and Chapman, 1982; Chapman et al., 1984).

In anelastic or intrinsic attenuation, elastic energy is converted to heat, causing amplitude decay with travel distance in addition to geometrical spreading. It is also affected by scattering from small-scale heterogeneities in the crust. The scattering deflects and redistributes amounts of energy in the direct wave when it propagates the heterogeneous medium, distributing it into the seismic coda. The combined effect of anelastic attenuation and scattering alter its shape by reducing high frequencies more rapidly with distance than lower frequencies. Determining the mechanism of attenuation and what causes regional differences is important to understand the composition and the physical conditions of continental lithosphere (Frankel, 1991).

There have been several explanations for the differences in attenuation between tectonically active areas and stable ones. Aki (1980) suggested that the strong attenuation in tectonically active ones is caused by the presence of fractures in the crust. He proposed that the attenuation of S waves was caused by scattering from these fractures. Others (e. g. Gregersen, 1984) suggest that the strong attenuation of regional phases in certain areas may be caused by the lack of a continuous waveguide in the crust. Active tectonic regions may have a blocklike crustal structure, possibly disrupting Lg wave propagation. Another suggestion is that the differences in temperature in the crust between the various regions. A related issue is whether the attenuation in the crust is caused by anelasticity, whether elastic energy is converted into heat, or by scattering from heterogeneities in the crust. The mechanism of attenuation may vary with the tectonic region (Frankel et al., 1990).



### 5.3 Mining events

Microearthquake studies in the eastern Wasatch Plateau (Taylor, 1994) have indicated two types of seismic triggered or induced events: first, small high frequency events such as caving of the roof from the longwall mining and second, events located within a few kilometers of the mine in a lateral or vertical direction. The first type is generally smaller than the other and the most of the second types are characterized by dilatational focal mechanisms and apparent low stress drops (0.01 to 1 MPa; verified by deficiency of high frequencies). Mining related events in Colorado Plateau are related to the room-and-pillar methods (Arabasz and McCarter, 2000).

The source of our anomalous seismic events is assumed to be due to the collapse of an underground mine. This collapse leads an implosional focal mechanism in which the rock mass surrounding the seismic source suddenly moves inward and generating P waves (Wong and McGarr, 1990). The characteristics of mine seismicity are related with the local geology and type of mining operation. However, the characteristics signals are different from what would be expected for "typical" tectonic events (Taylor, 1994).

The chemical explosions (normal mining activities) events detonated in a typical work day in an industrial region, However, many of these events are ripple-fired source. Hasegawa et al. (1989) and Johnston (1988) have summarized anomalous seismicity associated with mining activities as falling into two categories: events directly associated with mining activities (type 1) and triggered (or induced) events that can occur at distances up to a few kilometers from a mine (type 2). The source of energy release

of type 1 is the rock mass at or immediately surrounding mining openings and type 2 events are occurred to movements on faults planes near mining (Pechmann et al., 1995).

#### 5.4 Final considerations

The experimental correlation of regional attenuation values with heat flow in Coast Ranges region of California and Basin and Range province is not well defined, while the values show a good correlation in some regions of United States. Central Coast Ranges of California shows lateral variation of heat flow range from 50 - 105 mW m<sup>-2</sup> (Sass et al., 1997). High attenuation and various heat flow values in Coast Ranges region is not well correlated each other. The heat flow is even less than 40 mW m<sup>-2</sup> in Sierra Nevada (Sass et al., 1981; ; Sass et al., 1997) due to a combination of thermal transients resulting from Neogene subduction and extremely low crustal radioactivity (Lacénbruch, 1968, 1970), even though it is a high attenuation ( $Q_c(f) = 139f^{(0.6)}$ ) region (Nuttli, 1986).

The Wasatch front, among the zones of transition, shows high attenuation and high heat flow values. The low crustal shear wave  $Q_\mu$  values in the upper crust have been attributed to the motion of fluids in a networks of cracks and results imply that fluids are present to 10 kilometer or more in the crust (Mitchell, 1975, 1980).

Thus we may conclude from a regional perspective that the local thermal regime of Utah is consistent with the Q pattern throughout the Wasatch front, while unexpected thermal and attenuation relation occur in the Coast Ranges of California. Further study may required to relate continental

lithosphere structure and tectonic evolution by comparing various  $Q$  values and comprehensive geophysical properties (e. g. heat flow) in United States.

The current situation in much of the United States is the low rate of earthquake activity so that neither local earthquake nor strong ground motion recordings exist sufficiently to define strong ground motion scaling relations. Sufficient numbers of strong motion data applicable to developing predictive relations exist in a few location of the western United States (e. g. California). Abundant vertical component waveforms for small earthquakes in some regions provide some constraints on the extrapolation of the California relations to the larger events for different regions. The comparative regional study result is only confined to small earthquakes until now. Since the distance dependence is now well known, the results of this study are important for seismic hazard and future studies can focus on the scaling of ground motion with earthquake size in this region.

## 7. Appendix

Figure 7.1, 7.2, 7.3, and 7.4 describe initial, and final propagation functionals, and final residuals of the regression analysis of 2.0, 4.0, 8.0, and 12 Hz ranges for Fourier velocity spectra.

Figure 7.5, 7.6, 7.7, and 7.8 describe initial, and final propagation functionals, and final residuals of the regression analysis of 2.0, 4.0, 8.0, and 12 Hz ranges for band-pass filtered spectra.

Figure 7.9, 7.10, and 7.11 show duration data and regression lines as a function of distance for frequencies of 2.0, 6.0, and 12 Hz.

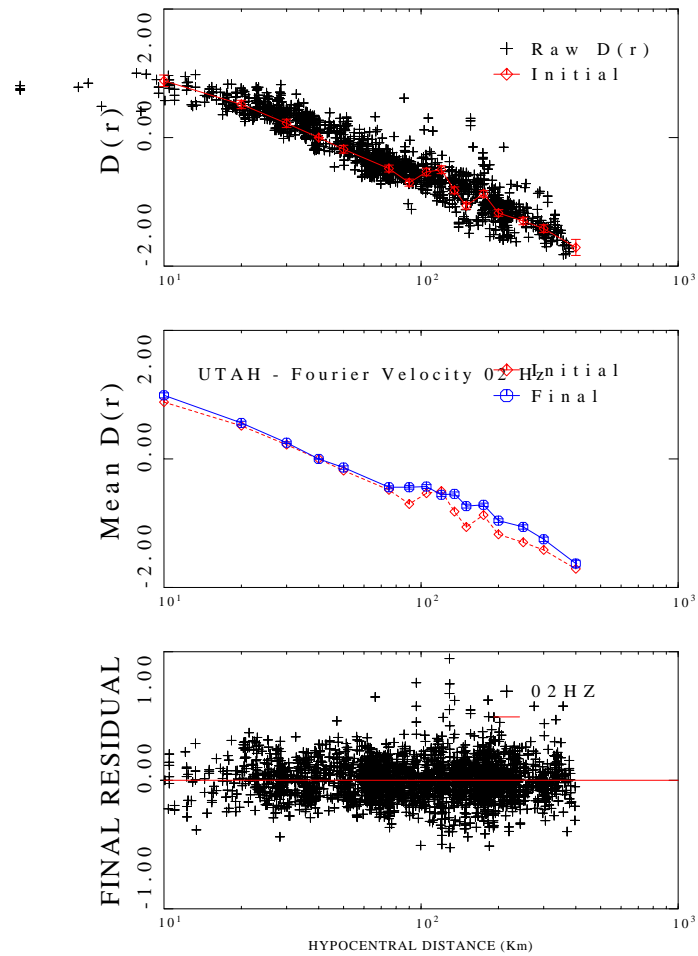


Figure 5.1: Regression analysis for 2.0 Hz. Top, initial estimate of  $D(r)$  using coda normalization technique. Middle, initial and final propagation functionals. Bottom, Final residuals of the regression analysis

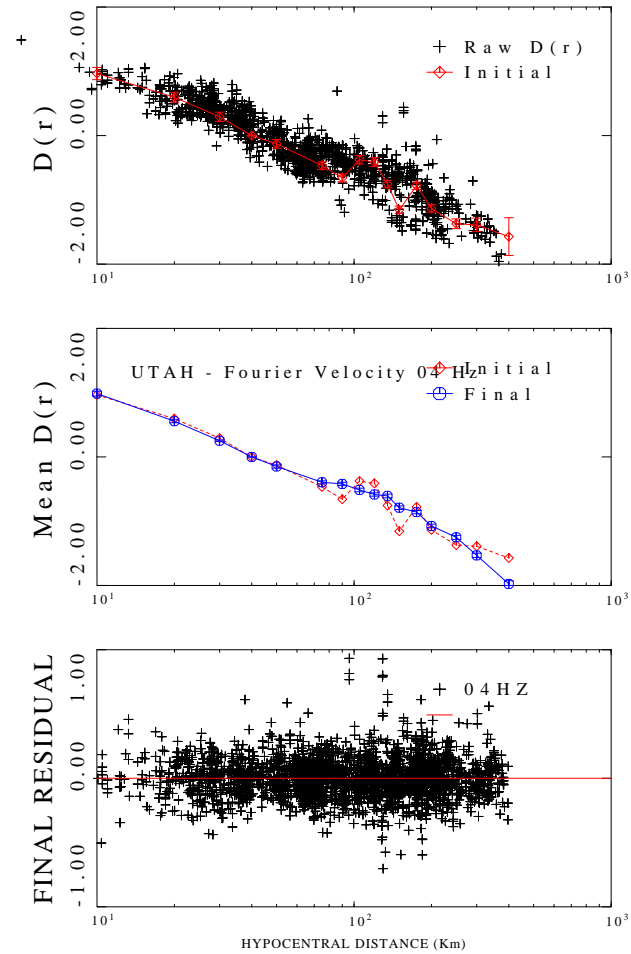


Figure 5.2: Regression analysis for 4.0 Hz. Top, initial estimate of  $D(r)$  using coda normalization technique. Middle, initial and final propagation functionals. Bottom, Final residuals of the regression analysis

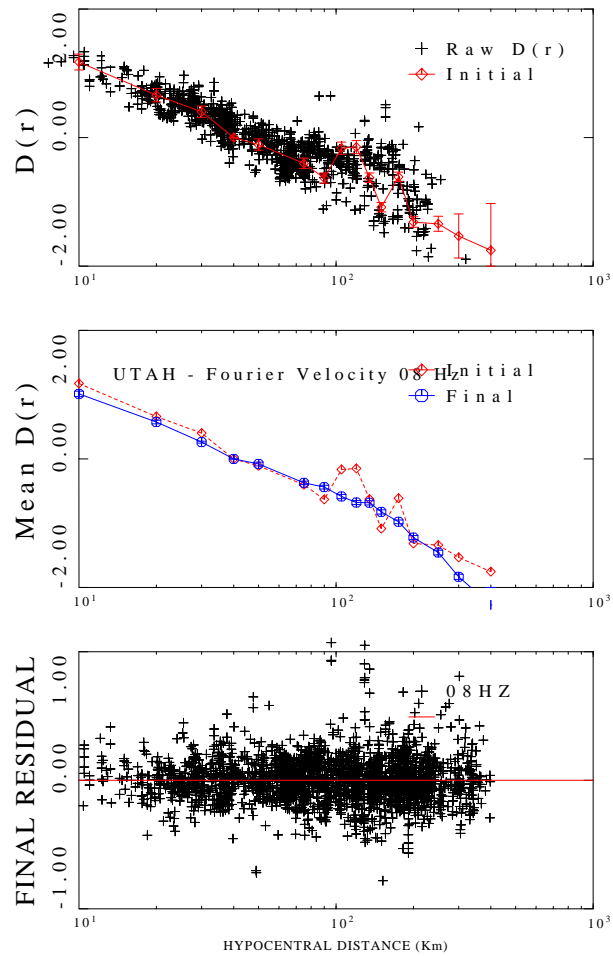


Figure 5.3: Regression analysis for 8.0 Hz. Top, initial estimate of  $D(r)$  using coda normalization technique. Middle, initial and final propagation functionals. Bottom, Final residuals of the regression analysis

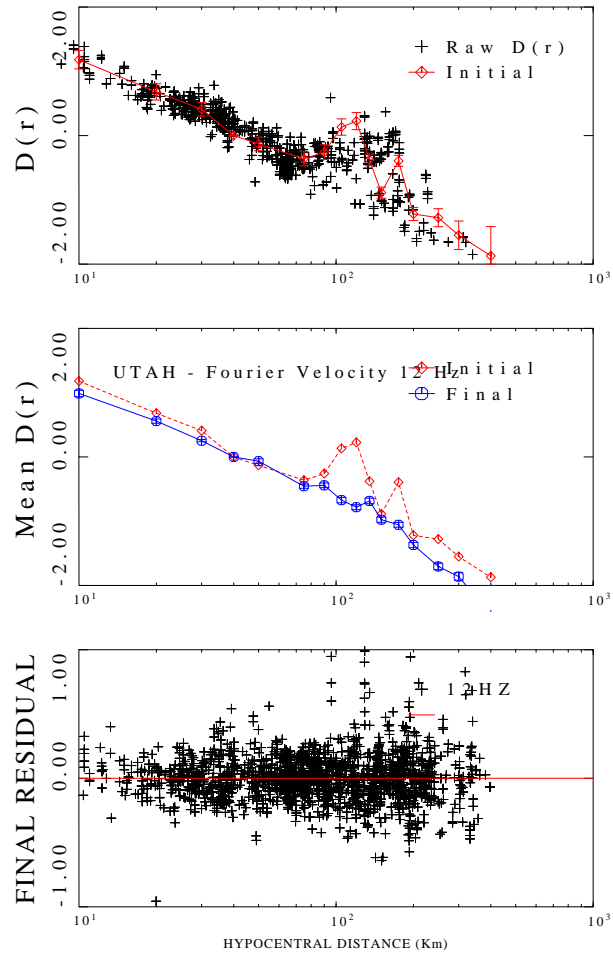


Figure 5.4: Regression analysis for 12 Hz. Top, initial estimate of  $D(r)$  using coda normalization technique. Middle, initial and final propagation functionals. Bottom, Final residuals of the regression analysis



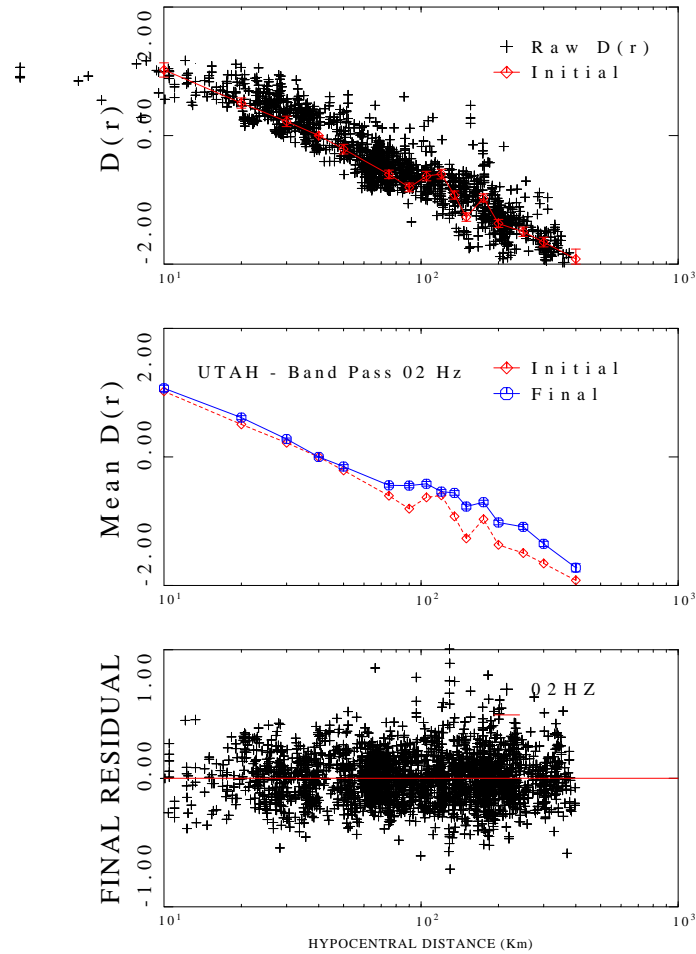


Figure 5.5: Regression analysis for 2.0 Hz. Top, initial estimate of  $D(r)$  using coda normalization technique. Middle, initial and final propagation functionals. Bottom, Final residuals of the regression analysis

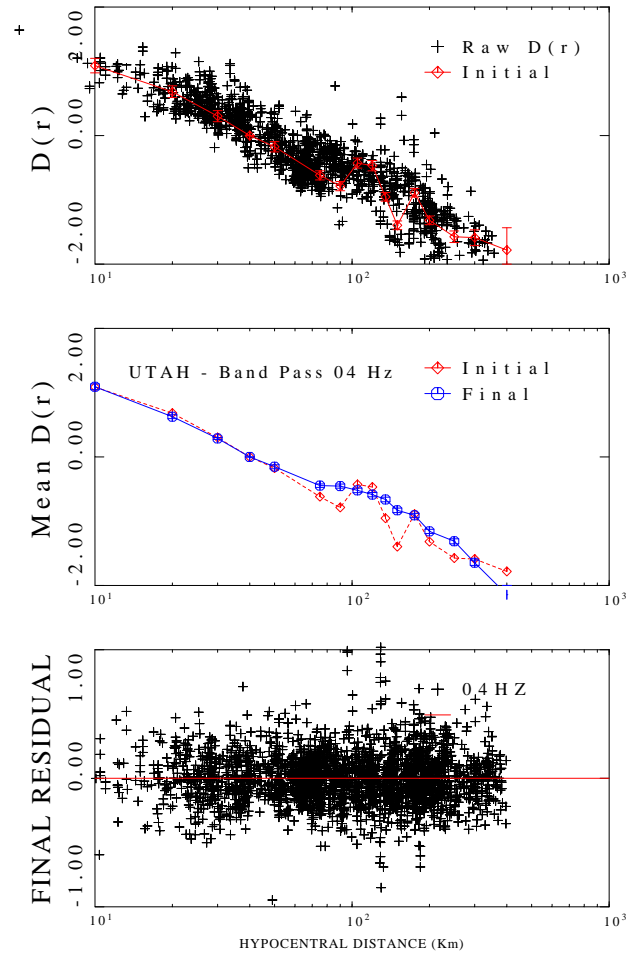


Figure 5.6: Regression analysis for 4.0 Hz. Top, initial estimate of  $D(r)$  using coda normalization technique. Middle, initial and final propagation functionals. Bottom, Final residuals of the regression analysis

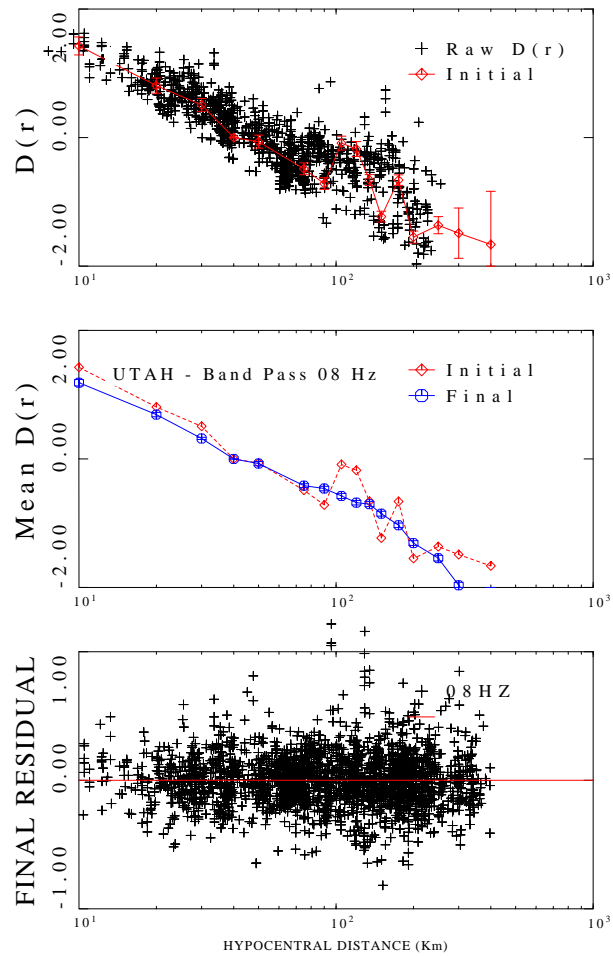


Figure 5.7: Regression analysis for 8.0 Hz. Top, initial estimate of  $D(r)$  using coda normalization technique. Middle, initial and final propagation functionals. Bottom, Final residuals of the regression analysis

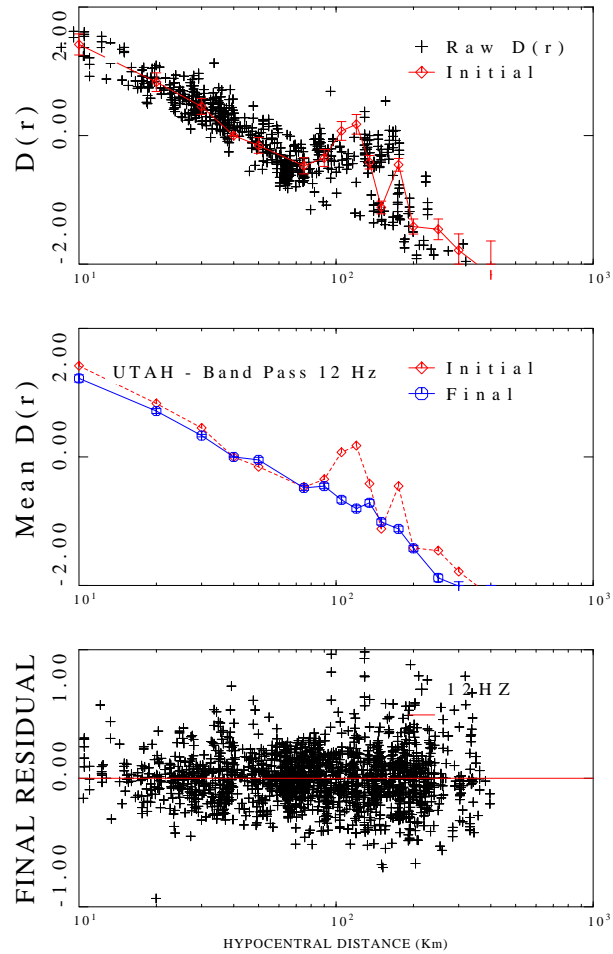


Figure 5.8: Regression analysis for 12 Hz. Top, initial estimate of  $D(r)$  using coda normalization technique. Middle, initial and final propagation functionals. Bottom, Final residuals of the regression analysis

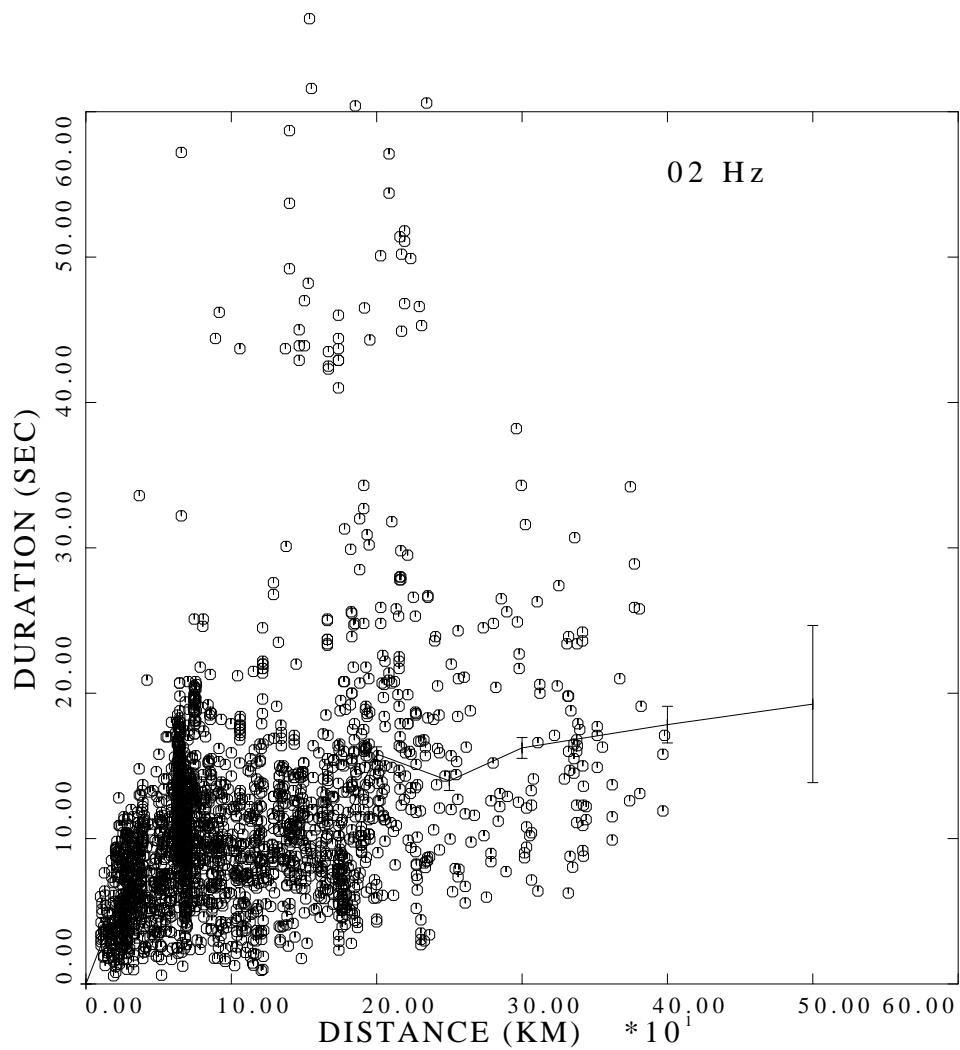


Figure 5.9: Duration data and regression lines as a function of distance for filtered frequency of 2.0 Hz

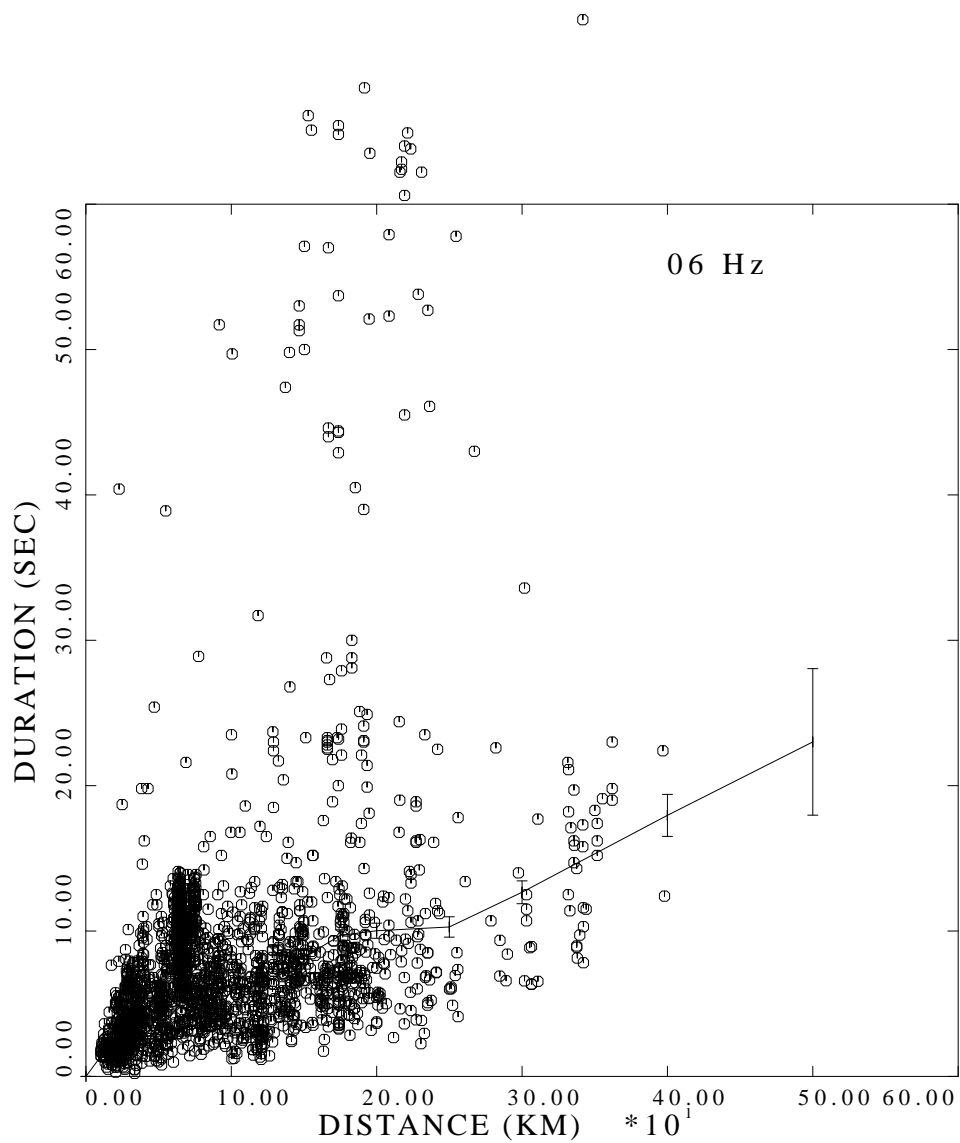


Figure 5.10: Duration data and regression lines as a function of distance for filtered frequency of 6.0 Hz

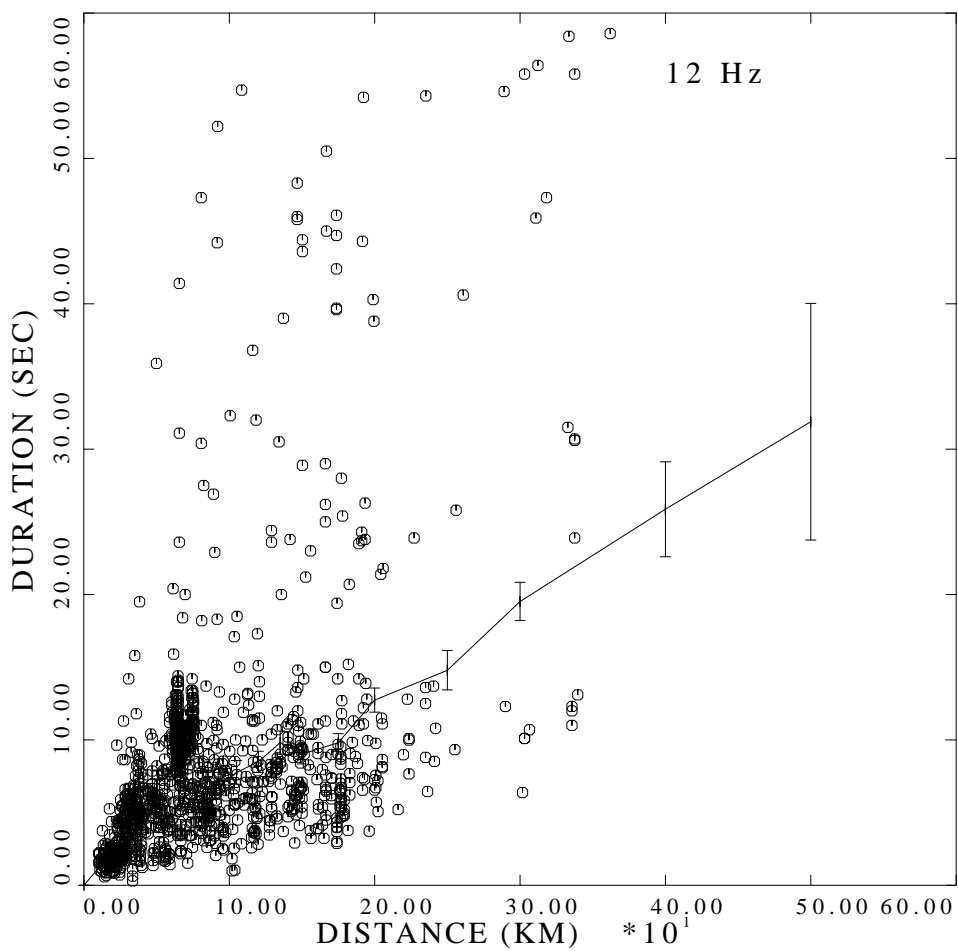


Figure 5.11: Duration data and regression lines as a function of distance for filtered frequency of 12 Hz

## Bibliography

- Aki, K., 1980. Scattering and attenuation of shear waves in the lithosphere, *J. Geophys. Res.*, 85, 6496-6504.
- Algermissen, S.T. and D. M. Perkins, 1976. A probabilistic estimate of maximum acceleration in rock in the contiguous United States, *U.S. Geol. Surv., Open-File Rept.* 76-416, 45pp.
- Anderson, J. G., and Y. Lei (1994). Nonparametric description of peak acceleration as a function of magnitude, distance, and site in Guerrero, Mexico, *Bull. Seis. Soc. Am.* 84, 1003-1017.
- Arabasz, W. J., and M. K. McCarter (2000). Mine seismicity and the interface between mining engineers and seismologists (abstract), *Seism. Res. Lett.*, 71 (2), 220.
- Arabasz, W. J., Smith, R. B. and Richins, W. D., 1980. Earthquake studies along the Wasatch front, Utah: Network monitoring, seismicity, and seismic hazards, *Bull. Seis. Soc. Am.*, 70. 1479-1499.
- Atkinson, G. M. (1993). Earthquake source spectra and attenuation in southeastern Canada, *University of Western Ontario, London, Ontario*, Ph.D. thesis.
- Atkinson, G. M., and D. M. Boore (1995). Ground-motion relations for eastern North America, *Bull. Seis. Soc. Am.* 85, 17-30.
- Atwater, T., 1970. Implications of plate tectonics for the Cenozoic tectonic evolution of western North America. *Geol. Soc. Am. Bull.*, 81: 3513-3536.
- Baquer, S., and Mitchell, B. J., 1998. Regional variation of Lg coda Q in the continental United States and its relation to crustal structure and evolution, *Pure appl. geophys.*, 153, 613-638.
- Blackwell, D. D., 1978. Heat flow and energy loss in the western United States. In: R. B. Smith and G. P. Eaton (Editors). *Cenozoic Tectonics and Regional Geophysics of the Western Cordillera. Geol. Soc. Am. Mem.*, 152: 175-208.
- Best, M. G., and Brimhall, W. H., 1974. Late Cenozoic alkalic basaltic magmas in the western Colorado plateaus and the Basin and Range transition zone, U.S.A., and their bearing on mantle dynamics: *Geol. Soc. Am. Bul.*, 85, 1677-1690.



- Boatwright, J. (1982). A dynamic model for far-field acceleration, *Bull. Seis. Soc. Am.* 72, 1049-1068.
- Bodell, J. M. and Chapman, D. S., 1982. Heat flow in the north-central Colorado Plateau. *J. Geophys. Res.*, 87, 2869-2884.
- Boore, D. M. (1983). Stochastic simulation of high-frequency ground motion based on seismological models of the radiated spectra, *Bull. Seis. Soc. Am.*, 73, 1865-1894.
- Boore, D. M. and Atkinson, G. M. (1987). Stochastic prediction of ground motion and spectral response parameters at hard-rock sites in Eastern North America, *Bull. Seis. Soc. Am.*, 77, 440-467.
- Boore, D. M. (1996). SMSIM — Fortran Programs for Simulating Ground Motions from Earthquakes: Version 1.0, *U.S. Geological Survey Open-File Report 96-80-A*, 73 pp
- Bouchon, M. (1978). A dynamic source model for the San Fernando earthquake, *Bull. Seis. Soc. Am.* 68, 1555-1576.
- Bucher, R. L. and Smith R.B., 1971. Crustal structure of the eastern Basin and Range province and the northern Colorado Plateau from phase velocities of Rayleigh waves in *The Structure and Physical Properties of the Earth's Crust*, *Am. Geophys. Union Monograph 14*, John G. Heacock, Editor, 59-70.
- Cartwright, D. E. and M. S. Longuet-Higgins (1956). The statistical distribution of the maxima of a random function, *Proc. Roy. Soc. London*, Ser. A237, 212-223.
- Castro, R. R., J. G. Anderson, and S. K. Singh (1990). Site response, attenuation, and source spectra of S waves along the Guerrero, Mexico subduction zone, *Bull. Seis. Soc. Am.*, 80, 1481-1503.
- Chapman, D. S., Clement, M. D. and Mase, C. W., 1981. Thermal regime of the Escalante Desert, Utah, with an analyses of the Newcastle geothermal system, *J. Geophys. Res.*, 86, 11735-11746.
- Chapman, D. S., Keho, T. H., Bauer, M.S and Picard, M.D., 1984. Heat flow in the Unita Basin determined from bottom hole temperature (BHT) data, *Geophysics*. 49, 453-466.
- Chavez, D. E. & Priestley, K. F., 1986. Measurement of frequency dependent Lg attenuation in the Great Basin, *Geophys. Res. Lett.*, 13, 551-554.

- Cluff, L. S., L. F. Hintze, G. E. Brogan, and C. E. Glass, 1975. Recent activity of the Wasatch fault, northwestern Utah, U. S. A., *Tectonophysics*, 29, 161-168.
- Cultrera, G., Boore, D. M., Joyner, W. B., and Dietel, C. M., 1999. Non-linear soil response vicinity of the Van Norman complex following the 1994 Northridge, California, Earthquake, *Bull. Seis. Soc. Am.*, 89, 1214-1231.
- Eaton, G. P., 1982. The Basin and Range Province: Origin and tectonic significance. *Annu. Rev. Earth Planet. Sci.*, 10: 409-440.
- Frankel, A. (1982). Source parameters and scaling relationships of small earthquakes in the northern Caribbean, *Bull. Seis. Soc. Am.*, 72, 1173-1190.
- Frankel, A. (1991). Mechanisms of seismic attenuation in the crust: Scattering and anelasticity in New York state, South Africa, and Southern California, *J. Geophys. Res.*, 96, 6269-6289.
- Frankel, A., McGarr, A., Bicknell, J., Mori, J., Seeber, L., and Cranswick, E., 1990. Attenuation of high-frequency shear waves in the crust: Measurements from New York state, South Africa, and Southern California, *J. Geophys. Res.*, 95, 17441-17457.
- Gans P. B., Mahood G. A. and Schermer E., 1989. Synextensional Magmatism in the Basin and Range province, *Geological Society of America, Special Paper*, 233, 1989.
- Gregerson, S., 1984. Lg-wave propagation and crustal structure differences near Denmark and the North Sea, *Geophys. J. R. Astro. Soc.*, 79, 217-234.
- Guidebook to the geology of Utah, Utah Geological Society No 18, 1964.
- Guidebook to the geology of Utah, Park City district Utah. No 22, 1968.
- Harmsen, S. (1997). Estimating the diminution of shear-wave amplitude with distance: application to the Los Angeles, California, urban area, *Bull. Seis. Soc. Am.* 87, 888-903.
- Hasegawa, H. S., R. J. Wetmiller, and D. J. Gendzwill (1989). Induced seismicity in mines in Canada-An overview, *Pageoph*, 129, 423-453.
- Herrmann, R. B. (2000). Comparative ground motion studies, USGS Award Number: 1434-HQ-97-GR03090.

- Herrmann, R. B., 1985. An extension of Random Vibration Theory estimates of strong ground motion to large earthquakes, *Bull. Seis. Soc. Am.*, 75, 1447-1453.
- Hose, R. K., and Blake, M.c., Jr., 1976. Geological and mineral resources of White Pine Country, Nevada; Part 1, Geology: *Nevada Bureau of Mines and Geology Bulletin*, 85, p. 1-35.
- <http://www-ep.es.llnl.gov/typ/sac.html>.
- <http://quakes.oce.orst.edu/moment-tensor/>.
- Idriss, I.M. (1985). "Evaluating seismic risk in engineering practice," *Proceedings of the 11th International Conference on Soil Mechanics and Foundation Engineering*, San Francisco, 1, 255-320.
- Johnston, J. C. (1988). A survey of mining associated rockbursts, *M. S. Thesis*, Massachusetts Institute of Technology, Cambridge, Massachusetts.
- Joyner, W. B. and D. M. Boore (1980). A stochastic source model for synthetic strong motion seismograms, *Proc. of 7th World Conf. on Earthquake Eng.*, 1-8.
- Kramer, S.(1996). *Geotechnical earthquake engineering*, Prentice Hall, Upper Saddle River, NJ, 07458, 653.
- Lachenbruch, A. H., Preliminary geothermal model of the Sierra Nevada, *J. Geophys. Res.*, 73, 6977-6989, 1968.
- Lachenbruch, A. H., Crustal temperature and heat production: Implications of the linear heat flow relation, *J. Geophys. Res.*, 75, 3291-3300, 1970.
- Lachenbruch, A. H. and Sass, J. H., 1977. Heat flow in the United States and the thermal regime of the crust. In: J. G. Heacock (Editor), *The Earth's Crust. Am. Geophys. Union, Geophys. Monogr.*, 20: 626-675.
- Lachenbruch, A. H. and Sass, J. H., 1978. Models of an extending lithosphere and heat flow in the Basin and Range province, *Geol. Soc. Am. Mem.*, 152, 209-250.
- Malagnini, L. (1999). Ground motion scaling in Italy and Germany, *Ph. D. Dissertation*, Saint Louis University.
- Mayeda, K., S. Koyanagi, M. Hoshiaba, K. Aki, and Y. Zeng (1992). A comparative study of scattering, intrinsic and coda  $Q^{-1}$  for Hawaii, Long Valley, and central California between 1.5 and 15.0 Hz, *J. Geophys. Res.*, 97, 6643-6660.

- Mitchell, B. J., 1975. Regional Rayleigh wave attenuation in North America, *J. geophy. Res.*, 85, 5212-5218.
- Mitchell, B. J., 1980. Frequency dependence of shear wave internal friction in the continental crust of eastern North America, *Geophys. J. Int.*, 85, 5212-5218.
- Mitchell, B. J. and Xie, J.K., 1994. Attenuation of multiphase waves in the Basin and Range Province-3. Inversion for crustal anelasticity, *Geophys. J. Int.*, 116, 468-484.
- Morgan, P., and Gosnold, W. D., 1989. Heat flow and thermal regimes in the continental United States, *Geological Society of America, Memoir 172*, 1989.
- Nuttli, O. W., 1986. Yield estimates of Nevada test site explosions obtained from seismic Lg waves, *J. Geophy. Res.*, 91, 2137-2152.
- Ou, G. B. and R. B. Herrmann (1990). A statistical model for ground motion produced by earthquakes at local and regional distances, *Bull. Seis. Soc. Am.*, 80, 1397-1417.
- Pechmann, J. C., Walter, W. R., Nava, S. J., and Arabasz, W. J. (1995). The February 3, 1995,  $M_L$  5.1 seismic event in the Trona mining district of southwestern Wyoming, *Seis. Re. Lett.* 66, No. 3.
- Peseckis, L. L. & Pomeroy, P. W., 1984. Determination of Q using Lg waves and its implications for nuclear yield estimation, *EOS, Trans. Am. geophys. Un.*, 65, 995.
- Phillips, W. S. and K. Aki (1986). Site amplification of coda waves from local earthquakes in central California, *Bull. Seis. Soc. Am.*, 76, 627-648.
- Powell, W. G. and Chapman, D. S., 1990. A detailed study of heat flow at the Fifth Water Site, Utah, in the Basin and Range-Colorado Plateau transition, *Tectonophysics*, 176: 291-314.
- Priestley, K and Brune, J., 1978. Surface waves and structure of the Great Basin of Nevada and western Utah, *J. Geophy. Res.*, 83, 2265-2273.
- Raooof, M., R. B. Herrmann, and L. Malagnini (1999). Attenuation and excitation of three component ground motion in Southern California, *Bull. Seis. Soc. Am.*, 89, 888-902.
- Reiter, M., Mansure, A. J. and Shearer, C., 1979. Geothermal characteristics of the Colorado Plateau. *Tectonophysics*, 61: 183-195.

- Rogers, A. M., Harmsen, S. C., Herrmann, R. B. & Meremonte, M. E., 1987. A study of ground motion attenuation in the southern Great Basin, Nevada-California, using several techniques for estimates of  $Q_s$ ,  $\log A_0$ , and coda  $Q$ , *J. Geophys. Res.*, 92, 3527-3540.
- Samieyade-Yard, M., 1993. Ground motion studies in the southern Great Basin of Nevada and California, *Ph. D. Dissertation*, Saint Louis University.
- Sanchez-Sesma, F. and Campillo, M. (1993). "Topographic effects for incident P, SV, and Rayleigh waves," *Tectonophysics*, 218, No. 1-3, 113-125.
- Sass, J. H., D. D. Blackwell, D. S. Chapman, J. K. Costain, E. R. Decker, L. A. Lawver, and C. A. Swanberg, 1981. Heat flow from the crust of the United States, in *Physical Properties of Rocks and Minerals*, edited by Y. S. Touloukian, W. R. Judd, and R. F. Roy, pp. 503-548, McGraw-Hill, New York.
- Sass, J. H., C. F. Williams, Arthur H. Lachenbruch, S. P. Galanis Jr., F. V. Grubb, 1997. Thermal regime of the San Andreas fault near Parkfield, California, *J. Geophys. Res.*, 102, 27575-27585.
- Singh, S. and R. B. Herrmann, 1983. Regionalization of crustal Q in the continental United States, *J. Geophys. Res.*, 88, 527-538.
- Slemmons, D. B. and Mckkinney, R. (1977). "Definition of 'active fault'", *Miscellaneous Paper S-77-8*, U.S. Army Corps of Engineers Waterways Experiment Station, Vicksburg, Mississippi.
- Smith, R. B., 1974. Seismicity and earthquake hazards of the Wasatch front, Utah, July-August, 1974, *Earthquake Information Bulletin* 6, 12-17.
- Smith, R. B., Meertens, C. M., and Martinez, L. J. (1998). Implications of GPS deformation measurements on earthquake hazard assessment on the Wasatch Fault zone, *Seismological Research Letters*, 69, 141.
- Stewart, J. H., and Poole, F. G., 1974. Lower Paleozoic and uppermost Precambrian of the Cordilleran miogeocline, Great Basin, western United States, in Dickinson, W. R., ed., *Tectonics and sedimentation*; Society of Economic Mineralogists and Paleontologists Special Publication 22, p. 28-57.
- Stewart, J. H., and Carlson, J. E., 1976. Cenozoic rocks of Nevada; Four maps and brief description of distribution, lithology, age and centers of volcanism: Nevada Bureau of Mines and Geology Map 52, scale 1 : 1,000,000.

- Su, F., K. Aki, T. Teng, Y. Zeng, S. Koyanagi, and K. Mayeda (1992). The relation between site amplification factor and surficial geology in central California, *Bull. Seis. Soc. Am.*, 82, 580-602.
- Taylor, S. R. (1994). False alarms and mine seismicity: An example from the Gentry Mountain mining region, Utah, *Bull. Seis. Soc. Am.*, 84, 350-358.
- Trifunac, M. D. and Brady, A. G. (1975). "A study of the duration of strong earthquake ground motion," *Bull. Seis. Soc. Am.*, 65, 581-626.
- University of Utah Seismograph Stations (UUSS) Home Page (2000), <http://www.seis.utah.edu/HTML/UtahsEarthquakeThreat2.html/>.
- University of Utah Seismograph Stations Home Page (2000), <http://www.ugs.state.ut.us/geohist.htm/>.
- U.S. Geological Survey, 1976. A Study of earthquake losses in the Salt Lake City, Utah area, *U. S. Geol. Surv., Open-File Rept.* 76-89, 357 pp.
- Vanmarke, E. H. and S. P. Lai (1980). Strong-motion duration of earthquake, *Bull. Seis. Soc. Am.* 70, 1293-1307.
- Vidale, J. E. and Helmberger, D. V. (1988). "Elastic finite difference of the 1971 San Fernando earthquake," *Bull. Seis. Soc. Am.* 78, 122-141.
- Wernicke, B., 1981. Low-angle normal faults in the Basin and Range province: *Nature*, 291, 645-648.
- Wong, I. G. and A. McGarr (1990). Implosional failure in mining induced seismology: A critical review, in *Proc. Second Int. Symp. on Rockbursts and Seismicity in Mines*, C. Fairhurst (Editor), Rotterdam, The Netherlands, 45-51.
- Xie, J. and B. J. Mitchell, (1990). Attenuation of multiphase surface waves in the Basin and Range province, part 1: Lg and Lg coda, *Geophys. J. Int.*, 102, 121-137.
- Zandt and Owens, 1980. Crustal flexure associated with normal faulting and implications for seismicity along the Wasatch Front, Utah, *Bull. Seis. Soc. Am.* 70, 1501-1520.
- Zoback, M. L., Anderson, R. E., and Thompson, G. A., 1981, Cenozoic evolution of the state of stress and style of tectonism of the Basin and Range province of the western United States; *Royal Society of London Philosophical Transactions, ser. A*, 300, 407-434.

## Vita Auctoris

Young-Soo Jeon was born in Seoul, Korea on September 27, 1968. He finished his elementary and secondary education in Seoul. After attending Sang-ji University he graduated with a B. E. degree in Mineral and Mining Engineering in February 1995. After this, he entered the army because it was a basic obligation for young Korean males. He then enrolled at Yonsei University and graduated with an M. S. degree in Geophysics in February 1997.

After that, while he worked as a researcher at Natural Science Center at Yonsei University, one of his mentors who works at the KIGAM (Korea Institute of Geology, Mining and Materials) seismology branch encouraged him to start his future work in Seismology. Even though the topic was totally new for him, he decided to pursue that field and joined the Saint Louis University, Department of Earth and Atmospheric Sciences in August 1998 to pursue an M. S. degree in geophysics.